



G E D I M I N A S M O N A S T Y R E C K I S

**D E V E L O P M E N T
O F N O V E L
M U L T I F U N C T I O N A L
F I B R E - R E I N F O R C E D
P O L Y M E R C O M P O S I T E S
U S I N G M X E N E
N A N O P A R T I C L E S**

D O C T O R A L D I S S E R T A T I O N

K a u n a s
2 0 2 3

KAUNAS UNIVERSITY OF TECHNOLOGY

GEDIMINAS MONASTYRECKIS

DEVELOPMENT OF NOVEL
MULTIFUNCTIONAL FIBRE-REINFORCED
POLYMER COMPOSITES USING MXENE
NANOPARTICLES

Doctoral dissertation
Technological Sciences, Mechanical Engineering (T 009)

Kaunas, 2023

This doctoral dissertation was prepared at Kaunas University of Technology, Faculty of Mechanical Engineering and Design, Department of Mechanical Engineering during the period of 2018–2022.

The doctoral right has been granted to Kaunas University of Technology together with Vytautas Magnus University.

Scientific Supervisor

Prof. Dr. Daiva ZELENIAKIENĖ (Kaunas University of Technology, Technological Sciences, Mechanical Engineering, T 009).

Scientific Advisor

Dr. Hab. Leon MISHNAEVSKY Jr. (Technical University of Denmark, Denmark, Technological Sciences, Materials Engineering, T 008).

Edited by: English language editor Brigita Brasienė (Publishing House *Technologija*), Lithuanian language editor Aurelija Gražina Rukšaitė (Publishing House *Technologija*).

Dissertation Defense Board of Mechanical Engineering Science Field:

Prof. Dr. Regita BENDIKIENĖ (Kaunas University of Technology, Technological Sciences, Mechanical Engineering, T 009) – **chairperson**;

Dr. Gintautas DUNDULIS (Kaunas University of Technology, Technological Sciences, Mechanical Engineering, T 009);

Prof. Dr. Roberts JOFFE (Luleå University of Technology, Sweden, Technological Sciences, Materials Engineering, T 008);

Dr. Olesja STARKOVA (University of Latvia, Latvia, Technological Sciences, Mechanical Engineering, T 009).

The official defense of the dissertation will be held at 3 p.m. on 26 of June 2023 at the public meeting of Dissertation Defense Board of Mechanical Engineering Science Field in M7 Hall at the Campus Library of Kaunas University of Technology.

Address: Studentų 48-M7, Kaunas, LT-51367, Lithuania.

Phone: (+370) 608 28 527; e-mail doktorantura@ktu.lt

Doctoral dissertation was sent on 26 of May, 2023.

The doctoral dissertation is available on the internet <http://ktu.edu> and at the library of Kaunas University of Technology (K. Donelaičio 20, Kaunas, LT-44239, Lithuania) and the library of Vytautas Magnus University (K. Donelaičio 52, Kaunas, LT-44244, Lithuania).

KAUNO TECHNOLOGIJOS UNIVERSITETAS

GEDIMINAS MONASTYRECKIS

NAUJŲ DAUGIAFUNKCINIŲ PLUOŠTU
SUSTIPRINTŲ POLIMERINIŲ KOMPOZITŲ
KŪRIMAS PRITAIKANT MAKSENŲ
NANODALELES

Daktaro disertacija
Technologijos mokslai, mechanikos inžinerija (T 009)

Kaunas, 2023

Disertacija rengta 2018–2022 metais Kauno technologijos universiteto Mechanikos inžinerijos ir dizaino fakultete, Mechanikos inžinerijos katedroje.

Doktorantūros teisė Kauno technologijos universitetui suteikta kartu su Vytauto Didžiojo universitetu.

Mokslinis vadovas:

prof. dr. Daiva ZELENIAKIENĖ (Kauno technologijos universitetas, technologijos mokslai, mechanikos inžinerija, T 009).

Mokslinis konsultantas:

habil. dr. Leon MISHNAEVSKY Jr. (Danijos technikos universitetas, Danija, technologijos mokslai, medžiagų inžinerija, T 008).

Redagavo: anglų kalbos redaktorė Brigita Brasienė (leidykla „Technologija“), lietuvių kalbos redaktorė Aurelija Gražina Rukšaitė (leidykla „Technologija“).

Mechanikos inžinerijos mokslo krypties disertacijos gynimo taryba:

prof. dr. Regita BENDIKIENĖ (Kauno technologijos universitetas, technologijos mokslai, mechanikos inžinerija, T 009) – **pirmininkė**;

dr. Gintautas DUNDULIS (Kauno technologijos universitetas, technologijos mokslai, mechanikos inžinerija, T 009);

prof. dr. Roberts JOFFE (Liuleo technologijos universitetas, Švedija, technologijos mokslai, medžiagų inžinerija, T 008);

dr. Olesja STARKOVA (Latvijos universitetas, Latvija, technologijos mokslai, mechanikos inžinerija, T 009).

Disertacija bus ginama viešame mechanikos inžinerijos mokslo krypties disertacijos gynimo tarybos posėdyje 2023 m. birželio 26 d. 15 val. Kauno technologijos universiteto Studentų miestelio bibliotekoje, M7 salėje.

Adresas: Studentų g. 48-M7, Kaunas, LT-51367, Lietuva.

Tel. (+370) 608 28 527; el. paštas doktorantura@ktu.lt

Disertacija išsiųsta 2023 m. gegužės 26 d.

Su disertacija galima susipažinti interneto svetainėje <http://ktu.edu>, Kauno technologijos universiteto (K. Donelaičio g. 20, Kaunas, LT-44239, Lietuva) ir Vytauto Didžiojo universiteto (K. Donelaičio g. 52, Kaunas, LT-44244, Lietuva) bibliotekose.

TABLE OF CONTENTS

LIST OF ABBREVIATIONS AND TERMS	6
INTRODUCTION	8
1. LITERATURE REVIEW.....	11
1.1. Nanoparticles in polymer composites	11
1.2. MXene synthesis and general properties.....	11
1.3. Surface properties.....	13
1.4. Mechanical properties	14
1.5. Electrical properties	14
1.6. Application.....	15
2. METHODOLOGY	18
2.1. Synthesis of MXenes.....	18
2.2. Characterisation.....	18
2.3. Sample preparation.....	18
2.4. Experimental testing.....	19
2.5. Numerical analysis	19
3. REVIEW OF THE PUBLICATIONS.....	21
3.1. Wettability of MXene and its interfacial adhesion with epoxy resin	21
3.2. Micromechanical modelling of MXene-polymer composites.....	22
3.3. Deformation and failure of MXene nanosheets	23
3.4. Strain sensing coatings for large composite structures based on 2D MXene nanoparticles	25
3.5. Scalable MXene and PEDOT-CNT nanocoatings for fibre-reinforced composite de-icing	26
CONCLUSIONS	28
SUMMARY	30
REFERENCES	37
PUBLICATION COPIES.....	53
CURRICULUM VITAE	104
ACKNOWLEDGMENTS	107

LIST OF ABBREVIATIONS AND TERMS

Abbreviations

AFM – atomic force microscopy;
AR – aspect ratio;
CF – carbon fibre;
CNT – carbon nanotubes;
d-Ti₃C₂T_z – delaminated MXenes;
EMI – electromagnetic interference;
FE – finite element;
FRPC – fibre-reinforced polymer composite;
GFRP – glass fibre-reinforced polymer;
GP – graphenes;
HCl – hydrochloric acid;
LiCl – lithium chloride;
LiF – lithium fluoride;
m-Ti₃C₂T_z – multilayered MXenes (non-delaminated);
NC – nanocomposite;
NP – nanoparticle;
PEDOT – poly(3,4-ethylenedioxythiophene);
PLA – polylactic acid;
PUC – periodic unit cell;
PVA – polyvinyl alcohol;
RVE – representative volume element;
SEM – scanning electron microscopy;
TEM – transmission electron microscopy;
Ti₃AlC₂ – titanium aluminium carbide called MAX phase;
Ti₃C₂T_z – titanium carbide nanoparticles called MXenes;
T_z – surface functional groups;
XPS – X-ray photoelectron spectroscopy.

Terms

Aspect ratio – the proportion between 2D nanoparticle size (diameter) and thickness.

Delamination – a process of nanoparticle separation into single-layered 2D flakes.

EMI shielding – a feature of electrically conductive material which prevents the passing of electromagnetic waves.

Hierarchical – a composite structure with several magnitudes of reinforcement components, e.g., epoxy matrix with carbon nanotubes and glass fibres.

Homogenisation – multiscale modelling approach which averages mechanical properties of a composite or structure. The technique is usually achieved with

representative volume element or periodic unit cell finite element models. The values obtained from the microscale can be used as the macroscale.

Monolayers – single-layer of fully delaminated 2D nanoparticle.

Multilayers – delaminated nanoparticles which are stacked together due to van der Waals forces.

Multifunctional – a property of a structure or material which serves multiple functions, e.g., sensing, shielding, healing, etc.

Nanoflake – a delaminated particle of one structural atomic layer, e.g., delaminated $\text{Ti}_3\text{C}_2\text{T}_z$ MXene.

Nanoindentation – puncture test performed for nanofilms and nanocomposites. Nanoindentation can as well be performed for nanoparticles alone, using the tip of an atomic force microscope, which provides force-displacement curves.

Nanosheet – a multilayered particle consisting of several interconnected nanoflakes.

Percolation threshold – a critical concentration of nanofillers where the composite turns abruptly from insulator to conductor through interconnected pathways.

INTRODUCTION

Composite materials have been used in the industry for nearly half a century. It became a considerable cost-effective replacement for traditional metals in some applications. The main advantages of composites are lightweight, anti-corrosion and durability. Furthermore, complex shapes can be easily manufactured using wet-forming, while mechanical properties can be tailored precisely considering fibre's anisotropic behaviour. Nowadays, one of the best structural composite example is a wind turbine blade, which is aerodynamically efficient and has a high strength-to-weight ratio.

The primary technological trend of the composite industry is to lower carbon dioxide footprint during all stages of the life cycle: manufacturing, exploitation and utilisation. However, **the core problem** is that the industry continues to use traditional manufacturing processes based on hardly recyclable fibre-reinforced epoxy composites, which leads to higher pollution and overloaded landfills. Therefore, the researchers focus on developing next-generation composite materials, which are sustainable, durable and have multifunctional properties, such as self-diagnostics or self-healing ^[1]. The durability of the composite structures comes with improved resistance to fatigue, thus resulting in a prolonged operational lifetime. The newest technology, which promises improvement in composite mechanical properties, is hierarchical nanoparticle (NP) reinforcement.

Recent achievements in material engineering unlocked fast and scalable NP production, which led to cheap and commercial access. The last two decades were mainly dedicated to the investigation of carbon-based NP like graphenes (GP) and carbon nanotubes (CNT). Due to their high strength and nano size, the particles increased the fatigue life of the composites, based on the early-stage micro-crack prevention. Moreover, the composites became electrically conductive, which was further applied for sensing purposes. In 2011, a new group of entirely novel 2D NPs called MXenes was discovered ^[2]. These particles possess technologically beneficial properties for nanocomposite (NC) applications, such as metallic conductivity, hydrophilicity and excellent mechanical properties ^[3]. However, the full potential of MXenes for nano-engineered structural polymer composite has not been explored yet.

The surface energy between MXenes and polymers is still not estimated, and it is an essential parameter for adhesion and overall NC mechanical properties. Moreover, several mechanical properties, including interface strength, homogenised properties of multilayered particles, and interlaminar shear strength, are yet to be discovered. Moreover, MXenes have not been investigated as strain-sensing or de-icing nanocoatings for fibre-reinforced polymer composites (FRPC). Therefore, the **primary motivation** for this work is the research and development of innovative multifunctional FRPC.

The research aims to develop fibre-reinforced polymer composites with high mechanical and multifunctional properties based on matrix modification and nanocoating with electrically conductive MXene nanoparticles.

The objectives (O) and tasks (T)

- O1.** Characterise initial properties of MXenes.
 - T1.1.** Evaluate atomic composition, size, thickness and morphology.
 - T1.2.** Investigate wettability properties, surface energy and adhesion strength.
- O2.** Analyse mechanical properties of MXene-polymer NCs, pure MXene flakes and freestanding films using finite element (FE) modelling.
 - T2.1.** Develop multiscale homogenisation methodology using 2D periodic unit cell (PUC) and 3D representative volume element (RVE) models.
 - T2.2.** Predict NC's mechanical properties under different geometrical and mechanical variables.
 - T2.3.** Analyse mechanical properties of MXene flakes and freestanding films using nanoindentation and tensile numerical simulations.
- O3.** Investigate multifunctional properties of FRPC with electrically conductive nanocoatings.
 - T3.1.** Develop coating application methodology and characterise morphology and electrical properties.
 - T3.2.** Analyse electrical resistance sensitivity under different ambient conditions.
 - T3.3.** Investigate piezo-resistive effect of the coating under static tensile and tensile-tensile cyclic loadings.
 - T3.4.** Evaluate de-icing efficiency of the coating under Joules heating.

The novelty of the work

The influence of geometrical parameters, distribution, interface strength and volume fraction on MXene-polymer NC mechanical properties was investigated numerically, while the influence of surface roughness, temperature, UV radiance and mechanical deformations on MXene nanocoating's electrical properties was investigated experimentally. Multifunctional properties of MXene nanocoatings, such as strain-sensing and heating were analysed in this work as well. For the first time, these scientific results were published:

- Wettability and surface energy between MXenes and epoxy matrix suggest high interfacial adhesion.
- The mechanical properties of multilayered MXene flakes are several times lower than single-layered flakes.
- The mechanical properties of interface layers between MXene-epoxy and MXene-polyvinyl alcohol (PVA) are not lower than polymer properties. It is in good agreement with wettability experiments and indicates full-bonding criteria for the modelling analysis.
- Numerical analysis suggests that the mechanical properties of MXene-polymer NC mostly depend on NP alignment, AR, and volume fraction.
- The adhesion strength between MXenes and epoxy is stronger than the adhesion between stacked MXene-MXene particles, which was determined both experimentally and numerically.

- In-situ testing of MXene-coated FRPC under static tensile and tensile-tensile cyclic loadings revealed a piezo-resistive effect and high gauge factor of several nanometer thickness coating.
- MXene nanocoatings are as well responsive to temperature, moisture, UV and direct sunlight exposure, which can influence piezo-resistive experiments. Although such sensitivity allows coating to be used as a multifunctional sensor.
- MXene nanocoatings show faster and more efficient de-icing when compared to traditional carbon-fibre heaters.

Practical significance

The scientific research and obtained results could be applied for:

- New scientific proposals on multifunctional polymer-based NCs and nanocoatings, as a starting scientific data.
- The development of sprayable and printable strain sensors on large composite structures.
- The development of de-icing nanocoatings for ultra-light aircraft, drones, helicopter blades, and wind turbine blades.
- The development of ultrathin nanocoatings for the temperature control of electronic devices and batteries in extreme environments.

Personal input of the author

The author contributed to the synthesis of MXenes with the help of expert personnel. The author partly participated in XPS, AFM and SEM characterisation of MXenes and was consulted regarding the interpretation of the data. The author performed most of the numerical analysis with co-author's consultations on the software and methodology. The author was solely responsible for sample preparation, and with consultations on the equipment and the standards, the author performed all mechanical experiments, including planning, preparation, testing and data curation. The author was as well responsible for post-processing, analysis and interpretation of results and their visualisation. The PhD candidate is the first author in three out of five publications and is the second author in the other two publications.

1. LITERATURE REVIEW

1.1. Nanoparticles in polymer composites

The addition of NPs to polymer composites increases their mechanical properties based on the reinforcement effect, which is related to the superior mechanical properties of NPs and high surface area. Moreover, carbon-based NPs provide electrical conductivity to the polymer, which opens a wide range of new multifunctional capabilities, such as strain-sensing, self-healing and electromagnetic interference (EMI) shielding [1, 4, 5]. As a result, multifunctional polymer composites can be used as smart composites in the automotive and aerospace industries, but with specifically tailored electrical and mechanical properties, they can be used in electronic gadgets, solar cells and batteries.

Graphite and GP, at the filler amount of 2–4 wt%, improve polymer's strength by 10–40% and Young's modulus by 10–95% [6–11]. The electrical conductivity percolation threshold is roughly between 0.2–0.6 wt% with conductivity values of 10^{-3} – 10^{-5} S/cm. In comparison, several investigations show that 0.5–1.5 wt% CNT improved the polymer's strength by 5–20% and modulus by 10–35% [12–16]. The percolation threshold was much lower compared to GP and ranged between 0.05–0.1 wt%, while conductivity values were as well higher and ranged between 10^{-2} – 10^{-3} S/cm at ~1 wt%. High filler concentrations usually increase conductivity but tend to reduce the mechanical properties due to NP agglomeration [17].

In order to achieve polymer NC with proper mechanical and electrical properties requires a compatible polymer matrix, homogeneous distribution of NPs, good interfacial adhesion properties and high AR. A larger overlapping area of the flakes results in a stronger mechanical connection and higher electrical conductivity. Moreover, superior mechanical and electrical properties can be obtained with the alignment of the NPs, which is hardly achievable using CNT. Therefore, 2D NPs, such as GP and MXenes, have received significant attention for their processability [18–20]. However, large quantities of GP are still challenging to produce and require surface modification [21]. Meanwhile, MXenes naturally possess excellent hydrophilic properties and even higher electrical conductivity [22, 23].

1.2. MXene synthesis and general properties

MXenes are prepared from a ceramic precursor called MAX phase, constructed of 2D layered transition metal carbide/nitride atomic blocks $M_{n+1}X_n$ bonded together by "A" layer, usually an aluminium [24, 25]. MAX phase particle shape varies from a complex polygon to an unsymmetrical rectangular with sizes of 1–10 μm [26]. Selective etching of the Al layer from one of MAX phase materials Ti_3AlC_2 using HF results in $\text{Ti}_3\text{C}_2\text{T}_z$ called MXene [27]. Such particles are mostly multilayered, interconnected structures, which often require further delamination procedures [28]. Another etching method is based on HCl and LiF, and during the synthesis, HF and LiCl are produced in-situ [29]. Throughout the synthesis, Li^+ ions act as intercalants, increasing the atomic spacing between the MXene sheets and reducing van der Waals

forces^[30]. Therefore, following a simple shear mixing and centrifugation procedure, MXenes fully delaminate into single-layered flakes. The method was supported by the theoretical investigation of interlayer distance and binding energy and its correspondence to the increase of interlaminar sliding^[31].

The density of delaminated MXenes was estimated similarly to that of titanium, i.e., 3.7 g/cm³^[32]. After the delamination, MXenes contain surface functional groups (T_z), such as -O, -OH and -F^[33]. These groups define the surface properties and make them hydrophilic. Therefore, MXenes can be dispersed in a polar solvent and various polymer matrices^[34]. The size and thickness of MXene particles can differentiate depending on the precursor and the etching procedures^[35, 36]. The NP's size is determined manually through scanning electron microscopy (SEM) and ranges between 1–5 μm . Dynamic light scattering can be used for the average statistical size evaluation as well, but the method is more suitable for volumetric particles, such as non-delaminated MXenes^[37]. For some applications, such as yarn dyeing for smart-textile development, the reduced sizes of MXene (150 nm) are required^[38]. Thus, NP size reduction can be achieved with time and intensity-controlled ultrasonication methods^[39]. The thickness of the NP is determined with atomic force microscopy (AFM). However, more precise measurements can be obtained by using high-resolution transmission electron microscopy (TEM), which can evaluate the thickness of surface functional groups as well. The estimated thickness of delaminated MXene ($d\text{-Ti}_3\text{C}_2\text{T}_z$) flake is equal to 0.98 nm, while non-delaminated multilayered ($m\text{-Ti}_3\text{C}_2\text{T}_z$) flake ranges between 5–30 nm^[40]. The size and thickness proportion, called the aspect ratio (AR), determines how well the NPs are delaminated. This ratio as well determines the flake's mechanical and electrical properties, stability and dispersibility. The AR of $d\text{-Ti}_3\text{C}_2\text{T}_z$ flakes range between 200–1,000^[41], with some new reports of ultra-large flakes with AR of 10,000^[42], while $m\text{-Ti}_3\text{C}_2\text{T}_z$ sheets are between 17–100^[43–45].

MXenes are relatively stable at high temperatures. The thermogravimetric analysis revealed that $\text{Ti}_3\text{C}_2\text{T}_z$ decreased by 4–7% in weight at 700 °C^[46]. Due to the layered nanostructure and good heat dissipation, MXenes showed promising results in fire-retardant coatings and aerogels^[47, 48]. Despite thermal stability, MXenes possess natural oxidation to TiO_2 , which is mainly caused by hydrolysis^[49, 50]. This effect was clarified throughout the ageing experiment in different media, such as polymer, water, ice and open air, and significant differences have been observed^[51]. Moreover, MXene oxidation depends on the solution type, humidity and stored temperatures^[52]. High oxidation rates can be unacceptable for most applications. Therefore, the researchers try to improve MXene stability over the time with various methods^[53]. One of the following modifications, which have shown remarkable results, is hydrogen annealing. The oxidation rate was reduced up to 10 times, and MXene's electrical conductivity recovered almost to its initial value^[52]. Another approach was based on the chemical stabilisation using low amounts (1 mg/mL) of L-ascorbic acid. In water-based MXene solution, it acted as an antioxidant, which slowed down the hydrolysis processes near the flake edges and resulted in up to 5 times decreased oxidation rate^[54]. The last and most common technique is to cover

MXenes with a thin polymer layer or add a small amount of compatible polymer to the mixture, preventing water and air molecules from penetrating [55]. In order to preserve the newly synthesised water-based MXenes, it is advised to store them at low temperatures with sealed and argon-filled flasks [55]. In contrast, the MAX phase shows much better oxidation stability and can be stored at room temperature, non-sealed [56].

MXenes, similar to GP, possess high absorbance in the UV spectrum [57, 58]. Under short-term of UV exposure, the conductivity of MXenes slightly increases due to the spontaneous oxidation at the nanoscale and the photoelectric effect, but in long-term exposure, the oxidation rate is accelerated, and MXenes degrade much faster [59]. For example, a study revealed that MXenes lost over 85% of their conductivity under 24 h UV exposure, while it took 27 days to reach the same result in the dark [51]. Lastly, d-Ti₃C₂T_z show extraordinary EMI shielding properties due to their unique layered atomic structures and metallic behaviour. MXenes possess interlayer reflectiveness of electromagnetic waves and are the most effective material until now, compared to the relative thickness of the coating [60].

1.3. Surface properties

The presence of abundant hydrophilic functional groups on the MXene surface can ensure strong adhesion at the MXene-polymer interface. Surface energy is one of the key parameters determining NC's mechanical characteristics, such as tensile strength, Young's modulus and fracture toughness. The interfacial adhesion and surface energy can be evaluated through contact angle measurements with various liquids [61]. Until now, only a few studies have focused on this research, from which one measured the water contact angle of the rolled MXene film – 21.5° [62], while others reported much higher values for a vacuum-filtered film – 62° [63]. These results suggest that surface energies can differ according to MXene synthesis, oxidation state, quality of MXenes and sample preparation.

Another approach can be based on the computational multiscale modelling analysis. By knowing the properties of NPs and polymers, the interface layer can be estimated by using the inverse modelling technique [64]. Previous inverse modelling studies have successfully obtained GP's interfacial properties, thus supporting this technique [65]. However, in order to accurately predict the layer's strength, the modelling must be validated with experimental data. According to the numerical analysis, the best mechanical properties of the MXene-polymer NCs can be achieved when the load is effectively transferred from the matrix to the NP. This is only possible when a strong interfacial adhesion exists between the polymer matrix and MXene [66]. Few studies suggested a strong interaction between MXenes and polymeric matrices [67, 68]. Later, it was supported by MXene-coated aramid fibre, which interfacial shear strength increased by 3 times [69]. The reinforcing effect occurred due to the increased fibre surface area and fibre-epoxy mechanical interlocking behaviour.

The adhesion strength of a coating composed of pure overlapping NPs mainly depends on van der Waals force and mechanical interlocking caused by roughness and waviness [35]. The film's adhesion is usually obtained by using the nanoindentation

technique, which measures the bending rigidity and estimates the interfacial strength between the flakes [70–72]. One of the recent studies investigated the adhesion between $\text{Ti}_3\text{C}_2\text{T}_z$ and SiO_2 using a spherical tip of AFM [73].

1.4. Mechanical properties

The first theoretical mechanical properties of MXenes were estimated by using molecular dynamics (MD) simulation. Based on the force fields between radius and atomic bond angles, the study predicted $\text{Ti}_3\text{C}_2\text{T}_z$ Young's modulus of 502 GPa and tensile strength of 22 GPa [74]. Later, a nanoindentation study showed slightly lower mechanical properties with modulus and strength of 330 GPa and 17 GPa, respectively [75]. One research suggested that lower properties were caused by atomic defects and irregular structures [76] and was approved by MD nanoindentation simulation, which introduced artificial defects of 1% titanium and 10% carbon atoms inside the $\text{Ti}_3\text{C}_2\text{T}_z$ flake, leading to the same results [77]. It is as well important to emphasize that larger defects, such as wrinkles, pre-cracked flakes and multilayered MXenes, will significantly affect NC's mechanical properties. Therefore, in every investigation, it is essential to characterise MXene quality and shape parameters, such as AR. It was reported that polymer NC with high AR GP increased tensile strength and fatigue life [64, 78].

The strengthening effect can be explained by micromechanical behaviour, when several magnitudes stronger NPs act as reinforcing fillers and prevent micro-cracking of the polymer, based on the fracture energy dissipation and absorption [79]. However, the drawback of GP, in comparison to the MXenes, is the lack of surface functional groups, which correspond to the adhesion strength. MXenes as well exhibit higher bending stiffness and fracture strain when compared to GP, which are essential properties for developing robust and flexible nanofilms [80, 81].

For example, vacuum-filtered freestanding MXene films possess tensile strength of only 18–25 MPa and fracture strain of 0.6–1.2%, which are much smaller when compared to a single MXene flake due to the low binding strength of van der Waals forces [82, 83]. However, recent FE simulations have shown that the alignment of MXenes can significantly increase the ultimate tensile strength [68]. The hypothesis was experimentally proven by using the blade-coating method, and the tensile strength of freestanding MXene films was up to 25 times higher (570 MPa), compared to a filtered film [84]. Furthermore, a similar strengthening effect was achieved with polymer-based NCs when 40 wt% of aligned MXenes improved PVA strength by 3 times [67], while 40 wt% of randomly distributed MXenes increased Young's modulus and hardness of epoxy-based NCs by 2 times [85].

1.5. Electrical properties

The electrical conductivity of pure $\text{Ti}_3\text{C}_2\text{T}_z$ MXene flakes was estimated between 4600 ± 1000 S/cm [39]. Another study obtained remarkable values of up to 11,000 S/cm and confirmed that conductivity greatly depends on MAX phase precursor, synthesis type and flake quality [86]. The conductivity of MXene films and coatings ranges between 1,000–10,000 S/cm and depends on the surface groups, AR

of flakes, coating preparation type, purity and film thickness^[87–89]. For example, using ultra-large MXene flakes, aligned with the blade-coating method, resulted in a conductivity of 15,100 S/cm at the thickness of 214 nm^[84]. Other types of MXene application, such as pure MXene nanofibres, produced by the wet-spinning assembly, reported 7,800 S/cm^[41, 90], while dip-coated textile yarns with 77 wt% MXene loading reached 440 S/cm^[91], and lastly, pure MXene aerogels exhibit only 0.87 S/cm at 98.6% porosity^[92].

MXene polymer films and coatings possess much lower electrical conductivity, which mainly depends on filler volume in the matrix, the polymer's dielectric permittivity and the flake's alignment. Several studies reported the following conductivities of such NC: MXene/Latex film with 6.71 vol% filler loading had 1,400 S/cm^[93]; Ti₃C₂T_z/cellulose nanofibre composite paper with 90 wt% had 0.739 S/cm^[94]; MXene/PVA composites with 90 wt% had 220 S/cm, while at 60 wt%, the values dropped to 0.013 S/cm^[67].

The conductivities of polymer NC filled with randomly distributed multilayered MXenes tend to be several magnitudes lower. For example, few studies reported the percolation threshold of MXene/PAM at 6 wt% with the conductivity of $3 \cdot 10^{-4}$ S/cm while at 75 wt% filler loading, the value increases to $3 \cdot 10^{-2}$ S/cm^[95]. MXene/epoxy NCs show a percolation threshold at ~0.85 wt% with $1.81 \cdot 10^{-8}$ S/cm conductivity, while at 1.2 wt%, the values increase to $4.52 \cdot 10^{-6}$ S/cm^[96]. Although the electrical conductivity of NC is ten orders higher than that of pure epoxy resin ($1.03 \cdot 10^{-18}$ S/cm), the use of such NCs for multifunctional purposes is barely possible. Therefore, in order to achieve multifunctional FRPC, one of these application methods should be considered: thin films with aligned and highly concentrated MXenes, sprayed-coated composites, dip-coated fibres.

1.6. Application

The wind turbine industry is among the largest in composite material usage with a global market valued at around 100 billion EUR (2019). Due to higher wind speeds and air density, which result in a higher energy production rate, wind turbine farm construction is targeted at cold regions and offshore^[97]. As a result, the composite structures suffer increased loads, excessive vibrations and harsh environmental conditions^[98, 99]. The composites tend to degrade faster, experience early matrix cracking and interlaminar debonding, and eventually, the turbine's operation is disturbed^[100, 101]. In order to track composite conditions, various on-site and remote structural health monitoring techniques are used. Traditional sensors, such as piezoelectric transducers, optical fibres and strain gauges, tend to debond after some time, requiring frequent maintenance and calibration. Recently, the successful synthesis and scalable manufacturing methods of various NPs have led researchers to develop electrically conductive polymers and investigate their self-sensing capability^[102, 103]. Besides, CNT and GP, MXenes are considered as more promising materials for polymer NCs due to their hydrophilic properties. The compatibility with various polymers and solvents allows MXenes to be easily processed and applied for various

manufacturing processes, such as 3D printing ^[104], casting ^[84], spray coating ^[105, 106] and vacuum filtration ^[107, 108].

MXene strain-sensing coatings, based on the piezo-resistive effect, were introduced only recently. The piezo-resistive mechanism, which allows tracking composite deformations, structural damage and overall degradation, is based on the local conductivity losses of nanocoating due to its integrity interruption (cracking) and morphology change. Moreover, when MXene flakes start to debond from each other, electrical resistance tends to increase due to the electron tunnelling effects, mostly occurring when the distance between the NPs is less than 3 nm ^[109, 110]. Several numerical studies have shown how the electric resistance changes under nanoscale deformations using quantum tunnelling formulations ^[111, 112]. Furthermore, the piezo-resistance of NP-based strain sensors is well explained by micromechanical FE modelling and theoretical predictions ^[113–115]. Moreover, several studies suggested that the piezo-resistivity of nanocoating depends on the surface morphology ^[116–118]. A study compared GP and MXene nanocoatings under the same tensile loading, and the results showed 4 times higher gauge factor for MXenes ^[119, 120]. Compared with GP nanocoating, a CNT-polymer NC resulted in up to 10 times lower sensitivity to deformations ^[121]. Until now, the most piezo-resistive MXene coating was developed on textile yarns, which resulted in an ultra-sensitive response and gauge factor of 12,900 ^[122].

Water-based $d\text{-Ti}_3\text{C}_2\text{T}_z$ are as well suitable for layer-by-layer coating technology, opening new possibilities for tailored coatings that are based on hierarchical NP combinations ^[123]. For instance, sandwich-type nanolaminates that were developed from 2D nanoflakes, nanowires and nanospheres have shown an ultra-wide sensing range and good cyclic loading response due to flake-to-flake sliding ^[124, 125]. In comparison, $m\text{-Ti}_3\text{C}_2\text{T}_z$ can be used in slightly different applications due to their unique multilayered and porous nanostructures. Successful results were obtained in pressure sensors ^[126, 127], supercapacitors ^[32, 128, 129], EMI shielding films ^[130–132] and solar cells ^[133]. Another positive feature of multilayers is the intercalation of ions and small molecules, which resulted in the energy density improvement of the batteries ^[134, 135], ultra-sensitive gas sensors ^[136–138] and humidity sensors ^[139].

Another important feature of conductive nanocoatings can be considered for de-icing applications. Ice formation on wind turbine blades cause disturbed aerodynamic flow and reduces its efficiency by 20% ^[140, 141]. Traditional metal and CF-based integrated heaters experience face-sheet debonding and are vulnerable to lightning strikes ^[142, 143]. Moreover, these systems consume actual turbine's power of 5–10% ^[144]. Therefore, the development of efficient and scalable de-icing nanocoatings based on Joule heating is of high interest ^[123]. Joule heating is a process when a current flowing through a resistor, in this case, a resistive nanocoating, is converted into heat, following Joule's first law. For example, the de-icing using GP-coated glass fibre rowing resulted in 80 °C after 180 s and 10 V voltage ^[145]. In comparison, aligned CNT coating (6 μm) resulted in 48 °C/min at a power density of 0.128 W/cm² ^[146]. The GP-epoxy (12 wt%) de-icing coating resulted in 13.6 °C/min at 0.125 W/cm² ^[147]. Even though Joule heating of MXenes was investigated only recently, Jia et al.

deposited Ti_3C_2 MXenes on wood-pulp fabric, which showed $63\text{ }^\circ\text{C}/\text{min}$ at $0.174\text{ W}/\text{cm}^2$ [148]. Despite the vast application field of MXenes, the use in multifunctional epoxy-based FRPC lacks investigation.

2. METHODOLOGY

2.1. Synthesis of MXenes

Ti₃C₂T_z MXenes were prepared from Ti₃AlC₂ with a <40 μm particle size and >98 wt% purity (MRC, Kyiv, Ukraine). The etching solvents were 37 wt% HCl and 99 wt% LiF (Merck, Darmstadt, Germany). MAX phase was stirred for 24 h at room temperature. The multi-layered MXene sediment was further delaminated using 99 wt% LiCl (Merck, Darmstadt, Germany). The resulting solution was centrifuged 10–15 times at 3500 rpm and washed until the supernatant reached above pH 6.

2.2. Characterisation

The SEM characterisation of MAX phase, MXene particles and MXene coatings was performed using EVO 40HV (Carl Zeiss AG, Jena, Germany), JSM 6610 (JEOL Ltd., Tokyo, Japan) and S-3400N (Hitachi Ltd., Tokyo, Japan) equipment. Non-conductive MXene-epoxy NC were scanned with additional gold coating, while MXene coatings were scanned on silicon wafers. The homogeneity of the coating was characterised by using a digital optical microscope Leica DVM6, whereas the roughness was evaluated by using an image rendering software LAS X (Leica Microsystems, Wetzlar, Germany). The surface topography of MXene coatings was monitored by using AFM NanoWizard®3 NanoScience and Dimension Icon (Bruker, Billerica, MA, the USA) in PeakForce quantitative nanoscale mechanical mode with ScanAsyst-Air tips ($k = 0.4 \text{ N}\cdot\text{m}^{-1}$) and 0.5 Hz scanning frequency. X-ray photoelectron spectroscopy (XPS) was performed using the K-Alpha system (Thermo Fisher Scientific, Warrington, the UK) equipped with a micro-focused, monochromatic 1486.68 eV Al K α source and a 400 μm beam diameter.

2.3. Sample preparation

The thermosetting epoxy resin Biresin® CR122 and a 3:10 amine curing agent CH122-5 (Sika AG, Baar, Switzerland) were used for NC and GFRP specimen preparation. Polymer-based NC specimens (ISO-527-2-5A) were cast in silicone moulds, whereas GFRP were prepared from twill-weave 163 g/m² glass fibre (Porcher Industries, Erbach, Germany) using the hand-layup technique. All specimens were degassed and cured under vacuum at room temperature for 24 h and post-cured in a convection oven for 5 h at 80–100 °C. The samples were plasma-treated using low-pressure plasma cleaner ZEPTO (Diener Electronic GmbH & Co. KG, Ebhausen, Germany) and argon-enriched K1050X RF plasma cleaner (QuorumTechnologies, Laughton, the UK) to increase the wettability properties that are necessary for water-based spraying. Spray-coating was performed using a 0.4 mm diameter airbrush Sparmax HB-040 (Anest Iwata Sparmax Co., Taipei, Taiwan). The concentration of the delaminated MXenes in the water-based supernatant was reconcentrated from the original 0.34 mg/mL to 3 mg/mL, while PEDOT/CNT aqueous 1:1 paste (SYNPO, Pardubice, the Czech Republic) was reconcentrated to 0.33 mg/mL for more uniform spraying. Copper wires were soldered with conductive polylactic acid (PLA)

Protopasta (Protoplant, Inc., Vancouver, Canada) and covered with silver paste (Ferro GmbH, Frankfurt, Germany) to reduce the contact resistance.

2.4. Experimental testing

Contact angle measurements were performed using See-System E equipment (Advex Instruments, Brno, the Czech Republic) with diiodomethane, deionised water and glycerol for the surface energy investigation. For each test, three 2 ml liquid droplets were placed on the MXene-coated glass samples at different places, and the average contact angle was measured using “See-System” software.

Electrical resistance values were monitored over time using a two-probe 287 True-RMS logging multimeter (Fluke Corporation, Everett, WA, the USA). For long-time fatigue experiments, Arduino Mega 2560 microcontroller (Arduino, Turin, Italy) and a 24-bit analogue-to-digital converter ARD-LTC2499 (Iowa Scaled Engineering, Elbert, CO, the USA) were used together with 10 k Ω reference resistor.

Three-point bending tests were performed using H25 KT universal testing machine (Tinius Olsen, Redhill, the UK) and ISO-178 standards, while tensile and fatigue tests (at 1 Hz amplitude speed) were performed using ElectroPuls E10000T (Instron, Norwood, MA, the USA) and ISO-527. The deformations in the longitudinal direction between four strain markings and transversal deformations between six were measured using Manta G-146B visual extensometer (Allied Vision Technologies, Stadroda, Germany).

Pull-out tests of MXene-coated GFRP specimens were performed (6 samples per each test) using Adheometr PM 420/63 and ISO-4624 standard. The exposure to UV light experiment was performed using a 301–365 nm DRT230 UV lamp and rated power density of 3–7 mW/cm² for the sample surface, considering the distance to the sample. Thermal imaging was performed using FLIR SC7500 (Teledyne FLIR LLC, Wilsonville, Oregon, the USA).

2.5. Numerical analysis

The surface energy of MXenes is influenced by multiple interfacial processes, such as adsorption, wetting and adhesion. In order to evaluate these properties, the harmonic mean and geometric mean approaches were used. In this regard, the surface energy was calculated with equations proposed by Fowkes, Owens and Wendt, which consider contact angle values of different polar and non-polar liquids. The interaction at the interface between MXenes and polymer was evaluated using the work of adhesion parameter.

MXene-polymer NC numerical analysis was simulated using ABAQUS CAE, while nanoindentation and tensile of Ti₃C₂T_z MXene monolayers were performed using LS Dyna software. RVE models with different MXene particle alignments and volume fractions were generated using DIGIMAT FE code. All models were analysed using dynamic explicit methods. The initial stress-strain curves of pure Ti₃C₂T_z flake and epoxy resin were inserted into the software for plasticity and damage characterisation. These were the primary properties of MXenes and epoxy matrix, respectively: Young’s modulus of 330 and 0.97 GPa, tensile strength of 22000 and

41.9 MPa and Poisson's ratio of 0.23 and 0.4. The symmetrical constraints and displacement were applied to the opposite sides of the model's surface nodes. The smallest mesh size of 2D models was 0.2 nm with a total value of $2-3 \cdot 10^5$ quadrilateral elements (S4R), while 3D RVE models had a mesh of 5 nm and a total of $1-2 \cdot 10^6$ tetrahedral elements (C3D4). The damage criterion of $Ti_3C_2T_z$ was assumed ductile due to the metallic titanium layers and was based on the inserted stress-strain curve of pure MXene flakes (obtained from MD simulations). The damage criterion of polymer matrix was based on the maximum principal stress, according to the inserted polymer's stress-strain curve with plasticity region and deformation at failure. The crack growth rate was controlled and calibrated with a damage evolution parameter, i.e., displacement at failure. Failed elements were automatically removed from the model, thus giving a visual crack growth and a drop in the mechanical properties. Stress and strain curves of the models were obtained from summed reaction forces of constrained surface nodes in nN at a given displacement steps in nm.

The multiscale modelling approach was considered in two steps. Firstly, a homogenisation of multi-layered MXenes flakes was evaluated using the PUC model with respect to the experimental data. Due to the multi-layered structure of MXene, the adhesion of polymer matrix only existed with the outer MXene layers and the edges of the inner layers. Due to this, the inner layers had a minimum effect on the mechanical properties due to the early debonding and weak van der Waals forces between the flakes. Therefore, homogenised multi-layered MXene particle properties had a proportionally lower Young's modulus and strength as the ratio between the thickness of two surface flakes (top and bottom single-layered MXene) and total thickness of a multi-layered MXene particle. Secondly, the obtained homogenised mechanical properties of MXenes were used for 3D RVE model filament properties. The model calibration with experimental data was performed by changing the bonding strength between the particle and matrix. The adhesion was determined as an additional interface layer of 5 nm thickness around the particles, which strength and Young's modulus were changed by a factor of 0.25–1 of the surrounding polymer's mechanical values.

3. REVIEW OF THE PUBLICATIONS

3.1. Wettability of MXene and its interfacial adhesion with epoxy resin

The article is published in *Materials Chemistry and Physics*, Elsevier, 2020 [IF: 4,778; AIF: 6,504; IF/AIF: 0,734; Q2; 12 citations]. The graphical abstract of the research, presented in the first publication, is shown in Figure 1. This is the result of collaboration of research groups from 3 institutions by the following authors: K. Zukienė, G. Monastyreckis, S. Kilikevicius, M. Procházka, M. Micusik, M. Omastová, A. Aniskevich and D. Zeleniakienė. The author's contribution to this publication is validation, formal analysis, investigation, writing of the original draft, review and editing, visualisation. The co-authors as well partially contributed to the conceptualisation, methodology, validation, formal analysis, investigation, writing of the original draft, review and editing and visualisation.

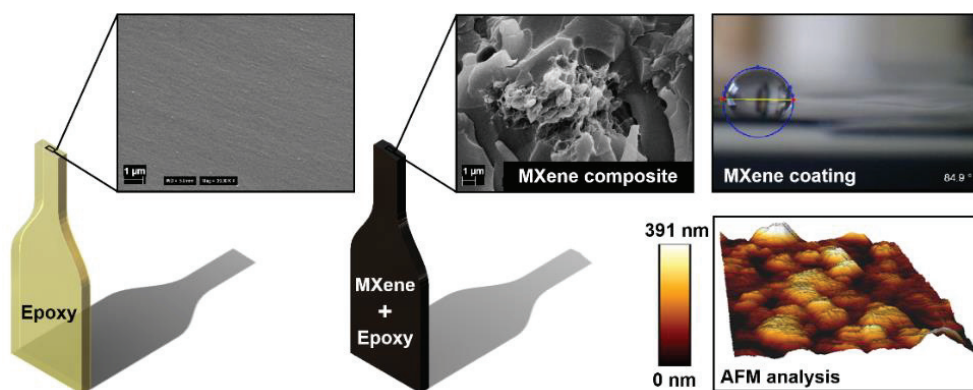


Fig. 1. Graphical abstract of the research presented in the first publication “SEM, AFM and optical imaging of MXene-epoxy NCs and MXene nanocoatings”

This work covers Tasks T1.1 and T1.2 and presents the synthesis of $Ti_3C_2T_z$ MXenes, comprehensive characterisation using XPS, AFM, SEM and surface wettability analysis. The aim of this study was to investigate the surface energy of $Ti_3C_2T_z$ particles and measure interfacial adhesion between MXenes and thermosetting epoxy resin Bisphenol F-epichlorohydrin.

MXenes were prepared from Ti_3AlC_2 MAX phase using HCl/LiF etching method and LiCl delamination procedure. Pure MXene coatings were prepared by dip-coating methods, and 1 wt% MXene-epoxy NCs were prepared using a mechanical stirrer and degassing. The characterisation of MXene particle surface composition was carried out using XPS, which confirmed good Al etching results and the appearance of surface functional groups (T_z), such as hydroxyl, oxide and fluorine groups, which determine MXene's hydrophilic characteristics. The thickness and roughness of the coatings were measured using AFM. The average surface roughness increased with coating layers, which directly influenced the wettability properties. The wettability properties of MXenes, surface energies and work of adhesion were

estimated through the measurements of contact angles using polar and non-polar liquids (water, diiodomethane, glycerol). The wettability improved with more coating layers for all the considered liquids due to the hydrophilic nature of MXenes and nanostructure morphology.

The surface energy of the 10-layer MXene coating was up to 64.48 mJ/m^2 . The surface energy of epoxy with 1 wt% of randomly distributed MXenes increased relative to that of the pure MXene coating. According to the work of adhesion values (123.6 mJ/m^2), the interfacial adhesion between the MXene particles and the epoxy is high. Moreover, it was supported by the post-fracture SEM analysis, where rough and scattered surfaces of MXene-epoxy NCs were observed. The results presented in this article suggest that MXenes can improve polymer's mechanical properties, such as strength, stiffness and resistance to fatigue. Therefore, the following publication focuses on the further investigation of MXene interface layer strength and predicts the mechanical properties of NCs with different particle properties, geometry, weight percentages and alignment using micromechanical FE modelling techniques.

3.2. Micromechanical modelling of MXene-polymer composites

The article is published in *Carbon*, Elsevier, 2020 [IF: 9,594; AIF: 6,592; IF/AIF: 1,455; Q1; 26 citations]. The graphical abstract of the second publication is shown in Figure 2. This is the result of collaboration of research groups from 4 institutions by the following authors: G. Monastyreckis, L. Mishnaevsky Jr., C.B. Hatter, A. Aniskevich, Y. Gogotsi and D. Zeleniakiene. The author's contribution to this publication is methodology, software, validation, formal analysis, investigation, resources, data curation, writing of the original draft, review and editing, visualisation. The co-authors as well partially contributed to the conceptualisation, software, data curation, methodology, validation, formal analysis, review and editing.

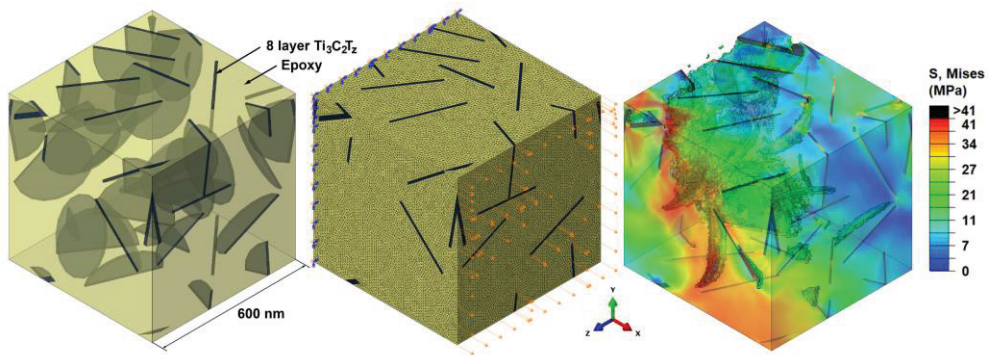


Fig. 2. Graphical abstract of the research presented in the second publication “FE simulation of MXene-polymer RVE model. Distribution, boundary conditions and simulation results”

This work covers Tasks T2.1 and T2.2 and presents a numerical investigation of mechanical properties of novel polymer NC reinforced with MXene nanosheets. The aim of this study is to develop a suitable methodology based on the FE

homogenisation approach for the prediction of elastic properties and micro-structural damage behaviour of MXene-polymer composites.

The geometry and particle distribution of MXene in the RVE models were generated using DIGIMAT software, while FE tensile simulations were performed using ABAQUS CAE. Homogenised Young's modulus of multilayered MXene ($m\text{-Ti}_3\text{C}_2\text{T}_z$) was evaluated with the PUC model. The interface layer was used to determine the adhesion strength between the MXenes and polymer matrix. The calibration of 2D and 3D RVE models with respect to static tensile experiments was performed via inverse modelling techniques by changing the interface layer strength, particle's AR and elastic properties.

In both MXene-PVA and MXene-epoxy FE models, the interface properties were obtained the same as the matrices, which supports the obtained results of the first publication. The average $m\text{-Ti}_3\text{C}_2\text{T}_z$ AR values were measured for 25–31.25 and homogenised Young's modulus, for 22–66 GPa. After the calibration, a comprehensive computational analysis of NC's mechanical properties was performed based on the particle alignment, volume fraction and AR.

The simulation results showed that Young's modulus and tensile strength increased with higher AR, volume fraction and alignment. Thus, with 30 vol% of aligned MXenes, Young's modulus of epoxy-based NC increased 8.4 times and tensile strength 1.91 times. Moreover, aligned MXenes have a much greater influence on the polymer's mechanical properties than random distribution. This insight gives a strong reason to continue the work on high-strength electrical conductivity MXene-polymer films and coatings for the applications, such as structural health monitoring, de-icing and EMI shielding. Therefore, the next publication uses a theoretical approach and FE simulations to focus on the mechanical properties of $d\text{-Ti}_3\text{C}_2\text{T}_z$ MXene particles and freestanding MXene film.

3.3. Deformation and failure of MXene nanosheets

The article is published in *Materials*, MDPI, 2020 [IF: 3,623; AIF: 5,678; IF/AIF: 0,638; Q1; 11 citations]. The graphical abstract of the research, presented in the third publication, is shown in Figure 3. This is the result of collaboration of research groups from 2 institutions by the following authors: D. Zeleniakiene, G. Monastyreckis, A. Aniskevich and P. Griskevicius. The author's contribution to this publication is methodology, data curation, review and editing, visualisation. The co-authors as well contributed to the conceptualisation, methodology, software, validation, formal analysis, investigation, writing of the original draft, review and editing and visualisation.

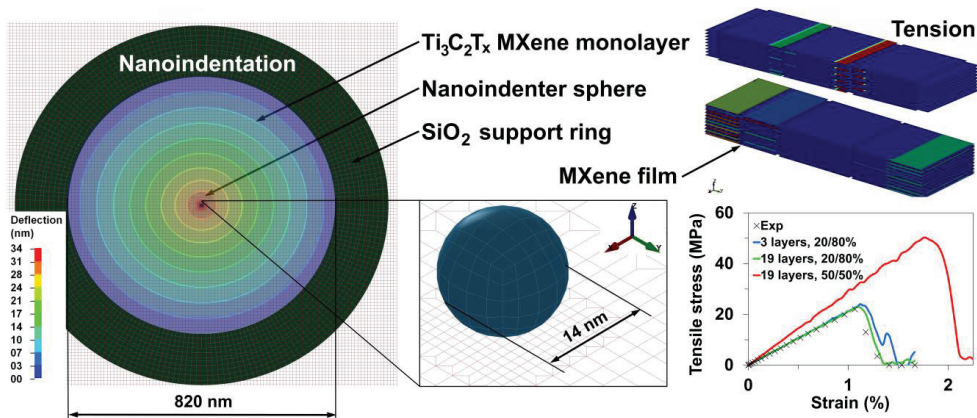


Fig. 3. Graphical abstract of the research presented in the third publication “Nanoindentation and tensile FE simulations of MXenes and pure MXene films”

The work covers Task T2.3 and presents a numerical investigation of the mechanical properties of MXene particles and films. The aim of this study is to develop FE model, which can estimate shear strength, in-plane stiffness and shear energy release rate of MXene nanosheets.

The computational analysis was performed using LS-Dyna explicit software for both FE nanoindentation and nanosheet tensile simulations. An inverse modelling technique with a curve-fitting approach was used for the model calibration. Stress and strain curves were obtained from reaction forces and displacements of shell-type element nodes. First, a parametric sensitivity analysis of $d\text{-Ti}_3\text{C}_2\text{T}_z$ was performed, and in order to fit the experimental data, the thickness of the flake had to be increased from 0.98 to 1.1 nm, or Young's modulus had to be raised from 333 to 380 GPa.

In the model, the flake-to-flake adhesion strength was defined through the cohesive traction–separation law. The best curve-fitting with regards to the experimental data was obtained by using the following parameters: interlaminar shear strength – 2.2 MPa, in-plane stiffness – 0.26 GPa/ μm , and shear energy release rate – $3.8 \cdot 10^{-2} \text{ J/m}^2$. After the calibration, a predictive FE analysis was performed with a maximum theoretical overlapping length of 50% flake size and compared with 20%. Under tensile loading, the strength and failure strain of the film increased roughly two times and stiffness by 40%. The results demonstrate that the mechanical properties of the freestanding films mostly depend on the interlaminar shear strength between the individual flakes, which is determined by van der Waals forces and surface groups of MXenes. These results as well suggest that MXene film's mechanical properties can be greatly increased using high AR flakes, thus having a larger overlapping area. The mechanical parameters that have been obtained in this work can be used as necessary inputs for further computational analysis, which can contribute towards the development of novel, highly conductive and robust multifunctional nanofilms and coatings. Therefore, the next publication focuses on piezo-resistive MXene coating development for the composite's strain monitoring.

3.4. Strain sensing coatings for large composite structures based on 2D MXene nanoparticles

The article is published in *Sensors*, MDPI, 2021 [IF: 3,847; AIF: 4,274; IF/AIF: 0,900; Q2; 10 citations]. The graphical abstract of the research, presented in the fourth publication, is shown in Figure 4. This is the result of collaboration of research groups from 4 institutions by the following authors: G. Monastyreckis, A. Stepura, Y. Soyka, H. Maltanova, S.K. Poznyak, M. Omastova, A. Aniskevich and D. Zeleniakienė. The author's contribution to this publication is conceptualisation, methodology, software, validation, formal analysis, investigation, data curation, writing of the original draft, visualisation. The co-authors as well partially contributed to the conceptualisation, methodology, validation, formal analysis, data curation, investigation, review and editing.

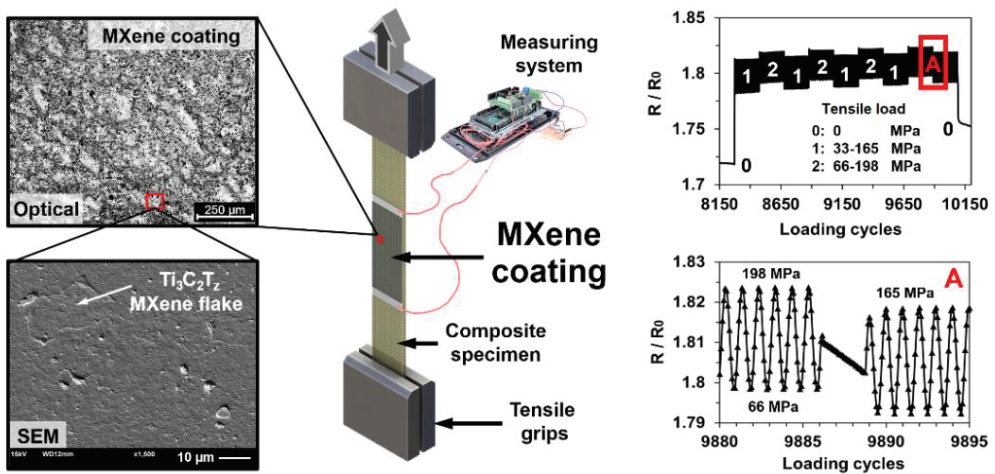


Fig. 4. Graphical abstract of the research presented in the fourth publication “Optical and SEM images of MXene coating, a tensile testing scheme using MXene coated FRPC and relative resistance results under cyclic loading”

This work covers Tasks T3.1, T3.2 and T3.3 and presents the experimental investigation of MXene coating mechanical and electrical properties as well as the piezo-resistive sensing behaviour under static tensile and tensile-tensile cyclic loadings. The aim of this study is to develop an easily processable and scalable MXene nanocoating that can monitor low strain values, typical for fibre-reinforced composites.

Plasma-treated epoxy specimens and GFRP composites were spray-coated with a water-based d-Ti₃C₂T_z solution. First, the coating's morphology and roughness were characterised using digital optical microscopy and SEM. Second, the electrical sensitivity was analysed against temperature change, UV exposure and natural atmospheric oxidation. The influence of temperature on the electrical properties was marginal, while UV irradiation (301–365 nm) had a much more noticeable effect, and at a surface power density of 7 mW/cm², the coating's resistance decreased by 22.7%.

The MXene coating as well experienced natural oxidation, resulting in a gradual increase of resistance values over time. Therefore, all samples for tensile and fatigue tests were covered with a thin epoxy layer. In order to ensure that the layer would last throughout the fatigue experiments, the pull-out (adhesion) tests were performed. The adhesion strength was measured for 2.14 MPa, which was twice lower than that of epoxy-epoxy adhesion; thus, it represented a pull-out strength between MXene particles. Similar results were obtained in a third publication, where the interlaminar shear strength of MXenes was 2.2 MPa. The strain sensitivity of MXenes was analysed on glossy, perpendicular and parallel roughened epoxy surfaces. The results showed that sensitivity depends on the roughening size and direction and is the highest for a sample with a perpendicular to the loading roughening.

Tensile-tensile fatigue tests were performed for MXene-coated epoxy and GFRP samples. The epoxy sample, at 0.5 Hz cycles and 8.33–25 MPa loading amplitude (0.31–0.97% strain), resulted in a 16.25% permanent electrical resistance increase after 21,650 loading cycles. GFRP samples with 0° fibre angle were tested for 10⁴ cycles under varying amplitudes with strains reaching up to 1.86%. The coating's resistance increased permanently by 1.8 times, but the response to loading was stable, and it was easy to differentiate between the loads according to the resistance values. The results demonstrate that MXenes can be considered for scalable and ultra-thin strain-sensing coatings. The following publication is the extension of nanocoating investigation on multifunctional properties. It follows a similar spray-coating technique, characterisation, and focuses on Joule heating, which is intended for de-icing of the composites.

3.5. Scalable MXene and PEDOT-CNT nanocoatings for fibre-reinforced composite de-icing

This article is published in *Materials*, MDPI, 2022 [IF: 3,748; AIF: 6,225; IF/AIF: 0,602; Q1]. The graphical abstract of the research, presented in the fifth publication, is shown in Figure 5. This is the result of collaboration of research groups from 4 institutions by the following authors: G. Monastyreckis, J.T. Siles, P. Knotek, M. Omastova, A. Aniskevich and D. Zeleniakiene. The author's contribution to this publication is conceptualisation, methodology, validation, formal analysis, investigation, data curation, writing of the original draft, visualisation. The co-authors as well partially contributed to the conceptualisation, methodology, validation, formal analysis, investigation, review and editing.

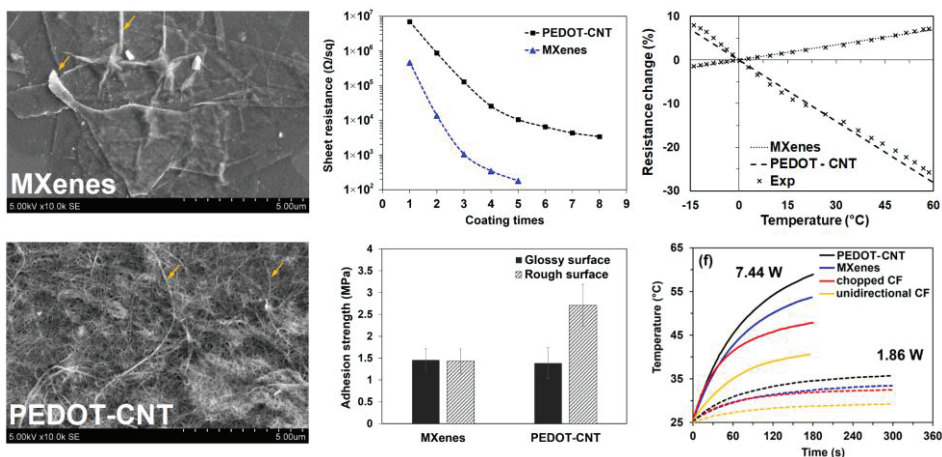


Fig. 5. Graphical abstract of the research presented in the fifth publication “SEM images of MXene and PEDOT-CNT coatings with four graphs representing electrical, mechanical and Joule heating properties”

The work covers Task T3.1, T3.2 and T3.4 and presents an experimental investigation of the nanocoating application for composite de-icing. The aim of this study is to develop an efficient and ultra-thin nanocoating on GFRP composites using a scalable application technique and investigate its adhesion strength, heating behaviour and de-icing performance.

In this study, the de-icing performance is investigated between traditional CF-based coatings (unidirectional and chopped) and novel MXene and poly(3,4-ethylenedioxythiophene)-coated single-walled CNT (PEDOT-CNT) coatings. AFM and SEM characterisation was performed for d-Ti₃C₂T_z flake thickness and size measurements as well as coating's thickness and morphology. MXene coating showed conductivity of 1,000 S/cm at the thickness of ~40 nm, while PEDOT-CNT was up to 25 times less conductive and 5 times thicker. The difference in adhesion strength of both coatings was marginal and equal to 1.5±0.25 MPa. Both coatings showed up to 7 times higher conductivity on a glossy surface when compared to rough. The flexibility and electrical sensitivity of the coatings were investigated under three-point bending. MXene coating showed higher piezo-resistivity and resulted in a permanent resistance increase. In contrast, PEDOT-CNT coating showed a lower gauge factor but responded better to the cycling due to its flexible web-like nanotube structure.

The thermal temperatures were monitored using an infrared camera. Both MXene and PEDOT-CNT coatings resulted in uniform heat distribution throughout the sample and showed no wire overheating, which was observed in traditional CF coatings. Additionally, the average coating temperature increases under the same power density and time was 84% higher for MXenes and 117% for PEDOT-CNT. Therefore, both nanocoatings resulted in up to three times faster de-icing when compared to CF-based coatings. These easily processable coatings offer fast and efficient de-icing for large composite structures, such as wind turbine blades, without adding any significant weight.

CONCLUSIONS

1. The characterisations of MXene flakes were performed using XPS, AFM and SEM. Atomic composition showed no trace of Al and appearance of surface functional groups. The morphology was observed, and the flake thickness was measured for 1.1 nm.
2. The wettability properties of MXenes were obtained by measuring the contact angle of polar and non-polar liquids. Depending on the coating layers, the surface energy was estimated at 47.98–64.48 mJ/m². The work of adhesion value was obtained for 123.6 mJ/m², suggesting high adhesion strength between MXene and epoxy.
3. Multiscale homogenisation methodology was developed using 2D PUC and 3D RVE models based on inverse modelling techniques. Homogenised multilayered MXenes AR was measured for 25–31.25 AR and Young's modulus for 22–66 GPa. Moreover, the interface layer strengths between MXene-epoxy and MXene-PVA were measured to have the same properties as the surrounding matrices.
4. A predictive analysis of NC's mechanical properties was performed, and the simulation results showed that Young's modulus and tensile strength increase with higher AR, volume fraction and the alignment of flakes. For example, with 30 vol% of aligned MXenes, Young's modulus of epoxy-based NC increased by 8.4 times and tensile strength by 1.91 times.
5. A parametric sensitivity analysis of nanoindentation showed that the thickness of the d-Ti₃C₂T₂ flake had to be increased from 0.98 to 1.1 nm or Young's modulus from 333 to 380 GPa. From the numerical simulation of freestanding MXene sheets, these parameters were obtained: interlaminar shear strength – 2.2 MPa, in-plane stiffness – 0.26 GPa/μm and shear energy release rate – $3.8 \cdot 10^{-2}$ J/m².
6. The spray-coating methodology and substrate surface modification were developed. The characterisation of MXene coating was performed using digital optical microscope, AFM and SEM. The coating thickness was estimated at 37 nm, while flake sizes ranged between 2–6 μm. The electrical properties were higher with increased coating thickness and lower with a rougher substrate surface.
7. MXene coating's adhesion test was performed, resulting in 1.5–2.1 MPa. Moreover, the oxidation rate was estimated for 1 month, and 3.7 times more stable results were obtained with epoxy-covered MXenes. The coating showed a slight electrical signal response to the temperature increase, UV exposure and bending as well.
8. MXene coating's piezo-resistive sensitivity was obtained under static tensile and cyclic loadings. The coating's resistance increased permanently by 1.8 times after 10,000 cycles, but the response to loading was stable, and it was easy to differentiate between the loads according to the piezo-resistive effect.

9. MXene coating's Joules heating was analysed using a thermal imaging camera and tested for de-icing of FRPC. The average temperature increase under the same power density and time was 84% higher for MXenes, when compared to the carbon fibre-based coatings. Therefore, nanocoating resulted in up to three times faster de-icing, showing higher efficiency.

SUMMARY

Kompozitinės medžiagos pramonėje naudojamos jau beveik pusę amžiaus. Kai kuriose srityse šios medžiagos tapo ekonomišku metalų pakaitalu tradicinėse konstrukcijose. Pagrindiniai kompozitų privalumai yra lengvumas, antikorozinės savybės ir ilgaamžiškumas. Be to, naudojant kompozitų formavimo technologijas, galima gauti sudėtingų formų detales, o jų mechanines savybes galima tiksliai pritaikyti dėl pluošto anizotropinių savybių. Vienas geriausių kompozitinių konstrukcijų pavyzdžių yra vėjo jėginių mentės, kurios pasižymi dideliu stiprumo ir svorio santykiu ir yra aerodinamiškos.

Pagrindinė kompozitų pramonės tendencija yra sumažinti anglies dioksido pėdsaką visais konstrukcijos gyvavimo etapais – gamyboje, eksploatacijoje ir utilizavime. Tačiau **pagrindinė problema** yra ta, kad pramonė ir toliau naudoja tradicinius gamybos procesus, pagrįstus neperdirbamais pluoštu armuotais epoksidiniais kompozitais, o tai lemia didesnę taršą ir perpildytus sąvartynus. Todėl mokslininkai daugiausia dėmesio skiria naujos kartos kompozitinių medžiagų, kurios būtų tvarios, ilgalaikės ir pasižymėtų daugiafunkcinėmis savybėmis, tokiomis kaip savidiagnostika, kūrimumi. Norint suteikti daugiafunkciškumą, gali pagelbėti naujos technologijos, grįstos nanodalelių (angl. *nanoparticles*, NP) panaudojimu, leidžiančiu pagerinti kompozitinių konstrukcijų ilgaamžiškumą.

Naujausi medžiagų inžinerijos pasiekimai atvėrė greitą ir didelės apimties NP gamybą, kuri lėmė pigų komercinį prieinamumą. Pastarieji du dešimtmečiai daugiausia buvo skirti anglies tipo NP, tokių kaip grafenas ir anglies nanovamzdeliai (angl. *carbon nanotubes* CNT), tyrinėjimui. Buvo pastebėta, kad dėl didelio dalelių stiprumo ir nanoeilės matmenų kompozitų atsparumas nuovargiui padidėjo dėl mikroįtrūkimų sustabdymo. Taip pat, pritaikant šias NP, kompozitai įgijo elektrinį laidumą, kuris buvo tyrinėjamas savidiagnostikos tikslais. 2011 m. buvo atrasta visiškai nauja 2D NP grupė, pavadinta maksenu (angl. *MXenes*). Šios dalelės pasižymi technologiškai naudingomis savybėmis nanokompozitams (angl. *nanocomposites*, NC), tokiomis kaip metalinis laidumas, hidrofiliškumas ir puikios mechaninės savybės. Tačiau makseno pritaikomumas struktūriniais polimeriniams kompozitams dar nebuvo ištirtas.

Viena iš pagrindinių nenustatytų savybių yra paviršiaus energija tarp makseno ir polimerų, kuri lemia gerą sukibimą. Taip pat neįvertintos adhezinės savybės, daugiasluoksnių dalelių homogenizuotos savybės ir tarp sluoksniinis šlyties stiprumas. Be to, maksenas dar nebuvo pritaikytas deformacijų jutikliams ar nuledinimo dangoms pluoštu sustiprintuose polimeriniuose kompozituose (angl. *fibres reinforced polymeric composites*, FRPC). Todėl šio darbo poreikis remiasi inovatyvaus ir daugiafunkcio FRPC sukūrimu.

Tyrimo tikslas – sukurti geromis mechaninėmis ir daugiafunkcinėmis savybėmis pasižymintį pluoštu sustiprintą polimerinį kompozitą, panaudojant elektrai laidžią nanomedžiagą makseną kompozito matricai modifikuoti ir jo nanodangoms.

Tyrimo siekiai (S) ir uždaviniai (U):

S1. Apibūdinti makseno savybes.

U1.1. Nustatyti atominę sudėtį, dydį, storį ir morfologiją.

U1.2. Ištirti vilgumo savybes, paviršiaus energiją ir adhezijos stiprumą.

S2. Išanalizuoti makseno-polimero NC, gryno makseno dalelių ir jų dangų mechanines savybes, naudojant baigtinių elementų (angl. *finite element*, FE) modeliavimą.

U2.1. Sukurti daugiaskalę homogenizavimo metodiką, pritaikant reprezentatyvaus tūrinio elemento (angl. *representative volume element*, RVE) ir periodinio vienetinio elemento (angl. *periodical unit cell*, PUC) modelius.

U2.2. Nustatyti NC mechanines savybes pagal skirtingus mechaninius ir geometrinius kintamuosius.

U2.3. Atlikti skaičiuojamąjį makseno dalelių ir dangų nanoindentacijos bei tempimo modeliavimą.

S3. Ištirti daugiafunkcines FRPC su elektrai laidžiomis nanodangomis savybes.

U3.1. Sukurti dangos formavimo metodiką ir atlikti elektrinių savybių bei morfologijos tyrimus.

U3.2. Atlikti elektrinio jautrumo analizę veikiant įvairiomis aplinkos sąlygomis.

U3.3. Ištirti dangos pjezovaržines savybes esant statinėms tempimo ir ciklinėms apkrovoms.

U3.4. Įvertinti dangos nuledinimo efektyvumą.

Darbo naujumas

Skaitiniais metodais ištirta makseno geometrinių parametrų, pasiskirstymo, tarpsluoksnio stiprumo ir tūrio dalies įtaka makseno-polimero NC mechaninėms savybėms, o eksperimentiniais – paviršiaus šiurkštumo, temperatūros, UV spinduliavimo ir mechaninių deformacijų įtaka makseno nanodangos elektrinėms savybėms. Šiame darbe taip pat buvo analizuojamos daugiafunkcinės makseno nanodangų savybės, tokios kaip deformacijų jutimas ir šilimas. Pirmą kartą buvo paskelbti šie moksliniai rezultatai:

- Nustatytos vilgumo ir paviršiaus energijos tarp makseno ir epoksidinės matricos vertės demonstruoja geras adhezinės savybes.
- Daugiasluoksnių makseno dalelių mechaninės savybės yra kelis kartus mažesnės nei vienasluoksnių.
- Tarpfazinių sluoksnių tarp makseno ir epoksidinės dervos bei makseno ir polivinilo alkoholio (PVA) mechaninės savybės yra ne mažesnės nei polimero savybės. Tai patvirtina tiek vilgumo eksperimentai, tiek modeliavimo analizė.
- Skaitinė analizė rodo, kad makseno-polimero NC mechaninės savybės labiausiai priklauso nuo NP išlygiavimo, kraštinių santykio (angl. *aspect ratio*, AR) ir tūrio dalies.

- Adhezijos stiprumas tarp makseno ir epoksidinės dervos yra didesnis nei tarp gryno makseno dalelių plėvelėse, tai patvirtinta tiek eksperimentiškai, tiek skaitiniais metodais.
- Maksenu dengto FRPC bandymas *in-situ*, esant statinėms tempimo ir tempimo-tempimo ciklinėms apkrovoms, atskleidė pjezovaržinį efektą ir aukštą kelių nanometrų storio dangų pjezovaržinio stiprinimo koeficientą.
- Makseno nanodangos reaguoja į temperatūrą, drėgmę, UV ir tiesioginius saulės spindulius, kurie gali turėti įtakos pjezovaržinėms savybėms. Tačiau toks jautrumas leidžia dangą naudoti kaip daugiafunkcij jutiklį.
- Naudojant makseno nanodangas nustatytas greitesnis ir efektyvesnis FRPC nuleidinimas, palyginti su tradiciniais anglies pluošto šildytuvais.

Praktinis pritaikomumas

Moksliniai tyrimai ir gauti rezultatai gali būti taikomi:

- Kaip pradiniai duomenys naujoms mokslinėms paraiškoms, tyrinėjančioms daugiafunkcinius polimerinius nanokompozitus ir nanodangas.
- Purškiamų ir spausdinamų deformacijų jutikliams ant didelėms kompozitinėms konstrukcijoms kurti.
- Itin lengvų orlaivių, bepiločių orlaivių, sraigtasparnių ir vėjo turbinų menčių nuleidinimo nanodangoms kurti.
- Ypač plonomis nanodangoms, skirtoms elektroninių prietaisų ir baterijų temperatūrai kontroliuoti ekstremaliose aplinkose.

Autoriaus indėlis

Autorius kartu su ekspertų pagalba prisidėjo prie makseno nanodalelių sintetinio. Taip pat iš dalies dalyvavo charakterizavimo tyrimuose pritaikant rentgeno fotoelektroninę spektroskopiją (angl. *X-ray photoelectron spectroscopy*, XPS), atominės jėgos mikroskopiją (angl. *atomic force microscopy*, AFM) ir skenuojamąją elektroninę mikroskopiją (angl. *scanning electron microscopy*, SEM), po kurių buvo konsultuojamas dėl duomenų interpretavimo bei aprašymo tikslumo. Su bendraautorių patarimais apie programinės įrangos ypatumus ir skaičiavimo metodikas didžiąją dalį skaitinės analizės autorius atliko savarankiškai. Konsultuodamasis dėl įrangos valdymo ypatumų ir standartų pritaikymo, autorius savarankiškai paruošė visus bandinius ir atliko mechaninius eksperimentus, įskaitant planavimą, pasiruošimą, testavimą ir duomenų apdorojimą. Autorius taip pat buvo atsakingas už rezultatų analizę ir interpretavimą bei jų vizualizavimą. Doktorantas yra pirmasis trijų iš penkių publikacijų autorius ir antrasis dviejų publikacijų autorius.

Straipsnių apžvalga

Straipsnio, pavadinimu „**Wettability of MXene and its interfacial adhesion with epoxy resin**“, tyrimų tikslas buvo ištirti $Ti_3C_2T_z$ makseno nanodalelių paviršiaus energiją ir įvertinti adheziją su epoksidine derva (užduotys U1.1 ir U1.2). Maksenas buvo susintetintas iš Ti_3AlC_2 „MAX“ fazės, naudojant HCl/LiF išdininimo metodą ir LiCl delaminacijos procedūrą. Makseno dangos buvo suformuotos įmerkiant substratą į makseno vandeninį tirpalą ir išdžiovinant, o 1 wt% (masės dalies) makseno ir epoksidinės dervos NC buvo paruošti naudojant mechaninį maišymą ir vakuavimą. Makseno dalelių sudėtis nustatyta naudojant XPS. Šie rezultatai parodė gerą aliuminio pašalinimą bei patvirtino paviršiaus funkcinių grupių (T_z), tokių kaip hidroksido, oksido ir fluoro, lemiančių geras hidrofilines savybes, atsiradimą. Dangų storis ir šiurkštumas buvo išmatuotas naudojant AFM. Makseno vilgumo savybės, paviršiaus energija ir adhezijos darbas buvo įvertintas matuojant polinius ir nepolinius skysčių vilgumo kampus. Vilgumas pagerėjo naudojant storesnes dangas dėl makseno hidrofiliškumo ir nanostruktūros morfologijos. Dešimties sluoksnių dangos paviršiaus energija siekė $64,48 \text{ mJ/m}^2$, o epoksidinės dervos su 1 wt% atsitiktinai paskirsčiusių dalelių adhezijos darbas buvo lygus $123,6 \text{ mJ/m}^2$. Tokie rezultatai lemia gerą paviršiaus adheziją tarp makseno ir epoksidinės dervos. Taip pat šią prielaidą patvirtina ir kompozito lūžio paviršiaus vaizdai, gauti iš SEM analizės. Šiame straipsnyje pateikti rezultatai rodo, kad maksenas gali pagerinti polimero mechanines savybes, tokias kaip stiprumas, standumas ir atsparumas nuovargiui. Todėl kitoje publikacijoje toliau nagrinėjami makseno tarp sluoksnių stiprumas ir NC mechaninių savybių priklausomybė nuo skirtingo dalelių kiekio, geometrijos bei kryptiškumo, naudojant FE modeliavimą.

Straipsnio, pavadinimu „**Micromechanical modeling of MXene-polymer composites**“, tyrimų tikslas buvo sukurti tinkamą metodiką, pagrįstą FE homogenizacijos principais, skirtą makseno-polimero NC tamprumo ir stiprumo savybėms bei struktūriniais pažeidimams prognozuoti (užduotys U2.1 ir U2.2). Makseno dalelių geometrija ir pasiskirstymas RVE modeliuose buvo sugeneruotas naudojant DIGIMAT, o FE tempimo modeliavimas buvo atliktas naudojant ABAQUS CAE programinę įrangą. Homogenizuoto daugiasluoksnių makseno tamprumo modulis buvo įvertintas naudojant PUC modelį. Kintamos tarp sluoksnių savybės buvo naudojamos sukibimo stiprumui tarp makseno ir polimerinės matricos įvertinti, pritaikant atvirkštinio modeliavimo metodą. 2D ir 3D RVE modelių skaičiavimo kalibravimas buvo atliktas atsižvelgiant į statinio tempimo eksperimentinius rezultatus, esant PVA NC su išlygiuotomis dalelėmis, bei epoksidinės dervos NC su atsitiktinai pasiskirsčiusiomis dalelėmis. Abiejų NC tarp sluoksnių stiprumo savybės buvo prilygstančios jų matricoms. Delaminuotų maksenų AR vertės buvo gautos tarp 25–31,25, o homogenizuotas tamprumo modulis tarp 22–66 GPa. Po kalibravimo buvo atlikta išsami skaičiuojamoji analizė, leidusi nustatyti NC mechanines savybes, esant įvairiems kintamiesiems. Modeliavimo rezultatai parodė, kad tamprumo modulis ir stiprumas tempiant padidėjo dėl didesnio AR, užpildo kiekio ir dalelių išlygiavimo. Esant makseno NC su 30 vol% užpildu (tūrinės dalies), tamprumo

modulis padidėjo 8,4 kartus, o stiprumas – 1,91 karto. Rezultatai rodo, kad išlygiuotos dalelės turi daug didesnę poveikį polimero mechaninėms savybėms nei atsitiktinai pasiskirsčiusios. Dalelių išlygiavimas taip pat suteikia NC plėvelėms ir dangoms didelį elektrinį laidumą, kuris svarbus kuriant daugiafunkcinius kompozitus. Todėl kitoje publikacijoje nagrinėjamos pavienių makseno dalelių bei jų dangų mechaninės savybės, pritaikant FE modeliavimą.

Straipsnio, pavadinimu „**Deformation and Failure of MXene Nanosheets**”, tyrimų tikslas buvo sukurti FE modelį, kuris leistų įvertinti delaminuoto makseno šlyties stiprumą, standumą ir šlyties energijos išsiskyrimo koeficientą (užduotis U2.3). Skaičiavimo analizė buvo atlikta naudojant LS-Dyna programinę įrangą. Modeliui kalibruoti pagal eksperimentinius rezultatus buvo naudojamas atvirkštinio modeliavimo metodas. Įtempių ir deformacijų kreivės buvo gautos iš reakcijos jėgų ir modelio mazgų poslinkių. Pirmiausia buvo atlikta parametrinė jautrumo analizė pagal eksperimentinius duomenis. Rezultatų atitikimu buvo pasiektas su padidintu dalelės storiu (nuo 0,98 iki 1,1 nm) arba padidintu tamprumo modulių (nuo 333 iki 380 GPa). Modelyje makseno tarpusavio adhezija buvo apibrėžta sukibimo ir atskyrimo jėgos dėsnio (angl. *traction-separation law*). Geriausiai eksperimentinius rezultatus atitinkanti modeliavimo kreivė buvo gauta naudojant šiuos parametrus: tarpfluoksninis šlyties stiprumas – 2,2 MPa, santykinis standumas – 0,26 GPa/μm ir šlyties energijos išsiskyrimo koeficientas – $3,8 \cdot 10^{-2} \text{ J/m}^2$. Po kalibravimo buvo atlikta tempimo simuliacija su didžiausiu teoriniu dalelių persidengimo ilgiu (50%) ir buvo gautas du kartus padidėjęs plėvelės stiprumas ir trūkimo deformacija, standumas padidėjęs 40%. Rezultatai rodo, kad dangų mechaninės savybės labiausiai priklauso nuo tarpfluoksninio šlyties stiprumo ir dalelių AR, kurie lemia didesnę persidengimo plotą. Šiame darbe gauti mechaniniai parametrai gali būti naudojami tolesnei skaičiavimo analizei, tiriančiai daugiafunkcines nanoplėveles ir dangas. Todėl kitoje publikacijoje pagrindinis dėmesys skiriamas pjezovaržinių makseno savybių tyrimams, kurie leistų stebėti kompozito deformacijas ir pažeidimus.

Straipsnio, pavadinimu „**Strain Sensing Coatings for Large Composite Structures Based on 2D MXene Nanoparticles**”, tyrimų tikslas buvo sukurti lengvai formuojamą makseno dalelių dangą, kuri galėtų aptikti mažas deformacijas, būdingas pluoštu armuotiems kompozitams (užduotys U3.1, U3.2 ir U3.3). Plazma apdoroti padidinto vilgumo epoksidiniai bandiniai ir stiklo pluoštu armuoti polimeriniai (angl. *glass fibre reinforced polymer*, GFRP) kompozitai buvo padengti vandeniniu delaminuotų makseno dalelių tirpalu purškiant. Dangos morfologija ir šurkštumas buvo charakterizuoti naudojant skaitmeninį optinį mikroskopą ir SEM. Elektrinis jautrumas buvo analizuojamas atsižvelgiant į temperatūros pokyčius, UV poveikį ir natūralią oksidaciją. Temperatūros poveikis elektrinėms savybėms buvo nedidelis, o UV spinduliuotės (301–365 nm) – daug didesnis, ir, esant paviršiaus galios tankiui 7 mW/cm^2 , dangos varža sumažėjo 22,7%. Buvo atlikti makseno dangos adhezijos testai, kurie parodė 2,14 MPa stiprumą. Panašūs rezultatai buvo gauti antroje publikacijoje, kurioje maksenų tarpfluoksninis šlyties stiprumas buvo lygus 2,2 MPa. Dangos elektrinis jautrumas deformacijai buvo ištirtas ant lygių ir šurkščių paviršių.

Rezultatai parodė, kad pjezovaržinis jautrumas priklauso nuo šiurkštumo dydžio ir krypties, ir yra didžiausias esant statmenam apkrovai šiurkštumui. Tempimo ir nuovargio tyrimai buvo atlikti su epoksidiniais bei GFRP bandiniais. Maksenu dengtas epoksidinis bandinys, esant 0,5 Hz ciklams ir 8,33–25 MPa apkrovos amplitudei (0,31–0,97% deformacijai), pasižymėjo 16,25% negrįžtamu elektrinės varžos padidėjimu po 21650 apkrovimo ciklų. GFRP bandiniai su 0° armavimo kryptimi buvo apkrauti 10000 ciklų su skirtingomis amplitudėmis. Dangos negrįžtama elektrinė varža padidėjo 1,8 karto, tačiau jutimas apkrovai buvo stabilus ir priklausė nuo jos dydžio. Rezultatai parodė, kad makseno dalelės gali būti pritaikytos itin plonomis sensorinėms dangoms, jaučiančiomis deformacijas ir pažeidimus. Kita publikacija tiria tolimesnį tokios dangos pritaikomumą daugiafunkcinėms savybėms, tokioms kaip kompozito šilimas bei ledo atitirpinimas.

Straipsnio, pavadinimu „**Scalable MXene and PEDOT-CNT Nanocoatings for Fibre-Reinforced Composite De-Icing**”, tyrimų tikslas buvo sukurti efektyvią ir itin ploną nanodangą, skirtą ledo atitirpinimui nuo kompozitinių konstrukcijų (užduotys U3.1, U3.2 ir U3.4). Šiame tyrime buvo analizuojamos tradicinės anglies pluošto dangos (vienkryptės ir smulkintos) ir makseno dalelių bei *poly(3,4-ethylenedioxythiophene)* su CNT užpildu (PEDOT-CNT) nanodangos. AFM ir SEM analizė buvo naudota dangos storiui ir morfologijai įvertinti. Penkis kartus užpurkštų makseno dangų elektrinis laidumas buvo lygus 1000 S/cm, esant ~40 nm storiui, o PEDOT-CNT danga buvo apie 25 kartus mažiau laidų ir 5 kartus storesnė. Nustatytas iki 7 kartų didesnis abiejų dangų laidumas ant lygaus paviršiaus negu ant šiurkštaus. Taip pat buvo atlikti dangų jautrumo ir lankstumo tyrimai esant tritaškiui lenkimui. Makseno danga pasižymėjo didesniu pjezovaržiniu jautrumu ir negrįžtamu elektrinės varžos pokyčiu, o PEDOT-CNT danga buvo mažiau jautri, bet lankstesnė esant ciklinei apkrovai. Šiluminis išsiskyrimas, remiantis Džaulio pirmu dėsniu, dangose buvo stebimas naudojant infraraudonųjų spindulių kamerą. Abi nanodangos pasireiškė tolygiu šilumos pasiskirstymu, o tradicinės anglies pluošto dangos šilo netolygiai. Palyginti su tradicinėmis dangomis, vidutinė makseno nanodangos temperatūra esant tokiam pačiam galios tankiui ir laikui buvo 84% didesnė, o PEDOT-CNT dangos – 117% didesnė, todėl abi nanodangos lėmė iki trijų kartų greitesnį ledo atitirpinimą. Tyrimo rezultatai rodo, kad šios lengvai formuojamos nanodangos užtikrina greitesnį ir efektyvesnį ledo atitirpinimą ir gali būti pritaikomos naudojant dideles kompozitines konstrukcijas, tokias kaip vėjo jėgainių mentės, nepridedant papildomo svorio konstrukcijai.

Išvados:

- 1 Makseno nanodalelių charakterizavimas atliktas naudojant XPS, AFM ir SEM. Atominė sudėtis parodė gerą aliuminio išsėdinimą bei paviršiaus funkcinių grupių atsiradimą. Nustatyta nanodalelių morfologija, o išmatuotas dalelės storis prilygo 1,1 nm.
- 2 Makseno vilgumo savybės įvertintos matuojant polinių ir nepolinių skysčių vilgumo kampus. Priklausomai nuo dangos sluoksnių, paviršiaus energija buvo

- gauta tarp 47,98–64,48 mJ/m². Adhezijos darbas buvo 123,6 mJ/m², o tai rodo gerą adhezijos stiprumą tarp nanodalelių ir epoksidinės dervos.
- 3 Naudojant 2D PUC ir 3D RVE modelius, buvo sukurta daugiaskalės homogenizacijos metodika, paremta atvirkštinio modeliavimo technika. Buvo gautos šios homogenizuotos daugiasluoksnių makseno dalelių mechaninių savybių ribos: AR – nuo 25 iki 31,25; tamprumo modulis – nuo 22 iki 66 GPa. Buvo tirtas tarp sluoksnių stiprumas tarp makseno ir epoksidinės dervos ir PVA, rezultatai parodė, kad tarp sluoksnių pasivėžimi tomis pačiomis mechaninėmis savybėmis, kaip ir matricos.
 - 4 NC prognozuojamoji mechaninių savybių analizė parodė, kad tamprumo modulis ir stiprumas didėja esant didesniai AR, užpildo kiekiui ir nanodalelių išlygiavimui. Pavyzdžiui, naudojant 30 vol% išlygiuotų nanodalelių, NC tamprumo modulis padidėja 8,4 kartus, o stiprumas – 1,91 karto.
 - 5 Nanoindentacijos parametrinė jautrumo analizė parodė, kad delaminuotos makseno dalelės storis turi būti padidintas nuo 0,98 iki 1,1 nm arba tamprumo modulis nuo 333 iki 380 GPa. Atliekant skaitinį tempimo modeliavimą, gauti šie parametrai: tarp sluoksnių šlyties stiprumas – 2,2 MPa, santykinis stiprumas – 0,26 GPa/μm ir šlyties energijos išsiskyrimo koeficientas – $3,8 \cdot 10^{-2} \text{ J/m}^2$.
 - 6 Sukurta purškimo dengimo ir paviršiaus modifikavimo metodika. Makseno dangos charakterizavimas atliktas naudojant skaitmeninę optinę mikroskopą, AFM ir SEM. Apskaičiuotas dangos storis lygus 37 nm, o dalelės dydis svyruoja tarp 2–6 μm. Elektrinės savybės buvo gautos didesnės padidėjus dangos storiui ir mažesnės, kai pagrindo paviršius buvo šiurkštesnis.
 - 7 Atlikti makseno nanodangos adhezijos bandymai ir gauti 1,5–2,1 MPa įtempiai. Oksidacija buvo įvertinta 1 mėnesio laikotarpiu. Naudojant epoksidinę dervą dengtą makseno dangą, buvo gauta 3,7 karto mažesnė oksidacija. Taip pat buvo įvertintas dangos elektrinis jautrumas temperatūrai, UV spindulių poveikiui ir lenkimui.
 - 8 Makseno dangos pjėzovaržinis jautrumas buvo gautas esant statinėms tempimo ir ciklinėms apkrovoms. Po 10 000 ciklų dangos elektrinė varža negrįžtamai padidėjo 1,8 karto, tačiau reakcija į apkrovą buvo stabili, ir pagal pasikeitusias elektrines vertes apkrovos metu buvo galima nustatyti bandinio deformacijas.
 - 9 Džaulio principu kaitinama makseno danga buvo iširta naudojant terminio vaizdo kamerą ir išbandytas pritaikomumas kompozitų ledui atitirpinti. Palyginti su tradicinėmis anglies pluošto dangomis, vidutinė makseno nanodangos temperatūra esant tokiam pačiam galios tankiui ir laikui buvo 84% didesnė, ir tai lėmė iki trijų kartų greitesnį ledo atitirpinimą.

REFERENCES

1. GIBSON, Ronald F. A review of recent research on mechanics of multifunctional composite materials and structures. *Composite Structures*. Online. 2010. Vol. 92, no. 12, p. 2793–2810. DOI 10.1016/j.compstruct.2010.05.003.
2. NAGUIB, Michael, KURTOGLU, Murat, PRESSER, Volker, LU, Jun, NIU, Junjie, HEON, Min, HULTMAN, Lars, GOGOTSI, Yury and BARSOUM, Michel W. Two-dimensional nanocrystals produced by exfoliation of Ti_3AlC_2 . *Advanced Materials*. 2011. Vol. 23, no. 37, p. 4248–4253. DOI 10.1002/adma.201102306.
3. GOGOTSI, Yury and ANASORI, Babak. The Rise of MXenes. *ACS Nano*. 2019. Vol. 13, p. 8491–8494. DOI 10.1021/acsnano.9b06394.
4. MARUTHI, N, FAISAL, Muhammad and RAGHAVENDRA, Narasimha. Conducting polymer based composites as efficient EMI shielding materials : A comprehensive review and future prospects. *Synthetic Metals*. Online. 2021. Vol. 272, no. October 2020, p. 116664. DOI 10.1016/j.synthmet.2020.116664.
5. NIU, Pengying, BAO, Nanbin, ZHAO, Huhu, YAN, Shuang, LIU, Beibei, WU, Yukai and LI, Huanjun. Room-temperature self-healing elastomer-graphene composite conducting wires with superior strength for stretchable electronics. *Composites Science and Technology*. Online. 2022. Vol. 219, no. January, p. 109261. DOI 10.1016/j.compscitech.2022.109261.
6. WANG, Chunyan, LAN, Yanfei, LI, Xing, YU, Wenting and QIAN, Yong. Improving the mechanical, electrical, and thermal properties of polyimide by incorporating functionalized graphene oxide. *High Performance Polymers*. 2016. Vol. 28, no. 7, p. 800–808. DOI 10.1177/0954008315598818.
7. RYU, Sung Hun and SHANMUGHARAJ, A M. Influence of long-chain alkylamine-modified graphene oxide on the crystallization , mechanical and electrical properties of isotactic polypropylene nanocomposites. *Chemical Engineering Journal*. Online. 2014. Vol. 244, p. 552–560. DOI 10.1016/j.cej.2014.01.101.
8. WAJID, Ahmed S, AHMED, H S Tanvir, DAS, Sriya, IRIN, Fahmida, JANKOWSKI, Alan F and GREEN, Micah J. High-Performance Pristine Graphene/Epoxy Composites With Enhanced Mechanical and Electrical Properties. *Macromol. Mater. Eng*. 2013. Vol. 298, p. 339–347. DOI 10.1002/mame.201200043.
9. TRIPATHI, Sandeep Nath, SAINI, Parveen, GUPTA, Deeksha and CHOUDHARY, Veena. Electrical and mechanical properties of PMMA/reduced graphene oxide nanocomposites prepared via in situ polymerization. *J. Mater. Sci*. 2013. Vol. 48, p. 6223–6232. DOI 10.1007/s10853-013-7420-8.
10. YOONESSI, Mitra and GAIER, James R. Highly Conductive Multifunctional Graphene Polycarbonate Nanocomposites. *ACS Nano*. 2010.

- Vol. 4, no. 12, p. 7211–7220. DOI 10.1021/nm1019626.
11. LI, Yan, ZHANG, Han, PORWAL, Harshit, HUANG, Zhaohui, BILOTTI, Emiliano and PEIJS, Ton. Mechanical, electrical and thermal properties of in-situ exfoliated graphene/epoxy nanocomposites. *Composites Part A*. Online. 2017. Vol. 95, p. 229–236. DOI 10.1016/j.compositesa.2017.01.007.
 12. KOO, Min Ye, SHIN, Hon Chung, KIM, Won-seok and LEE, Gyo Woo. Properties of multi-walled carbon nanotube reinforced epoxy composites fabricated by using sonication and shear mixing. *Carbon Letters*. 2014. Vol. 15, no. 4, p. 255–261. DOI 10.5714/CL.2014.15.4.255.
 13. MA, Peng Cheng, KIM, Jang-Kyo and TANG, Ben Zhong. Effects of silane functionalization on the properties of carbon nanotube/epoxy nanocomposites. *Composites Science and Technology*. 2007. Vol. 67, p. 2965–2972. DOI 10.1016/j.compscitech.2007.05.006.
 14. MA, Peng Cheng, TANG, Ben Zhong and KIM, Jang-Kyo. Effect of CNT decoration with silver nanoparticles on electrical conductivity of CNT-polymer composites. *Carbon*. 2008. Vol. 46, p. 1497–1505. DOI 10.1016/j.carbon.2008.06.048.
 15. SONG, Young Seok and YOUN, Jae Ryou. Influence of dispersion states of carbon nanotubes on physical properties of epoxy nanocomposites. *Carbon*. 2005. Vol. 43, p. 1378–1385. DOI 10.1016/j.carbon.2005.01.007.
 16. LI, Yichao, LI, Renfu, FU, Xuewei, WANG, Yu and ZHONG, Wei-hong. A bio-surfactant for defect control: Multifunctional gelatin coated MWCNTs for conductive epoxy nanocomposites. *Composites Science and Technology*. Online. 2018. Vol. 159, p. 216–224. DOI 10.1016/j.compscitech.2018.03.001.
 17. LI, Yichao, HUANG, Xianrong, ZENG, Lijian, LI, Renfu, TIAN, Huafeng and FU, Xuewei. Review A review of the electrical and mechanical properties of carbon nanofiller-reinforced polymer composites. *Journal of Materials Science*. Online. 2019. Vol. 54, no. 2, p. 1036–1076. DOI 10.1007/s10853-018-3006-9.
 18. CHEN, Ye, FAN, Zhanxi, ZHANG, Zhicheng, NIU, Wenxin, LI, Cuiling, YANG, Nailiang, CHEN, Bo and ZHANG, Hua. Two-Dimensional Metal Nanomaterials : Synthesis , Properties , and Applications. *Chemical Reviews*. 2018. Vol. 118, p. 6409–6455 Review. DOI 10.1021/acs.chemrev.7b00727.
 19. TAN, Chaoliang, CAO, Xiehong, WU, Xue-jun, HE, Qiyuan, YANG, Jian, ZHANG, Xiao, CHEN, Junze, ZHAO, Wei, HAN, Shikui, NAM, Gwang-hyeon, SINDORO, Melinda and ZHANG, Hua. Recent Advances in Ultrathin Two-Dimensional Nanomaterials. *Chemical Reviews*. 2017. Vol. 117, p. 6225–6331. DOI 10.1021/acs.chemrev.6b00558.
 20. JIN, Huanyu, GUO, Chunxian, LIU, Xin, LIU, Jinlong, VASILE, Anthony, JIAO, Yan, ZHENG, Yao and QIAO, Shi-zhang. Emerging Two-Dimensional Nanomaterials for Electrocatalysis. *Chemical Reviews*. 2018. Vol. 118, p. 6337–6408 Review. DOI 10.1021/acs.chemrev.7b00689.
 21. LI, Zheling, CHU, Jingwen, YANG, Cheng, HAO, Sijia, BISSETT, Mark A,

- KINLOCH, Ian A and YOUNG, Robert J. Effect of functional groups on the agglomeration of graphene in nanocomposites. *Composites Science and Technology*. Online. 2018. Vol. 163, no. May, p. 116–122. DOI 10.1016/j.compscitech.2018.05.016.
22. SHAHZAD, Faisal, IQBAL, Aamir, KIM, Hyerim and KOO, Chong Min. 2D Transition Metal Carbides (MXenes): Applications as an Electrically Conducting Material. *Adv. Mater.* 2020. Vol. 32, no. 2002159, p. 1–23. DOI 10.1002/adma.202002159.
 23. WANG, Yijin, NIU, Bingqiang, ZHANG, Xingmao, LEI, Yimin, ZHONG, Peng and MA, Xiaohua. Review—Ti₃C₂T_x MXene: An Emerging Two-Dimensional Layered Material in Water Treatment. *ECS J. Solid State Sci. Technol.* 2021. Vol. 10, no. 047002. DOI 10.1149/2162-8777/abf2de.
 24. PIETZKA, M. A. and SCHUSTER, J. C. Summary of Constitutional Data on the Aluminum-Carbon-Titanium System. *Journal of Phase Equilibria*. 1994. Vol. 15, no. 4, p. 392–400. DOI <https://doi.org/10.1007/BF02647559>.
 25. LI, Shangshu, ZOU, Xingli, XIONG, Xiaolu, ZHENG, Kai, LU, Xionggang, ZHOU, Zhongfu, XIE, Xueliang and XU, Qian. Electrosynthesis of Ti₃AlC₂ from oxides/carbon precursor in molten calcium chloride. *Journal of Alloys and Compounds*. Online. 2018. Vol. 735, p. 1901–1907. DOI 10.1016/j.jallcom.2017.11.342.
 26. FENG, Aihu, YU, Yun, JIANG, Feng, WANG, Yong, MI, Le, YU, Yang and SONG, Lixin. Fabrication and thermal stability of NH₄HF₂-etched Ti₃C₂ MXene. *Ceramics International*. 2017. Vol. 43, no. 8, p. 6322–6328. DOI 10.1016/j.ceramint.2017.02.039.
 27. NAGUIB, Michael, MASHTALIR, Olha, CARLE, Joshua, PRESSER, Volker, LU, Jun, HULTMAN, Lars, GOGOTSI, Yury and BARSOUM, Michel W. Two-dimensional transition metal carbides. *ACS Nano*. 2012. Vol. 6, no. 2, p. 1322–1331. DOI 10.1021/nn204153h.
 28. NAGUIB, Michael, MOCHALIN, Vadym N., BARSOUM, Michel W. and GOGOTSI, Yury. 25th anniversary article: MXenes: A new family of two-dimensional materials. *Advanced Materials*. 2014. Vol. 26, no. 7, p. 992–1005. DOI 10.1002/adma.201304138.
 29. ZHANG, Tian, PAN, Limei, TANG, Huan, DU, Fei, GUO, Yanhua, QIU, Tai and YANG, Jian. Synthesis of two-dimensional Ti₃C₂T_xMXene using HCl+LiF etchant: Enhanced exfoliation and delamination. *Journal of Alloys and Compounds*. Online. 2017. Vol. 695, p. 818–826. DOI 10.1016/j.jallcom.2016.10.127.
 30. ALHABEB, Mohamed, MALESKI, Kathleen, ANASORI, Babak, LELYUKH, Pavel, CLARK, Leah, SIN, Saleesha and GOGOTSI, Yury. Guidelines for Synthesis and Processing of Two-Dimensional Titanium Carbide (Ti₃C₂T_x MXene). *Chem. Mater.* 2017. Vol. 29, p. 7633–7644. DOI 10.1021/acs.chemmater.7b02847.
 31. ZHANG, H., FU, Z. H., LEGUT, D., GERMANN, T. C. and ZHANG, R. F. Stacking stability and sliding mechanism in weakly bonded 2D transition

- metal carbides by van der Waals force. *RSC Adv.* 2017. Vol. 7, p. 55912. DOI 10.1039/c7ra11139h.
32. YAN, Jun, REN, Chang E, MALESKI, Kathleen, HATTER, Christine B, ANASORI, Babak, URBANKOWSKI, Patrick, SARYCHEVA, Asya and GOGOTSI, Yury. Flexible MXene/Graphene Films for Ultrafast Supercapacitors with Outstanding Volumetric Capacitance. *Adv. Funct. Mater.* 2017. Vol. 27, p. 1701264. DOI 10.1002/adfm.201701264.
 33. HOPE, Michael A., FORSE, Alexander C., GRIFFITH, Kent J., LUKATSKAYA, Maria R., GHIDIU, Michael, GOGOTSI, Yury and GREY, Clare P. NMR reveals the surface functionalisation of Ti_3C_2 MXene. *Phys. Chem. Chem. Phys.* 2016. Vol. 18, p. 5099–5102. DOI 10.1039/c6cp00330c.
 34. MALESKI, Kathleen, MOCHALIN, Vadym N. and GOGOTSI, Yury. Dispersions of Two-Dimensional Titanium Carbide MXene in Organic Solvents. *Chem. Mater.* 2017. Vol. 29, p. 1632–1640. DOI 10.1021/acs.chemmater.6b04830.
 35. MALESKI, Kathleen, REN, Chang E., ZHAO, Meng-Qiang, ANASORI, Babak and GOGOTSI, Yury. Size-Dependent Physical and Electrochemical Properties of Two-Dimensional MXene Flakes. *ACS Applied Materials and Interfaces.* 2018. Vol. 10, no. 29, p. 24491–24498. DOI 10.1021/acsami.8b04662.
 36. JASTRZEBSKA, A. M., SZUPLEWSKA, A., WOJCIECHOWSKI, T., CHUDY, M., ZIEMKOWSKA, W., CHLUBNY, L., ROZMYSŁOWSKA, A. and OLSZYNA, A. In vitro studies on cytotoxicity of delaminated Ti_3C_2 MXene. *Journal of Hazardous Materials.* 2017. Vol. 339, p. 1–8. DOI 10.1016/j.jhazmat.2017.06.004.
 37. MASHTALIR, Olha, NAGUIB, Michael, MOCHALIN, Vadym N., DALL'AGNESE, Yohan, HEON, Min, BARSOUM, Michel W. and GOGOTSI, Yury. Intercalation and delamination of layered carbides and carbonitrides. *Nature Communications.* 2013. Vol. 4, p. 1–7. DOI 10.1038/ncomms2664. asd
 38. LEVITT, Ariana, HEGH, Dylan, PHILLIPS, Patrick, UZUN, Simge, ANAYEE, Mark, RAZAL, Joselito M, GOGOTSI, Yury and DION, Genevieve. 3D knitted energy storage textiles using MXene-coated yarns. *Materials Today.* Online. 2020. Vol. 34, p. 17–29. DOI 10.1016/j.mattod.2020.02.005.
 39. LIPATOV, Alexey, ALHABEB, Mohamed, LUKATSKAYA, Maria R., BOSON, Alex, GOGOTSI, Yury and SINITSKII, Alexander. Effect of Synthesis on Quality, Electronic Properties and Environmental Stability of Individual Monolayer Ti_3C_2 MXene Flakes. *Advanced Electronic Materials.* 2016. Vol. 2, p. 1600255. DOI 10.1002/aelm.201600255.
 40. WANG, Xuefeng, SHEN, Xi, GAO, Yurui, WANG, Zhaoxiang, YU, Richeng and CHEN, Liquan. Atomic-Scale Recognition of Surface Structure and Intercalation Mechanism of $Ti_3C_2T_x$. *J. Am. Chem. Soc.* 2015. Vol. 137,

- p. 2715–2721. DOI 10.1021/ja512820k.
41. ZHANG, Jizhen, UZUN, Simge, SEYEDIN, Shayan, LYNCH, Peter A, AKUZUM, Bilen, WANG, Zhiyu, QIN, Si, ALHABEB, Mohamed, SHUCK, Christopher E, LEI, Weiwei, KUMBUR, E Caglan, YANG, Wenrong, WANG, Xungai, DION, Genevieve, RAZAL, Joselito M and GOGOTSI, Yury. Additive-Free MXene Liquid Crystals and Fibers. *ACS Cent. Sci.* 2020. Vol. 6, p. 254–265. DOI 10.1021/acscentsci.9b01217.
 42. SHEKHIREV, Mikhail, BUSA, Jeffrey, SHUCK, Christopher E, TORRES, Angel, BAGHERI, Saman, SINITSKII, Alexander and GOGOTSI, Yury. Ultralarge Flakes of $Ti_3C_2T_x$ MXene via Soft Delamination. *ACS Nano.* 2022. No. July 25. DOI 10.1021/acsnano.2c04506.
 43. JASTRZĘBSKA, Agnieszka Maria, KARWOWSKA, Ewa, WOJCIECHOWSKI, Tomasz, ZIEMKOWSKA, Wanda, ROZMYSŁOWSKA, Anita, CHLUBNY, Leszek and OLSZYNA, Andrzej. The Atomic Structure of Ti_2C and Ti_3C_2 MXenes is Responsible for Their Antibacterial Activity Toward *E. coli* Bacteria. *Journal of Materials Engineering and Performance.* 2018. No. Ref 16, p. 1–6. DOI 10.1007/s11665-018-3223-z.
 44. FENG, Wanlin, LUO, Heng, WANG, Yu, ZENG, Sifan, TAN, Yongqiang, ZHANG, Haibin and PENG, Shuming. Ultrasonic assisted etching and delaminating of Ti_3C_2 MXene. *Ceramics International.* Online. 2018. Vol. 44, no. 6, p. 7084–7087. DOI 10.1016/j.ceramint.2018.01.147.
 45. CHE, Lin, SHI, Xuguo, YU, Nanjie, ZHANG, Xing, DU, Xiaoze and LIN, Jun. Measurement and Analysis of Thermal Conductivity of $Ti_3C_2T_x$ MXene Films. *materials.* Online. 2018. Vol. 11, no. 1707. DOI 10.3390/ma11091701.
 46. CAO, Yong, DENG, Qihuang, LIU, Zhiduo, SHEN, Dianyu, WANG, Ting, HUANG, Qing, DU, Shiyu, JIANG, Nan, LIN, Cheng-Te and YU, Jinhong. Enhanced thermal properties of poly(vinylidene fluoride) composites with ultrathin nanosheets of MXene. *RSC Adv.* Online. 2017. Vol. 7, p. 20494–20501. DOI 10.1039/C7RA00184C.
 47. ZHU, Yue, ZHAO, Xingbin, PENG, Qingyu, ZHENG, Haowen, XUE, Fuhua, LI, Pengyang, XU, Zhonghai and HE, Xiaodong. Flame-retardant MXene/polyimide film with outstanding thermal and mechanical properties based on the secondary orientation strategy. *Nanoscale Adv.* 2021. Vol. 3, p. 5683–5693. DOI 10.1039/d1na00415h.
 48. WANG, Ning-ning, WANG, Hao, WANG, Yu-ying, WEI, You-hao, SI, Jing-yu, CHUN, Anthony, YUEN, Yin, XIE, Jin-song, YU, Bin, ZHU, San-e, LU, Hong-dian, YANG, Wei, CHAN, Qing Nian and YEOH, Guan-heng. Robust, Lightweight, Hydrophobic, and Fire-Retarded Polyimide/MXene Aerogels for Effective Oil/Water Separation. *ACS Appl. Mater. Interfaces.* 2019. Vol. 11, p. 40512–40523. DOI 10.1021/acsaami.9b14265.
 49. ZHANG, Chuanfang John, PINILLA, Sergio, MCEVOY, Niall, CULLEN, Conor P, ANASORI, Babak, LONG, Edmund, PARK, Sang-hoon, SERAL-

- ASCASO, Andrés, SHMELIOV, Aleksey, KRISHNAN, Dileep, MORANT, Carmen, LIU, Xinhua, DUESBERG, Georg S., GOGOTSI, Yury and NICOLOSI, Valeria. Oxidation Stability of Colloidal Two-Dimensional Titanium Carbides (MXenes). *Chem. Mater.* 2017. Vol. 29, p. 4848–4856. DOI 10.1021/acs.chemmater.7b00745.
50. CHAE, Yoonjeong, KIM, Seon Joon, CHO, Soo-Yeon, CHOI, Junghoon, MALESKI, Kathleen, LEE, Byeong-Joo, JUNG, Hee-Tae, GOGOTSI, Yury, LEE, Yonghee and AHN, Chi Won. An investigation into the factors governing the oxidation of two-dimensional Ti_3C_2 MXene. *Nanoscale*. 2019. Vol. 11, p. 8387–8393. DOI 10.1039/c9nr00084d.
51. HABIB, Touseef, ZHAO, Xiaofei, SHAH, Smit A, CHEN, Yexiao, SUN, Wanmei, AN, Hyosung, LUTKENHAUS, Jodie L, RADOVIC, Miladin and GREEN, Micah J. Oxidation stability of $Ti_3C_2T_x$ MXene nanosheets in solvents and composite films. *npj 2D Materials and Applications*. Online. 2019. Vol. 3, no. 8, p. 1–6. DOI 10.1038/s41699-019-0089-3.
52. LEE, Yonghee, KIM, Seon Joon, YONG-JAE KIM, YOUNGHWAN LIM, CHAE, Yoonjeong, LEE, Byeong-Joo, KIM, Young-Tae, HAN, Hee, GOGOTSI, Yury and AHN, Chi Won. Oxidation-resistant titanium carbide MXene films. *J. Mater. Chem. A*. 2020. Vol. 8, p. 573–581. DOI 10.1039/c9ta07036b.
53. IQBAL, Aamir, HONG, Junpyo, KO, Tae Yun and KOO, Chong Min. Improving oxidation stability of 2D MXenes: synthesis, storage media, and conditions. *Nano Convergence*. Online. 2021. Vol. 8, no. 9, p. 1–22. DOI 10.1186/s40580-021-00259-6.
54. ZHAO, Xiaofei, VASHISTH, Aniruddh, PREHN, Evan, SUN, Wanmei, SHAH, Smit A, HABIB, Touseef, CHEN, Yexiao, TAN, Zeyi, LUTKENHAUS, Jodie L, RADOVIC, Miladin and GREEN, Micah J. Antioxidants Unlock Shelf-Stable $Ti_3C_2T_x$ (MXene) Nanosheet Dispersions. *Matter*. Online. 2019. Vol. 1, p. 513–526. DOI 10.1016/j.matt.2019.05.020.
55. GIMENEZ, Raquel, SERRANO, Berna, SAN-MIGUEL, Ver and CABANELAS, Juan Carlos. Recent Advances in MXene/Epoxy Composites: Trends and Prospects. *Polymers*. 2022. Vol. 14, no. 1170, p. 1–29. DOI <https://doi.org/10.3390/polym14061170>.
56. NOVOSELOVA, Iuliia P, PETRUHINS, Andrejs, WIEDWALD, Ulf, WELLER, Dieter, FARLE, Michael and SALIKHOV, Ruslan. Long-term stability and thickness dependence of magnetism in thin $(Cr_{0.5}Mn_{0.5})_2GaC$ MAX phase films. *Materials Research Letters*. Online. 2019. Vol. 7, no. 4, p. 159–163. DOI 10.1080/21663831.2019.1570980.
57. SATHEESHKUMAR, Elumalai, MAKARYAN, Taron, MELIKYAN, Armen, MINASSIAN, Hayk, GOGOTSI, Yury and YOSHIMURA, Masahiro. One-step Solution Processing of Ag, Au and Pd@MXene Hybrids for SERS. *Scientific Reports*. Online. 2016. Vol. 6, no. 1, p. 32049. DOI 10.1038/srep32049.
58. GUARDIA, L., VILLAR-RODIL, S., PAREDES, J. I., ROZADA, R.,

- MARTI, A., MARTI'NEZ-ALONSO, A. and TASCÓN, J.M.D. UV light exposure of aqueous graphene oxide suspensions to promote their direct reduction, formation of graphene–metal nanoparticle hybrids and dye degradation. *Carbon*. 2012. Vol. 50, p. 1014–1024. DOI 10.1016/j.carbon.2011.10.005.
59. CHERTOPALOV, Sergii and MOCHALIN, Vadym N. Environment-Sensitive Photoresponse of Spontaneously Partially Oxidized Ti₃C₂ MXene Thin Films. *ACS Nano*. 2018. Vol. 12, p. 6109–6116. DOI 10.1021/acsnano.8b02379.
 60. YUN, Taeyeong, KIM, Hyerim, IQBAL, Aamir, CHO, Yong Soo, LEE, Gang San, KIM, Myung-ki, KIM, Seon Joon, KIM, Daesin, GOGOTSI, Yury, KIM, Sang Ouk and KOO, Chong Min. Electromagnetic Shielding of Monolayer MXene Assemblies. *Adv. Mater.* 2020. Vol. 32, no. 1906769, p. 1–9. DOI 10.1002/adma.201906769.
 61. BARGIR, Sameer, DUNN, Steve, JEFFERSON, Bruce, MACADAM, Jitka and PARSONS, Simon. The use of contact angle measurements to estimate the adhesion propensity of calcium carbonate to solid substrates in water. *Applied Surface Science*. 2009. Vol. 255, p. 4873–4879. DOI 10.1016/j.apsusc.2008.12.017.
 62. GHIDIU, Michael, LUKATSKAYA, Maria R, ZHAO, Meng-qiang, GOGOTSI, Yury and BARSOUM, Michel W. Conductive two-dimensional titanium carbide ‘clay’ with high volumetric capacitance. *Nature*. Online. 2014. Vol. 516, no. 7529, p. 78–81. DOI 10.1038/nature13970.
 63. KANG, Kyoung Min, KIM, Dae Woo, REN, Chang E., CHO, Kyeong Min, KIM, Seon Joon, CHOI, Jung Hoon, NAM, Yoon Tae, GOGOTSI, Yury and JUNG, Hee-tae. Selective Molecular Separation on Ti₃C₂T_x–Graphene Oxide Membranes during Pressure-Driven Filtration: Comparison with Graphene Oxide and MXenes. *ACS Applied Materials and Interfaces*. 2017. Vol. 9, p. 44687–44694. DOI 10.1021/acsmi.7b10932.
 64. MISHNAEVSKY JR., Leon and DAI, Gaoming. Hybrid and hierarchical nanoreinforced polymer composites: Computational modelling of structure–properties relationships. *COMPOSITE STRUCTURE*. Online. 2014. Vol. 117, p. 156–168. DOI 10.1016/j.compstruct.2014.06.027.
 65. DAI, Gaoming and MISHNAEVSKY JR., Leon. Graphene reinforced nanocomposites: 3D simulation of damage and fracture. *Computational Materials Science*. Online. 2014. Vol. 95, p. 684–692. DOI 10.1016/j.commatsci.2014.08.011.
 66. KILIKVICIUS, Sigita, KVIETKAITE, Saule, MISHNAEVSKY JR., Leon, OMASTOVÁ, Mária, ANISKEVICH, Andrey and ZELENIAKIENE, Daiva. Novel Hybrid Polymer Composites with Graphene and MXene Nano-Reinforcements: Computational Analysis. *Polymers*. 2021. Vol. 13, no. 1013, p. 1–12. DOI <https://doi.org/10.3390/polym13071013>.
 67. LING, Zheng, REN, Chang E., ZHAO, Meng-Qiang, YANG, Jian, GIAMMARCO, James M., QIU, Jieshan, BARSOUM, Michel W. and

- GOGOTSI, Yury. Flexible and conductive MXene films and nanocomposites with high capacitance. *PNAS*. Online. 2014. Vol. 111, no. 47, p. 16676–16681. DOI 10.1073/pnas.1414215111.
68. KILIKIČIUS, Sigitas, KVIETKAITĖ, Saulė, ŽUKIENĖ, Kristina, OMASTOVÁ, Mária, ANISKEVICH, Andrey and ZELENIAKIENĖ, Daiva. Numerical investigation of the mechanical properties of a novel hybrid polymer composite reinforced with graphene and MXene nanosheets. *Computational Materials Science*. Online. 2020. Vol. 174, no. August 2019, p. 109497. DOI 10.1016/j.commatsci.2019.109497.
 69. TALOUB, Nadia, HENNICHE, Abdelkhalek, LIU, Li, LI, Jun, RAHOUI, Nahla, HEGAZY, Mohammad and HUANG, Yudong. Improving the mechanical properties, UV and hydrothermal aging resistance of PIPD fiber using MXene ($\text{Ti}_3\text{C}_2(\text{OH})_2$) nanosheets. *Composites Part B*. Online. 2019. Vol. 163, no. October 2018, p. 260–271. DOI 10.1016/j.compositesb.2018.11.007.
 70. JIANG, Tao and ZHU, Yong. microscopy with a microsphere tip †. . 2015. P. 10760–10766. DOI 10.1039/c5nr02480c.
 71. BURNHAM, Nancy A, DOMINGUEZ, Dawn D, MOWERY, Robert L and COLTON, Richard J. Letters 16. . 1990. Vol. 64, no. 16, p. 1931–1934.
 72. CAPPELLA, Brunero and KAPPL, Michael. Force measurements with the atomic force microscope : Technique, interpretation and applications. . 2005. Vol. 59, p. 1–152. DOI 10.1016/j.surfrep.2005.08.003.
 73. ONLINE, View Article, ZHANG, H, FU, Z H, LEGUT, D, GERMANN, T C and ZHANG, R F. bonded 2D transition metal carbides by van der. . 2017. P. 55912–55919. DOI 10.1039/c7ra11139h.
 74. BORYSIUK, Vadym N., MOCHALIN, Vadym N. and GOGOTSI, Yury. Molecular dynamic study of the mechanical properties of two-dimensional titanium carbides $\text{Ti}_{n+1}\text{C}_n$ (MXenes). *Nanotechnology*. 2015. Vol. 26, no. 26, p. 1–10. DOI 10.1088/0957-4484/26/26/265705.
 75. LIPATOV, Alexey, LU, Haidong, ALHABEB, Mohamed, ANASORI, Babak, GRUVERMAN, Alexei, GOGOTSI, Yury and SINITSKII, Alexander. Elastic properties of 2D $\text{Ti}_3\text{C}_2\text{T}_x$ MXene monolayers and bilayers. *Science Advances*. Online. 2018. Vol. 4, no. 6, p. 1–7. DOI 10.1126/sciadv.aat0491.
 76. SANG, Xiahan, XIE, Yu, LIN, Ming-wei, ALHABEB, Mohamed, AKEN, Katherine L Van, GOGOTSI, Yury, KENT, Paul R C, XIAO, Kai and UNOCIC, Raymond R. Atomic Defects in Monolayer Titanium Carbide. . 2016. DOI 10.1021/acsnano.6b05240.
 77. PLUMMER, Gabriel, ANASORI, Babak, GOGOTSI, Yury and TUCKER, Garritt J. Nanoindentation of monolayer $\text{Ti}_{n+1}\text{C}_n\text{T}_x$ MXenes via atomistic simulations: The role of composition and defects on strength. *Computational Materials Science*. 2019. Vol. 157, no. November 2018, p. 168–174. DOI 10.1016/j.commatsci.2018.10.033.
 78. DAI, Gaoming and MISHNAEVSKY JR., Leon. Fatigue of multiscale

- composites with secondary nanoplatelet reinforcement: 3D computational analysis. *Composites Science and Technology*. Online. 2014. Vol. 91, p. 71–81. DOI 10.1016/j.compscitech.2013.11.024.
79. MISHNAEVSKY JR., Leon. Composite materials for wind energy applications: micromechanical modeling and future directions. *Comput Mech*. 2012. Vol. 50, p. 195–207. DOI 10.1007/s00466-012-0727-5.
 80. BORYSIUK, Vadym N., MOCHALIN, Vadym N. and GOGOTSI, Yury. Bending rigidity of two-dimensional titanium carbide (MXene) nanoribbons: A molecular dynamics study. *Computational Materials Science*. Online. 2018. Vol. 143, p. 418–424. DOI 10.1016/j.commatsci.2017.11.028.
 81. ZHAO, Jing, WANG, Guole, YANG, Rong, LU, Xiaobo, CHENG, Meng, HE, Congli, XIE, Guibai and MENG, Jianling. Tunable Piezoresistivity of Nanographene Films for Strain Sensing. . 2015. No. 2, p. 1622–1629. DOI 10.1021/nn506341u.
 82. YANG, Wei, LIU, Jun-Jie, WANG, Li-Li, WANG, Wei, YUEN, Anthony Chun Yin, YUEN, Yin, PENG, Shuhua, YU, Bin, LU, Hong-Dian, YEOH, Guan Heng and WANG, Chun-Hui. Multifunctional MXene/natural rubber composite films with exceptional flexibility and durability. *Composites Part B*. Online. 2020. Vol. 188, p. 107875. DOI 10.1016/j.compositesb.2020.107875.
 83. FAN, Zhimin, HE, Huaqing, YU, Jianxin, LIU, Li, LIU, Yuyan and XIE, Zhimin. Lightweight Three-Dimensional Cellular MXene Film for Superior Energy Storage and Electromagnetic Interference Shielding. *ACS Appl. Energy Mater*. 2020. DOI 10.1021/acsaem.0c01650.
 84. ZHANG, Jizhen, KONG, Na, UZUN, Simge, LEVITT, Ariana, SEYEDIN, Shayan, LYNCH, Peter A., QIN, Si, HAN, Meikang, YANG, Wenrong, LIU, Jingquan, WANG, Xungai, GOGOTSI, Yury and RAZAL, Joselito M. Scalable Manufacturing of Free-Standing , Strong $Ti_3C_2T_x$ MXene Films with Outstanding Conductivity. *Adv. Mater*. 2020. Vol. 32, p. 2001093. DOI 10.1002/adma.202001093.
 85. HATTER, Christine B., SHAH, Jay, ANASORI, Babak and GOGOTSI, Yury. Micromechanical response of two-dimensional transition metal carbonitride (MXene) reinforced epoxy composites. *Composites Part B*. Online. 2020. Vol. 182, no. November 2019, p. 107603. DOI 10.1016/j.compositesb.2019.107603.
 86. LIPATOV, Alexey, GOAD, Adam, LOES, Michael J., VOROBÉVA, Nataliia S., ABOURAHMA, Jehad, GOGOTSI, Yury and SINITSKII, Alexander. High electrical conductivity and breakdown current density of individual monolayer $Ti_3C_2T_x$ MXene flakes. *Matter*. Online. 2021. Vol. 4, p. 1413–1427. DOI 10.1016/j.matt.2021.01.021.
 87. ZHANG, Chuanfang John, ANASORI, Babak, SERAL-ASCASO, Andrés, PARK, Sang-hoon, MCEVOY, Niall, SHMELIOV, Aleksey, DUESBERG, Georg S, COLEMAN, Jonathan N, GOGOTSI, Yury and NICOLOSI, Valeria. Transparent, Flexible, and Conductive 2D Titanium Carbide

- (MXene) Films with High Volumetric Capacitance. *Adv. Mater.* 2017. Vol. 1702678, p. 1–9. DOI 10.1002/adma.201702678.
88. SHUCK, Christopher E, HAN, Meikang, MALESKI, Kathleen, HANTANASIRISAKUL, Kanit, KIM, Seon Joon, CHOI, Junghoon, REIL, William E B and GOGOTSI, Yury. Effect of Ti_3AlC_2 MAX Phase on Structure and Properties of Resultant $Ti_3C_2T_x$ MXene. *ACS Appl. Nano Mater.* 2019. Vol. 2, p. 3368–3376. DOI 10.1021/acsanm.9b00286.
89. MARIANO, Marina, MASHTALIR, Olha, ANTONIO, Francisco Q, RYU, Won-hee, DENG, Bingchen, XIA, Fengnian, GOGOTSI, Yury and TAYLOR, André D. Solution-processed titanium carbide MXene films examined as highly transparent conductors. *Nanoscale.* 2016. Vol. 8, p. 16371–16378. DOI 10.1039/c6nr03682a.
90. EOM, Wonsik, SHIN, Hwansoo, AMBADEI, Rohan B., LEE, Sang Hoon, LEE, Ki Hyun, KANG, Dong Jun and HAN, Tae Hee. Large-scale wet-spinning of highly electroconductive MXene fibers. *Nature Communications.* Online. 2020. Vol. 11, no. 2825, p. 1–7. DOI 10.1038/s41467-020-16671-1.
91. UZUN, Simge, SEYEDIN, Shayan, STOLTZFUS, Amy L, LEVITT, Ariana S, ALHABEB, Mohamed, ANAYEE, Mark, STROBEL, Christina J, RAZAL, Joselito M, DION, Genevieve and GOGOTSI, Yury. Knittable and Washable Multifunctional MXene-Coated Cellulose Yarns. *Adv. Funct. Mater.* 2019. Vol. 29, p. 1905015. DOI 10.1002/adfm.201905015.
92. SAMBYAL, Pradeep, IQBAL, Aamir, HONG, Junpyo, KIM, Hyerim, KIM, Myung-ki, HONG, Soon Man, HAN, Meikang, GOGOTSI, Yury and KOO, Chong Min. Ultralight and Mechanically Robust $Ti_3C_2T_x$ Hybrid Aerogel Reinforced by Carbon Nanotubes for Electromagnetic Interference Shielding. *ACS Appl. Mater. Interfaces.* 2019. Vol. 11, p. 38046–38054. DOI 10.1021/acsami.9b12550.
93. LUO, Jia-qi, ZHAO, Sai, ZHANG, Hao-bin, DENG, Zhiming, LI, Lulu and YU, Zhong-zhen. Flexible, stretchable and electrically conductive MXene/natural rubber nanocomposite films for efficient electromagnetic interference shielding. *Composites Science and Technology.* Online. 2019. Vol. 182, p. 107754. DOI 10.1016/j.compscitech.2019.107754.
94. CAO, Wen-tao, CHEN, Fei-fei, ZHU, Ying-jie, ZHANG, Yong-gang, JIANG, Ying-ying and CHEN, Feng. Binary Strengthening and Toughening of MXene/Cellulose Nanofiber Composite Paper with Nacre-Inspired Structure and Superior Electromagnetic Interference Shielding Properties. *ACS Nano.* 2018. Vol. 12, p. 4583–4593. DOI 10.1021/acs.nano.8b00997.
95. NAGUIB, Michael, SAITO, Tomonori, LAI, Sophia, RAGER, Matthew S., AYTUG, Tolga, PARANTHAMAN, M. Parans, ZHAOC, Meng-Qiang and GOGOTSI, Yury. $Ti_3C_2T_x$ (MXene)–polyacrylamide nanocomposite films. *RSC Adv.* 2016. Vol. 6, p. 72069–72073. DOI 10.1039/c6ra10384g.
96. FENG, Ailing, HOU, Tianqi, JIA, Zirui, ZHANG, Yi, ZHANG, Fan and WU, Guanglei. Preparation and Characterization of Epoxy Resin Filled with $Ti_3C_2T_x$ MXene Nanosheets with Excellent Electric Conductivity.

- Nanomaterials*. 2020. Vol. 10, no. 162, p. 1–11.
DOI doi:10.3390/nano10010162.
97. LYDIA, M, KUMAR, S Suresh, SELVAKUMAR, A Immanuel and PREM, G Edwin. A comprehensive review on wind turbine power curve modeling techniques. *Renewable and Sustainable Energy Reviews*. 2014. Vol. 30, p. 452–460. DOI 10.1016/j.rser.2013.10.030.
 98. LI, Feiyu, CUI, Hongmei, SU, Hongjie, MA, Zhipeng, ZHU, Yaxiong and ZHANG, Yong. Icing condition prediction of wind turbine blade by using artificial neural network based on modal frequency. *Cold Regions Science and Technology*. Online. 2022. Vol. 194, p. 103467.
DOI 10.1016/j.coldregions.2021.103467.
 99. PÉREZ, Marco A, PERNAS-SÁNCHEZ, J, ARTERO-GUERRERO, J A and SERRA-LÓPEZ, Roger. High-velocity ice impact damage quantification in composite laminates using a frequency domain-based correlation approach. *Mechanical Systems and Signal Processing*. 2021. Vol. 147, p. 107124.
DOI 10.1016/j.ymsp.2020.107124.
 100. DALILI, N, EDRISY, A and CARRIVEAU, R. A review of surface engineering issues critical to wind turbine performance. *Renewable and Sustainable Energy Reviews*. 2009. Vol. 13, p. 428–438.
DOI 10.1016/j.rser.2007.11.009.
 101. WANG, L, KOLIOS, A, LIU, X, VENETSANOS, D and RUI, C. Reliability of offshore wind turbine support structures: A state-of-the-art review. *Renewable and Sustainable Energy Reviews*. Online. 2022. Vol. 161, no. April 2020, p. 112250. DOI 10.1016/j.rser.2022.112250.
 102. LIU, Hu, LI, Qianming, ZHANG, Shuaidi, YIN, Rui, LIU, Xianhu, HE, Yuxin, DAI, Kun, SHAN, Chongxin, GUO, Jiang, LIU, Chuntai, SHEN, Changyu, WANG, Xiaojing, WANG, Ning, WANG, Zicheng, WEI, Renbo and GUO, Zhanhu. Electrically conductive polymer composites for smart flexible strain sensors : a critical review. *J. Mater. Chem. C*. 2018. Vol. 6, p. 12121–12141. DOI 10.1039/c8tc04079f.
 103. WANG, Binghao and FACCHETTI, Antonio. Mechanically Flexible Conductors for Stretchable and Wearable E-Skin and E-Textile Devices. *Adv. Mater.* 2019. P. 1901408. DOI 10.1002/adma.201901408.
 104. ORANGI, Jafar, HAMADE, Fatima, DAVIS, Virginia A and BEIDAGHI, Majid. 3D Printing of Additive-Free 2D $Ti_3C_2T_x$ (MXene) Ink for Fabrication of Micro- Supercapacitors with Ultra-High Energy Densities. *ACS Nano*. 2020. Vol. 14, p. 640–650. DOI 10.1021/acsnano.9b07325.
 105. CHENG, Yongfa, MA, Yanan, LI, Luying, ZHU, Meng, YUE, Yang, LIU, Weijie, WANG, Longfei and JIA, Shuangfeng. Bioinspired Microspines for a High-Performance Spray $Ti_3C_2T_x$ MXene-Based Piezoresistive Sensor. . 2020. Vol. 14, p. 2145–2155. DOI 10.1021/acsnano.9b08952.
 106. ZHAO, Meng-Qiang, TRAINOR, Nicholas, REN, Chang E., TORELLI, Michelle, ANASORI, Babak and GOGOTSI, Yury. Scalable Manufacturing of Large and Flexible Sheets of MXene/Graphene Heterostructures. *Adv.*

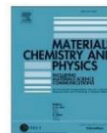
- Mater. Technol.* 2019. Vol. 4, p. 1800639. DOI 10.1002/admt.201800639.
107. WAN, Yan-jun, LI, Xing-miao, ZHU, Peng-li, SUN, Rong, WONG, Ching-ping and LIAO, Wei-Hsin. Lightweight , flexible MXene/polymer film with simultaneously excellent mechanical property and high-performance electromagnetic interference shielding. *Composites Part A*. Online. 2020. Vol. 130, p. 105764. DOI 10.1016/j.compositesa.2020.105764.
 108. YANG, Yina, SHI, Liangjing, CAO, Zherui, WANG, Ranran and SUN, Jing. Strain Sensors with a High Sensitivity and a Wide Sensing Range Based on a $Ti_3C_2T_x$ (MXene) Nanoparticle–Nanosheet Hybrid Network. *Adv. Funct. Mater.* 2019. Vol. 29, p. 1807882. DOI 10.1002/adfm.201807882.
 109. CLARK, Kendal W, ZHANG, X, VLASSIOUK, Ivan V, HE, Guowei, FEENSTRA, Randall M and LI, An-ping. Spatially Resolved Mapping of Electrical Conductivity across Individual Domain (Grain) Boundaries in Graphene. *ACS Nano*. 2013. Vol. 7, no. 9, p. 7956–7966. DOI 10.1021/nn403056k.
 110. LU, Xiaoxin, YVONNET, Julien, DETREZ, Fabrice and BAI, Jinbo. Multiscale modeling of nonlinear electric conductivity in graphene-reinforced nanocomposites taking into account tunnelling effect. *Journal of Computational Physics*. Online. 2017. Vol. 337, p. 116–131. DOI 10.1016/j.jcp.2017.01.063.
 111. HU, Ning, KARUBE, Yoshifumi, YAN, Cheng, MASUDA, Zen and FUKUNAGA, Hisao. Tunneling effect in a polymer/carbon nanotube nanocomposite strain sensor. *Acta Materialia*. 2008. Vol. 56, p. 2929–2936. DOI 10.1016/j.actamat.2008.02.030.
 112. DENG, Fei and ZHENG, Quan-Shui. An analytical model of effective electrical conductivity of carbon nanotube composites. *Appl. Phys. Lett.* 2008. Vol. 92, p. 071902. DOI 10.1063/1.2857468.
 113. CHANDRA, Y, ADHIKARI, S, FLORES, E I Saavedra and FIGIEL, Ł. Advances in finite element modelling of graphene and associated nanostructures. *Materials Science & Engineering R*. Online. 2020. Vol. 140, no. January, p. 100544. DOI 10.1016/j.mser.2020.100544.
 114. ZARE, Yasser and RHEE, Kyong Yop. Development of a Model for Electrical Conductivity of Polymer/Graphene Nanocomposites Assuming Interphase and Tunneling Regions in Conductive Networks. *Ind. Eng. Chem. Res.* 2017,. 2017. Vol. 56, p. 9107–9115. DOI 10.1021/acs.iecr.7b01348.
 115. RIZZI, Leo, ZIENERT, Andreas, SCHUSTER, Jörg, KÖHNE, Martin and SCHULZ, Stefan E. Electrical Conductivity Modeling of Graphene-based Conductor Materials. *ACS Appl. Mater. Interfaces*. 2018. Vol. 10, p. 43088–43094. DOI 10.1021/acsami.8b16361.
 116. ZHANG, Ye, CHANG, Ting-Hsiang, JING, Lin, LI, Kerui, YANG, Haitao and CHEN, Po-Yen. Heterogeneous, 3D Architecturing of 2D Titanium Carbide (MXene) for Microdroplet Manipulation and Voice Recognition. *ACS Appl. Mater. Interfaces*. 2020. Vol. 12, p. 8392–8402. DOI 10.1021/acsami.9b18879.

117. LIU, Qiang, CHEN, Ji, LI, Yingru and SHI, Gaoquan. High-Performance Strain Sensors with Fish-Scale-Like Graphene-Sensing Layers for Full-Range Detection of Human Motions. *ACS Nano*. 2016. Vol. 10, p. 7901–7906. DOI 10.1021/acsnano.6b03813.
118. KANG, Daeshik, PIKHITSA, Peter V., CHOI, Yong Whan, LEE, Chanseok, SHIN, Sung Soo, PIAO, Linfeng, PARK, Byeonghak, SUH, Kahp-Yang, KIM, Tae-il and CHOI, Mansoo. Ultrasensitive mechanical crack-based sensor inspired by the spider sensory system. *Nature*. Online. 2014. Vol. 516, p. 222–226. DOI 10.1038/nature14002.
119. SHI, Xinlei, WANG, Huike, XIE, Xueting, XUE, Qingwen, ZHANG, Jingyu, KANG, Siqi, WANG, Conghui, LIANG, Jiajie and CHEN, Yongsheng. Bioinspired Ultrasensitive and Stretchable MXene-Based Strain Sensor via Nacre-Mimetic Microscale “Brick-and-Mortar” Architecture. *ACS Nano*. 2019. Vol. 13, p. 649–659. DOI 10.1021/acsnano.8b07805.
120. SHI, Xinlei, LIU, Shuiren, SUN, Yang, LIANG, Jiajie and CHEN, Yongsheng. Lowering Internal Friction of 0D–1D–2D Ternary Nanocomposite-Based Strain Sensor by Fullerene to Boost the Sensing Performance. *Adv. Funct. Mater.* 2018. Vol. 28, p. 1800850. DOI 10.1002/adfm.201800850.
121. GEORGOUSIS, G, PANDIS, C, KALAMIOTIS, A, GEORGIPOULOS, P, KYRITSIS, A, KONTOU, E, PISSIS, P, MICUSIK, M., CZANIKOVA, K., KULICEK, J. and OMASTOVÁ, M. Strain sensing in polymer/carbon nanotube composites by electrical resistance measurement. *COMPOSITES PART B*. Online. 2015. Vol. 68, p. 162–169. DOI 10.1016/j.compositesb.2014.08.027.
122. SEYEDIN, Shayan, UZUN, Simge, LEVITT, Ariana, ANASORI, Babak, DION, Genevieve, GOGOTSI, Yury and RAZAL, Joselito M. MXene Composite and Coaxial Fibers with High Stretchability and Conductivity for Wearable Strain Sensing Textiles. *Adv. Funct. Mater.* 2020. Vol. 30, p. 1910504. DOI 10.1002/adfm.201910504.
123. LEE, Taemin, MIN, Sa Hoon, GU, Minsu, JUNG, Yun Kyung, LEE, Wonoh, LEE, Jea Uk, SEONG, Dong Gi and KIM, Byeong-su. Layer-by-Layer Assembly for Graphene-Based Multilayer Nanocomposites: Synthesis and Applications. *Chem. Mater.* 2015. Vol. 27, p. 3785–3796. DOI 10.1021/acs.chemmater.5b00491.
124. CAI, Yichen, SHEN, Jie, GE, Gang, ZHANG, Yizhou, JIN, Wanqin, HUANG, Wei, SHAO, Jinjun, YANG, Jian and DONG, Xiaochen. Stretchable $Ti_3C_2T_x$ MXene/Carbon Nanotube Composite Based Strain Sensor with Ultrahigh Sensitivity and Tunable Sensing Range. *ACS Nano*. 2018. Vol. 12, p. 56–62. DOI 10.1021/acsnano.7b06251.
125. YANG, Yina, CAO, Zherui, HE, Peng, SHI, Liangjing, DING, Guqiao, WANG, Ranran and SUN, Jing. $Ti_3C_2T_x$ MXene-graphene composite films for wearable strain sensors featured with high sensitivity and large range of linear response. *Nano Energy*. Online. 2019. Vol. 66, no. September,

- p. 104134. DOI 10.1016/j.nanoen.2019.104134.
126. CUI, Cong, CHENG, Renfei, ZHANG, Hui, ZHANG, Chao, MA, Yonghui, SHI, Chao, FAN, Bingbing, WANG, Hailong and WANG, Xiaohui. Ultrastable MXene @Pt/SWCNTs ' Nanocatalysts for Hydrogen Evolution Reaction. *Adv. Funct. Mater.* 2020. Vol. 2000693, p. 1–8. DOI 10.1002/adfm.202000693.
 127. WANG, Lin, ZHANG, Meiyun, YANG, Bin, TAN, Jiaojun and DING, Xueyao. Highly Compressible, Thermally Stable, Light- Weight, and Robust Aramid Nano fibers/Ti₃AlC₂ MXene Composite Aerogel for Sensitive Pressure Sensor. *ACS Nano.* 2020. Vol. 14, p. 10633–10647. DOI 10.1021/acsnano.0c04888.
 128. BOOTA, Muhammad, ANASORI, Babak, VOIGT, Cooper, ZHAO, Meng-qiang, BARSOUM, Michel W and GOGOTSI, Yury. Pseudocapacitive Electrodes Produced by Oxidant-Free Polymerization of Pyrrole between the Layers of 2D Titanium Carbide (MXene). *Adv. Mater.* 2016. Vol. 28, p. 1517–1522. DOI 10.1002/adma.201504705.
 129. WANG, Zhiyu, QIN, Si, SEYEDIN, Shayan, ZHANG, Jizhen, WANG, Jiangting, LEVITT, Ariana, LI, Na, HAINES, Carter, OVALLE-ROBLES, Raquel, LEI, Weiwei, GOGOTSI, Yury, BAUGHMAN, Ray H and RAZAL, Joselito M. High-Performance Biscrolled MXene/Carbon Nanotube Yarn Supercapacitors. *Small.* 2018. Vol. 14, p. 1802225. DOI 10.1002/smll.201802225.
 130. YUN, Taeyeong, KIM, Hyerim, IQBAL, Aamir, CHO, Yong Soo, LEE, Gang San, KIM, Myung-ki, KIM, Seon Joon, KIM, Daesin, GOGOTSI, Yury, KIM, Sang Ouk and KOO, Chong Min. Electromagnetic Shielding of Monolayer MXene Assemblies. *Advanced Materials.* 2020. Vol. 32, p. 1906769. DOI 10.1002/adma.201906769.
 131. SHAHZAD, Faisal, ALHABEB, Mohamed, HATTER, Christine B., ANASORI, Babak, HONG, Soon Man, KOO, Chong Min and GOGOTSI, Yury. Electromagnetic interference shielding with 2D transition metal carbides (MXenes). *Science.* 2016. Vol. 353, no. 6304, p. 1137–1140. DOI 10.1126/science.aag2421.
 132. LI, Lei, CAO, Yanxia, LIU, Xiaoya, WANG, Jianfeng, YANG, Yanyu and WANG, Wanjie. Multifunctional MXene-Based Fireproof Electromagnetic Shielding Films with Exceptional Anisotropic Heat Dissipation Capability and Joule Heating Performance. *ACS Appl. Mater. Interfaces.* 2020. Vol. 12, p. 27350–27360. DOI 10.1021/acсами.0c05692.
 133. TANG, Honghao, FENG, Huanran, WANG, Huike, WAN, Xiangjian, LIANG, Jiajie and CHEN, Yongsheng. Highly Conducting MXene–Silver Nanowire Transparent Electrodes for Flexible Organic Solar Cells. *ACS Appl. Mater. Interfaces.* 2019. Vol. 11, p. 25330–25337. DOI 10.1021/acсами.9b04113.
 134. TIAN, Yuan, AN, Yongling and FENG, Jinkui. Flexible and Freestanding Silicon/MXene Composite Papers for High-Performance Lithium-Ion

- Batteries. *ACS Appl. Mater. Interfaces*. 2019. Vol. 11, p. 10004–10011. DOI 10.1021/acsami.8b21893.
135. LIU, Yi-tao, ZHANG, Peng, SUN, Ning, ANASORI, Babak, ZHU, Qi-zhen, LIU, Huan, GOGOTSI, Yury and XU, Bin. Self-Assembly of Transition Metal Oxide Nanostructures on MXene Nanosheets for Fast and Stable Lithium Storage. *Adv. Mater.* 2018. Vol. 30, p. 1707334. DOI 10.1002/adma.201707334.
 136. ALI, Razium, JAWAID, Sana, ZHU, Qizhen, ABBAS, Zaheer and XU, Bin. A mini-review on MXenes as versatile substrate for advanced sensors. *Chinese Chemical Letters*. Online. 2019. DOI 10.1016/j.ccllet.2019.12.005.
 137. KOH, Hyeong-jun, KIM, Seon Joon, MALESKI, Kathleen, CHO, Soo-yeon, KIM, Yong-jae, AHN, Chi Won, GOGOTSI, Yury and JUNG, Hee-tae. Enhanced Selectivity of MXene Gas Sensors through Metal Ion Intercalation: In Situ X-ray Diffraction Study. *ACS Sensors*. 2019. Vol. 4, p. 1365–1372. DOI 10.1021/acssensors.9b00310.
 138. KIM, Seon Joon, KOH, Hyeong-Jun, REN, Chang E., KWON, Ohmin, MALESKI, Kathleen, CHO, Soo-yeon, ANASORI, Babak, KIM, Choong-ki, CHOI, Yang-kyu, KIM, Jihan, GOGOTSI, Yury and JUNG, Hee-Tae. Metallic $Ti_3C_2T_x$ MXene Gas Sensors with Ultrahigh Signal-to-Noise Ratio. *ACS Nano*. 2018. Vol. 12, p. 986–993. DOI 10.1021/acsnano.7b07460.
 139. AN, Hyosung, HABIB, Touseef, SHAH, Smit, GAO, Huili, PATEL, Anish, ECHOLS, Ian, ZHAO, Xiaofei, RADOVIC, Miladin, GREEN, Micah J. and LUTKENHAUS, Jodie L. Water Sorption in MXene/Polyelectrolyte Multilayers for Ultrafast Humidity Sensing. *ACS Appl. Nano Mater.* 2019. Vol. 2, p. 948–955. DOI 10.1021/acsanm.8b02265.
 140. JIN, Jia Yi and VIRK, Muhammad Shakeel. Study of ice accretion and icing effects on aerodynamic characteristics of DU96 wind turbine blade profile. *Cold Regions Science and Technology*. 2019. Vol. 160, no. September 2018, p. 119–127. DOI 10.1016/j.coldregions.2019.01.011.
 141. STOYANOV, D B and NIXON, J D. Alternative operational strategies for wind turbines in cold climates. *Renewable Energy*. Online. 2020. Vol. 145, p. 2694–2706. DOI 10.1016/j.renene.2019.08.023.
 142. MADI, Ezieddin, POPE, Kevin, HUANG, Weimin and IQBAL, Tariq. A review of integrating ice detection and mitigation for wind turbine blades. *Renewable and Sustainable Energy Reviews*. Online. 2019. Vol. 103, no. November 2018, p. 269–281. DOI 10.1016/j.rser.2018.12.019.
 143. BOOPATHI, Kadhivel, MISHNAEVSKY JR., Leon, SUMANTRAA, Bose, PREMKUMAR, S. Anthonyraj, THAMODHARAN, Krishnaraj and BALARAMAN, Kannan. Failure mechanisms of wind turbine blades in India: Climatic , regional , and seasonal variability. *Wind Energy*. 2022. P. 1–12. DOI 10.1002/we.2706.
 144. PARENT, Olivier and ILINCA, Adrian. Anti-icing and de-icing techniques for wind turbines: Critical review. *Cold Regions Science and Technology*. 2011. Vol. 65, no. 1, p. 88–96. DOI 10.1016/j.coldregions.2010.01.005.

145. KARIM, Nazmul, ZHANG, Minglonghai, AFROJ, Shaila, KONCHERRY, Vivek, POTLURI, Prasad and NOVOSELOV, Kostya S. Graphene-based surface heater for de-icing applications. *RSC Adv.* 2018. Vol. 8, p. 16815–16823. DOI 10.1039/c8ra02567c.
146. YAO, Xudan, HAWKINS, Stephen C and FALZON, Brian G. An advanced anti-icing / de-icing system utilizing highly aligned carbon nanotube webs. *Carbon.* Online. 2018. Vol. 136, p. 130–138. DOI 10.1016/j.carbon.2018.04.039.
147. REDONDO, O, PROLONGO, S G, CAMPO, M, SBARUFATTI, C and GIGLIO, M. Anti-icing and de-icing coatings based Joule’s heating of graphene nanoplatelets. *Composites Science and Technology.* Online. 2018. Vol. 164, no. May, p. 65–73. DOI 10.1016/j.compscitech.2018.05.031.
148. JIA, Xichen, SHEN, Bin, ZHANG, Lihua and ZHENG, Wenge. Waterproof MXene-decorated wood-pulp fabrics for high-efficiency electromagnetic interference shielding and Joule heating. *Composites Part B.* Online. 2020. Vol. 198, no. July, p. 108250. DOI 10.1016/j.compositesb.2020.108250.



Wettability of MXene and its interfacial adhesion with epoxy resin

K. Zukienė^a, G. Monastyreckis^{a,*}, S. Kilikevicius^a, M. Procházka^b, M. Micusik^b, M. Omastová^b, A. Aniskevich^c, D. Zeleniakienė^a

^a Department of Mechanical Engineering, Kaunas University of Technology, Studentų Str. 56, 51424, Kaunas, Lithuania

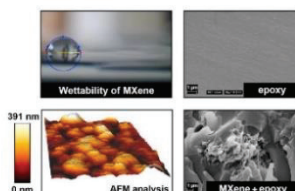
^b Polymer Institute, Slovak Academy of Sciences, Džbavská Cesta 9, Bratislava 45, 845 41, Slovakia

^c Institute for Mechanics of Materials, University of Latvia, Jelgavas Str. 3, Rīga, LV 1004, Latvia

HIGHLIGHTS

- Two-dimensional $\text{Ti}_3\text{C}_2\text{T}_x$ MXene nano-materials were synthesized and characterized.
- The surface energy and topography of $\text{Ti}_3\text{C}_2\text{T}_x$ MXene coatings supported on the glass substrate were estimated.
- The thermodynamic work of adhesion of MXene–epoxy nanocomposites was determined.

GRAPHICAL ABSTRACT



ARTICLE INFO

Keywords:
MXene
XPS
Polymer nanocomposites
Interfacial adhesion

ABSTRACT

The surface energies of MXene nanofillers critically affect the mechanical properties and durability of any polymer-based devices and composites to which these fillers are applied. In this context, this study comprehensively investigates $\text{Ti}_3\text{C}_2\text{T}_x$ MXenes prepared via the hydrochloric acid/lithium fluoride etching of Ti_2AlC_2 . The surface energy values of 10-layer MXene coatings were evaluated to be between 47.98 and 64.48 mJ/m² as per contact-angle measurements. The wettability properties were found to depend on the number of coating layers and the liquids used. Additionally, the coating roughness was evaluated by using atomic force microscopy. The effectiveness of MXenes as a reinforcing nanofiller for polymer matrix was investigated by utilising an epoxy resin. The work of adhesion between the MXene and epoxy was calculated to be up to 123.6 mJ/m². The prediction of a high adhesion was also confirmed with the use of scanning electron microscopy images to examine the fractured surface of the MXene–epoxy specimens.

1. Introduction

The outstanding reinforcement effects of nanofillers in polymer-based composites is related to their high specific surface area, superior mechanical properties, and strong filler–matrix interfacial adhesion. In this regard, two-dimensional (2D) nanomaterials have recently received

significant attention from academia and industries [1–3]. One such 2D nanoparticle is MXene [4,5], which consists of transition metal carbides, nitrides, and carbonitrides. Merits such as high conductivity, hydrophilicity, catalytic activity, and excellent thermal and mechanical properties [6–11] render MXene particles a potential material for several important applications. MXene and polymer matrix composites

* Corresponding author.

E-mail address: gediminas.monastyreckis@ktu.edu (G. Monastyreckis).

<https://doi.org/10.1016/j.matchemphys.2020.123820>

Received 3 July 2020; Received in revised form 15 August 2020; Accepted 8 September 2020

Available online 14 September 2020

0254-0584/© 2020 Elsevier B.V. All rights reserved.

Table 1
Force components of surface energy (mJ/m²) of test liquids [38].

Liquid	γ_1	γ_1^d	γ_1^p
Diiodomethane	50.8	49.5	1.3
Water	72.8	21.8	51.0
Glycerol	63.4	37.0	26.0

are considered promising industrial products for their varying utilities [12–14] including wearable electronics, energy storage devices, electromagnetic shielding, electrochemical actuators, and various sensors [15–22]. Poly (diallyldimethylammonium chloride) (PDDA), polyvinyl alcohol (PVA), poly (methyl methacrylate) (PMMA), and epoxy resin are some examples of polymer matrices used in the preparation of such composites. In this regard, Ling et al. [23] investigated Ti₃C₂T_x-PDDA and Ti₃C₂T_x-PVA composites and found that similar to pure Ti₃C₂T_x films and Ti₃C₂T_x-PDDA composites exhibit impressive flexibility and conductivity, whereas Ti₃C₂T_x-PVA composites demonstrate improved tensile strength. In another research [24], the authors introduced only 0.3 wt fraction (wt%) of exfoliated Ti₃Si_{0.75}Al_{0.25}C₂ nanosheets in PMMA, which resulted in significant improvements in the mechanical and thermal properties of PMMA. Moreover, Young's modulus and ultimate tensile strength of the Ti₃Si_{0.75}Al_{0.25}C₂/PMMA composites were approximately fivefold and twofold higher than their pure PMMA film counterparts, respectively.

Meanwhile, MXene-epoxy nanocomposites with improved electrical and thermal conductivities have also been investigated [25–27]. Furthermore, finite element simulations of the mechanical properties of MXene-epoxy nanocomposites have shown that the alignment of MXene nanosheets significantly increases the matrix elastic properties and the ultimate tensile strength [28,29]. A model with 30 vol% MXenes exhibited an increase in Young's modulus and tensile strength by factors of 8.4 and 1.91 times, respectively, when compared with the corresponding values for pure epoxy. According to simulations, the mechanical performance of the MXene-polymer composite can be maximised when the load is effectively transferred from the matrix to the nanoparticle. This can be achieved when a strong interfacial adhesion exists between the polymer matrix and MXene. The presence of abundant hydrophilic functional groups such as hydroxyl and carbonyl groups on the MXene surface can ensure strong adhesion at the MXene-matrix interface. The interfacial adhesion also depends on the MXene surface energy, which can be evaluated by using contact angle measurements. In this regard, the water contact angle on a rolled MXene film was measured to be 21.5° by Ghidui et al. [30], which confirms the hydrophilic nature of the MXene films. Moreover, Kang reported a significantly higher value of water wetting angle (62°) for MXene film produced by pressure-driven filtration [31].

Although the surface energies of various polymers are well characterised, that of MXene has not been investigated with regard to epoxy matrices. In this context, this study aims to determine the surface energy

and interfacial adhesion between MXene and epoxy resin.

2. Material and methods

2.1. Synthesis of MXenes

MXenes were prepared using Ti₃AlC₂ MAX phase 347 (MRC, Ukraine) with a particle size of <40 μm and purity of 98 wt%, applying the protocol published by Alhabeb et al. [32]. The etching solvents of 37 wt% hydrochloric acid (Merck, Germany) and lithium fluoride (LiF, >99 wt%) were provided by Sigma Aldrich (Germany). LiF was mixed with HCl to generate HF in the system. Next, the MAX phase was added slowly, and the suspension was stirred for the next 24 h. After the reaction, the resulting solution was centrifuged several times at 3500 rpm and then washed with deionised water until the pH of the supernatant reached a value of 6. Characterisation of prepared MXene (Raman spectra, AFM, etc.) was published elsewhere [33].

2.2. MXene coating preparation

The Ti₃C₂T_x MXene aqueous solution was centrifuged and washed several times with ultrapure deionised water until MXene batch concentration reached 30 wt%. MXene coatings were prepared by using motorised glass specimens (3 × 2 cm), which were dipped into a dispersed solution of 3 wt% MXenes. Each dipping procedure was performed with a 10 s steady vertical pull-out and 10 min of drying, which led to the formation of one MXene coating layer. This procedure was repeated up to 10 times.

2.3. MXene-epoxy composite preparation

The thermosetting epoxy resin Bisphenol F-(epichlorohydrin) with average molecular weight <700 (Biresin® CR122, Sika, Germany), in conjunction with the hardener 3-Aminomethyl-3,5,5-

Table 2
Surface chemical compositions of MAX phase and MXene.

Material	Surface chemical composition [at%]				
	Cl1s Ti ₃ C ₂ /1/II sp ³ /CO/ OCO	O1s ox I/II/III	Ti2p Ti ₃ C ₂ /I/II TiO ₂	F1s F ⁻ /TF ² TiOF/ C-F	Al2p/ Cl2p Ni1s/S2p
MAX phase	22.5	44.2	16.7	0.7	12.8/0.3
	6.5/0.3/1.7	24.0	4.9/2.5/	0.6/-	2.3/0.5
	9.2/2.6/2.2	6.9/12.4/	1.9	-/0.1	
MXene		0.9	7.4		
	30.0	23.7	25.9	16.4	-/2.8
	9.4/2.1/7.4	4.5	7.7/4.8/	0.6/10.3	1.3/-
	6.7/2.9/1.5	14.0/4.1/	6.3	4.7/0.8	
	1.1	7.1			

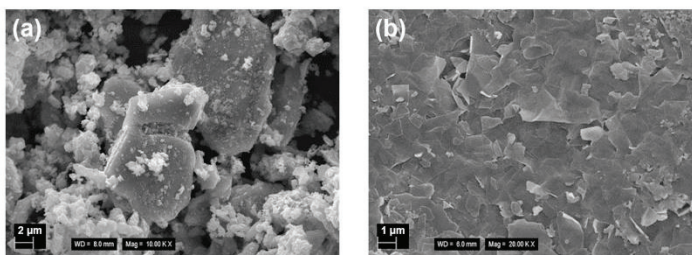


Fig. 1. SEM images of (a) MAX phase Ti₃AlC₂ powder, (b) Ti₃C₂T_x MXene nanoparticles.

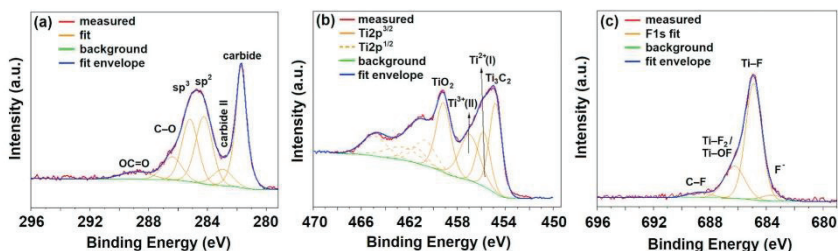


Fig. 2. XPS results corresponding to (a) C1s region, (b) Ti2p region, and (c) F1s region of MXene.

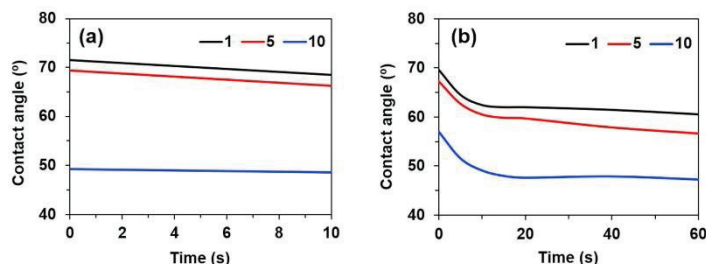


Fig. 3. Contact angles of (a) water and (b) glycerol on different numbers of MXene coating layers.

Table 3

Average contact angles (degrees) for different numbers of MXene coating layers on glass surface.

Number of layers	Water	Diiodomethane	Glycerol
1	68.40 ± 1.2	38.43 ± 1.1	60.57 ± 0.8
5	66.20 ± 0.7	30.05 ± 0.9	56.63 ± 1.2
10	48.50 ± 0.8	29.95 ± 0.5	47.27 ± 1.3

trimethylcyclohexylamin; 4,4'Methylenbis (cyclohexylamin); Cyclohex-1,2-ylendiamin (Biresin® CH122-5, Sika, Germany) with the mixing ratio of 10:3, was used in the study. For surface-energy estimation, the MXene-epoxy composites with a filler loading of 1 wt% were prepared by means of the following method: 30 wt% aqueous batch of MXenes was mixed with the curing agent with the use of a mechanical stirrer at 800 rpm for 1.5 h and degassed at 60 °C for 24 h under vacuum. Next, the epoxy resin was stirred with MXene-hardener mixture. The mixture was cast in silicone moulds, cured for 24 h at room temperature, and post-cured at 80 °C for 5 h in a convection oven.

2.4. Characterisation methods

2.4.1. Scanning electron microscopy

The morphologies of the MAX phase and MXene were studied by means of scanning electron microscopy (SEM), ZEISS EVO 40HV (Germany). MXene-epoxy composites and pure epoxy matrix structures were characterised on a gold-coated fractured specimen surface.

2.4.2. X-ray photoelectron spectroscopy

The MAX phase and prepared MXene were characterised by using X-ray photoelectron spectroscopy (XPS). The spectra were recorded by using a Thermo Scientific K-Alpha XPS system (Thermo Fisher Scientific, U.K.) equipped with a micro-focused, monochromatic Al K α X-ray source (1486.68 eV). An X-ray beam with a size of 400 μ m was used at

the settings of 6 mA/12 kV. The spectra were acquired in the constant analyser energy mode with pass energy of 200 eV for the survey. Narrow regions were collected by using the pass energy of 50 eV. Charge compensation was achieved with the use of the system dual-beam flood gun. The Thermo Scientific Avantage software package (version 5.9921, Thermo Fisher Scientific) was used for digital spectrum acquisition and data processing. Spectral calibration was performed by using the automated calibration routine and the internal Au, Ag, and Cu standards supplied with the K-Alpha system. The surface compositions in atomic percentage (at%) were determined by considering the integrated peak areas of the detected atoms and the respective sensitivity factors. The fractional concentration of a particular element *A* was computed using the following equation:

$$\%A = \frac{I_A/s_A}{\sum (I_n/s_n)} 100\%, \quad (1)$$

where I_n and s_n denote the integrated peak areas and the Scofield sensitivity factors corrected for the analyser transmission, respectively.

2.4.3. Atomic force microscopy imaging

The surface topographies of the MXene-coated glass samples were observed by means of an atomic force microscope (AFM) NanoWizard®3 NanoScience, JPK Instruments AG (Germany). The AFM data were processed by means of the original JPK instruments AG JPKSPM Data Processing software (Microtestmachines Co., Belorussia). An ULTRASHARP Si cantilever with a curvature radius of <10 nm was used (Spring Constant 37 N/m) for the AFM measurements. The measurements were performed in the contact mode with a maximum scan field of 10 × 10 μ m.

2.4.4. Surface energy calculation

The surface energy of solids is influenced by multiple interfacial processes such as adhesion, adsorption, and wetting. The harmonic mean approach (HMA) is frequently used to calculate the various surface

energy components of solids to predict the adhesion properties. In this regard, Fowkes proposed that surface energy γ_s can be considered as the sum of the contributions of the dispersion (γ_s^d) and polar (γ_s^p) components [34]:

$$\gamma_s = \gamma_s^d + \gamma_s^p \quad (2)$$

Here, the superscript d refers to the dispersion force (London-type) and p the hydrogen bonding. Parameters γ_s^d and γ_s^p were determined from the contact angles of each of the liquid pairs considered by means of Wu's HMA approximation for each liquid [35]:

$$(1 + \cos \theta_i) \gamma_i = 4 \frac{\gamma_i^d \gamma_i^d}{\gamma_i^d + \gamma_i^d} + 4 \frac{\gamma_i^p \gamma_i^p}{\gamma_i^d + \gamma_i^p} \quad (3)$$

where subscripts i and s denote the probe liquid and solid, respectively.

Meanwhile, Owens and Wendt [1969] proposed the following geometric mean approach (GMA) [36] to relate the surface energy and contact angle values:

$$(1 + \cos \theta_i) \gamma_i = 2 \left(\sqrt{\gamma_i^d \gamma_s^d} + \sqrt{\gamma_i^p \gamma_s^p} \right) \quad (4)$$

The interfacial energy γ_{s1s2} between two components s_1 and s_2 is calculated according to Ref. [35].

$$\gamma_{s1s2} = \gamma_{s1} + \gamma_{s2} - 4 \frac{\gamma_{s1}^d \gamma_{s2}^d}{\gamma_{s1}^d + \gamma_{s2}^d} - 4 \frac{\gamma_{s1}^p \gamma_{s2}^p}{\gamma_{s1}^p + \gamma_{s2}^p} \quad (5)$$

where γ_{s1} and γ_{s2} denote the surface energies, γ_{s1}^d and γ_{s2}^d the dispersive components, and γ_{s1}^p and γ_{s2}^p the polar surface-energy components of s_1 and s_2 , respectively.

The interaction occurring at the phase boundary of the MXene particles and epoxy was also evaluated by using the work of adhesion parameter W_{s1s2} as per Dupré [37]:

$$W_{s1s2} = \gamma_{s1} + \gamma_{s2} - \gamma_{s1s2} \quad (6)$$

where component s_1 refers to epoxy and s_2 to MXene.

2.4.5. Contact-angle measurements

For contact-angle measurements, 2-ml liquid droplets were placed on the MXene-coated glass samples, and the average contact angle (θ) was measured by using a surface energy evaluation system (Advex Instruments) and See-System software. A sequence of images was recorded over 60 s starting from the moment of droplet deposition, which facilitated the monitoring of the contact-angle dynamics over time. Diiodomethane, deionised water, and glycerol were chosen for the investigation of the surface energy; the principal surface-energy parameters of these liquids are listed in Table 1. For each test, the average contact-angle values of three drops were considered.

Table 4

Contact angles (degrees) of polar and non-polar liquids on epoxy and 1 wt% MXene-epoxy films.

Material	Water	Diiodomethane	Glycerol
Epoxy	62.00 ± 1.2	28.85 ± 1.1	82.59 ± 1.0
1 wt% MXene-epoxy	62.11 ± 0.9	25.50 ± 0.7	76.54 ± 1.9

3. Results and discussion

3.1. Characterisation of MXene

MXenes are usually prepared from MAX phases with the selective etching of the 'A' layers by the application of various procedures [9, 39–41]. In this study, the etching of the Ti_3AlC_2 MAX phase was performed by using a combination of HCl and LiF. The morphology of the MAX phase used for MXene preparation is shown in Fig. 1a, and the partially delaminated MXene nanoparticles after the etching are shown in Fig. 1b.

Here, it is noted that each specific preparation condition can influence the quality of the prepared MXene. Therefore, the XPS method is used to characterise the initial MAX phase and MXene surface chemical composition (Table 2). The surface of the MAX phase is strongly oxidised, and the spectrum demonstrates the presence of a Ti2p signal at ~458.8 eV corresponding to TiO_2 and an Al2p signal at ~74.3 eV corresponding to AlO_x (10.5 at% of AlO_x versus 2.3 at% of Al metal centred at ~72.0 eV, not listed in Table 2), which is most probably due to Al_2O_3 . There is also some contamination by nitrogen and sulphur (SO_3 centred at ~167.0 eV). After etching and MXene preparation, the contamination by nitrogen decreases to 1.3 at%, and sulphur completely disappears. The XPS results confirm the successful etching of Al from the MAX phase structure, and the results are also consistent with a previously obtained XPS analysis by Halim et al. [42].

Table 2 summarises the apparent surface chemical compositions of the initial MAX phase and final MXene samples, calculated from the deconvolution of individual high-resolution spectra. For MXene, a typical carbide signal is detected at ~281.6 eV (Fig. 2a). The signal at ~283 eV (labelled as 'carbide II') may be due to some satellite of the Ti carbide, possibly caused by conductive electrons available for shake-up-like events following core electron photoemission. Additionally, this position may also correspond to substoichiometric TiC_x or C–Ti–O due to the adsorption of the OH group on the MXene surface. The presence of the C–Ti–O group is also indicated by the O1s signal centred at ~531.5 eV (not shown in Fig. 2); however, this signal overlaps with the C=O organic contamination signal (labelled in Table 2 as 'O1s I'). Signals from adventitious carbon due to sample manipulation are centred at ~285.0 eV (sp^3 carbon), ~286.2 eV (C–O groups), and ~288.9 eV (O–C=O groups). The signal at ~288.9 eV can overlap with the C–F bonding signal. The signal at ~284 eV (labelled as ' sp^{2*} ') can be attributed to Ti–oxycarbides (Ti–OC) or some graphitic carbon.

Fig. 2b presents the XPS of the Ti2p region whereas Fig. 2c shows

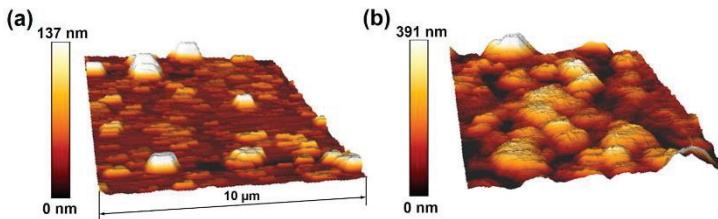


Fig. 4. AFM images of (a) monolayer MXene coating and (b) 10-layer MXene coating on a glass surface.

Table 5Components of surface energy (mJ/m²) determined by HMA and GMA for different numbers of MXene coating layers.

Liquid pairs	MXene coating layers	HMA				GMA			
		γ_s	γ_s^d	γ_s^p	γ_s^d/γ_s	γ_s	γ_s^d	γ_s^p	γ_s^d/γ_s
water–diiodomethane	1	52.00	37.88	14.13	0.27	44.81	35.25	9.56	0.21
	5	55.70	41.25	14.53	0.26	48.33	38.91	9.43	0.19
	10	64.48	41.16	23.32	0.36	56.71	36.01	20.69	0.36
glycerol–diiodomethane	1	44.20	38.27	5.93	0.13	41.33	37.44	3.89	0.09
	5	47.80	41.66	6.15	0.13	45.07	41.13	3.94	0.09
	10	51.13	41.45	9.69	0.19	47.98	39.15	8.83	0.18

Table 6Components of surface energy (mJ/m²) determined by HMA and GMA for epoxy and 1 wt% MXene–epoxy films.

Material	Liquids pairs	HMA				GMA			
		γ_s	γ_s^d	γ_s^p	γ_s^d/γ_s	γ_s	γ_s^d	γ_s^p	γ_s^d/γ_s
Epoxy	water–diiodomethane	59.5	36.6	22.8	0.38	55.5	34.5	20.6	0.37
	glycerol–diiodomethane	46.9	36.9	9.9	0.21	44.4	36.3	8.0	0.18
MXene–epoxy	water–diiodomethane	70.1	33.2	36.9	0.53	68.8	29.0	39.7	0.58
	glycerol–diiodomethane	51.6	33.3	18.3	0.35	50.5	30.9	19.6	0.39

Table 7

Interfacial tension and work of adhesion between MXene–epoxy interface.

Method	Liquids pairs	Interfacial tension, γ_{s1s2} , mJ/m ²	Work of adhesion, W_{s1s2} , mJ/m ²
HMA	water–diiodomethane	0.37	123.6
	glycerol–diiodomethane	0.36	97.66
GMA	water–diiodomethane	0.44	111.78
	glycerol–diiodomethane	0.24	92.14

that of the F1s region of the MXenes. In addition to TiO₂ and Ti₃C₂, Ti2p also shows an increase in the signal at ~456.1 eV (labelled as 'Ti I') and at ~457.2 eV (labelled as 'Ti II'). These signals along with some oxidation signals (C–Ti–O_x and some suboxides TiO_x) may be also correlated to the binding with fluorine, which is readily embedded in the final MXene structure. The F1s spectrum (Fig. 2c) exhibits a strong signal at ~685 eV, which can correspond to fluorine binding to the Ti carbide, thereby creating a C–Ti–F_x bond. The F1s signal at the slightly higher binding energy of ~686.5 eV can be attributed to C–Ti–OF_x or even a fluorine bridging atom (C–Ti–F–Ti–C) [43]. The signal at ~684 eV is probably due to traces of used HF or some other fluoride.

The MXene stoichiometry can be calculated from the obtained XPS results after subtracting the signals related to carbon contamination (signals of C1s beyond 284 eV) and TiO₂ signals (Ti2p at ~458.8 eV related to the O1s signal at ~529.6 eV). The final stoichiometry of MXene was determined to be Ti₃C_{1.84}O_{2.12}F_{2.39}.

3.2. Characterisation of surface energy of MXene and its interfacial adhesion energy with epoxy

The water and glycerol contact-angle measurements on mono-, five-, and ten-layer MXene coatings on glass substrates are shown in Fig. 3. The contact angles for both liquids are not constant owing to factors such as hydrophilicity, microporosity, and roughness, which increase with higher number of coating layers. The results indicate that the contact angle tends to decrease by 1–2° for water and 7–9° for glycerol over the first 10 s. The glycerol droplets reach an equilibrium after 15 s, which indicates steady-state contact angle values, that were used for further surface energy estimation.

Steady-state contact angle values of water, diiodomethane, and glycerol are listed in Table 3. The MXene monolayer coating exhibits a water contact angle of 68.4°, while the 10-layer sample exhibits a value of 48.5°. Furthermore, the 10-layer MXene shows a high wettability of just 29.95° for the non-polar diiodomethane solvent. These results

confirm that MXenes exhibit hydrophilic characteristics owing to their layered structure and surface functional groups such as hydroxyl, oxide, or fluorine groups (as indicated by the XPS analysis). The results further suggest the promising adhesion properties of MXene with a polymer matrix.

The surface topography of the MXene coating on the glass substrates was estimated by means of AFM imaging (Fig. 4). As can be observed from the AFM image in Fig. 4a, the monolayer MXene coating surface exhibits the sharp peaks and valleys of roughness profile (Kurtosis $R_{ku} = 3.18$) with an average roughness of 11.98 nm and maximum profile peak height $R_p = 137$ nm (Fig. 4a). On the other hand, the five and 10-layer coating surfaces show rounded peaks and grooves on the surface profile ($R_{ku} < 3$) [44]. The average surface roughness for the 5-layer coating increases to 37.88 nm and R_p up to 257.9 nm, and the average surface roughness and R_p for the 10-layer coating are 84.93 nm and 391 nm, respectively (Fig. 4b).

Topography and contact angle measurements show that the MXene multilayers exhibit improved wettability properties owing to the increased roughness and surface area of the exposed hydrophilic nanoparticles [44].

The surface energies of the epoxy and MXene–epoxy composite were calculated with polar (water and glycerol) and non-polar (diiodomethane) liquids (Table 4). The contact angles of water show similar results for both materials, while those of diiodomethane and glycerol exhibit a slight decrease of 3–4° between the two materials.

Surface energies γ_s and their dispersion (γ_s^d) and polar components (γ_s^p) for MXene, epoxy resin, and MXene–epoxy composites were calculated from the contact angles following Eqs. (2–4). The averaged results in Table 5 indicate that regardless of the liquid pairs selected, the calculated surface energy values correlate well between HMA and GMA. In addition, the magnitude distribution of the energy values of the specimens calculated by using these equations remains the same (as described above); the minimum γ_s values are obtained for the monolayer coating and the maximum values for the 10-layer coating. Both the HMA and GMA afford similar trends.

MXene is expected to demonstrate improved adhesive properties at the filler–matrix interface when compared with that of graphene. According to the results, MXene exhibits high surface energy up to 64.48 mJ/m² and forms strong adhesive bonds with polymers. For comparison, it is noted that the surface energy of graphene is 46.7 mJ/m² and that of graphene oxide is 62.1 mJ/m² [45,46].

The surface energy range of the epoxy resin was estimated to be 44.4–59.5 mJ/m² (Table 6), which is typical for commercially available epoxy resins. A prerequisite for good adhesion between a filler and

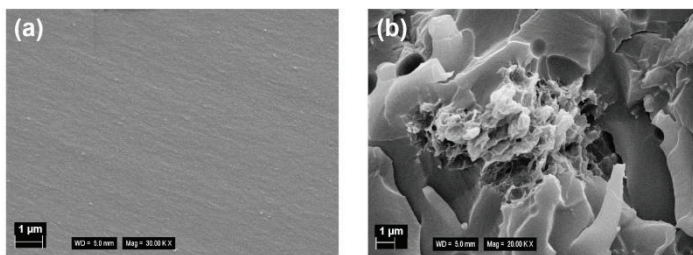


Fig. 5. SEM images of fractured cross-sectional surfaces of (a) pure epoxy specimen, (b) 1 wt% MXene-epoxy specimen.

polymer is that the filler surface energy must be greater or equal to that of the polymer.

The polar component of the surface energy, γ_s^p , is smaller than that of the dispersive component γ_s^d , particularly when the glycerol-diiodomethane liquid pair is used. The γ_s^p/γ_s ratio is 2–2.5 times lower for MXene and 1.8–2 times lower for the epoxy, depending on liquid pair used. The more significant difference could be due to the higher glycerol viscosity. However, as can be observed from Table 5 and Table 6, the γ_s^p/γ_s ratio between the dispersive and polar components of the surface energy for MXene (0.19 and 0.21) and epoxy (0.36 and 0.38) is very close. It is known that the closer is the γ_s^p/γ_s ratio between the MXene and the epoxy (using the same liquid pair), the stronger are the interactions between the phases, and the higher is the expected adhesion. The surface energy of MXene-epoxy composites is very similar to that of MXene and is about 10–20% higher than that of epoxy. The MXene particles increase the surface energy of the epoxy resin, mainly due to the polar component of the surface tension. This contribution also indicates the ability of the surface to participate in H-bonding interactions.

For the evaluation of interfacial energy and work of adhesion, it was assumed that the surface tension of the 10-layer MXene coating is equal to the surface tension of the MXene particles. As can be inferred from Table 7, the interfacial energy γ_{s1s2} between MXene and epoxy resin is low (0.24–0.44 mJ/m² as per Eq. (5)). The interaction occurring at the phase boundary of the MXene particles and epoxy was also evaluated by employing the work of adhesion W_{S1S2} (92.14–123.6 mJ/m²), which was calculated using Eq. (6). The obtained work of adhesion values for MXenes and epoxy were relatively high (Table 7). These values are similar or higher than those obtained for glass fibre and epoxy (89–95 mJ/m²) [47].

The possibility of high MXene-epoxy interfacial adhesion was also analysed via the examination of the SEM images of the fractured surface of 1 wt% MXene-epoxy specimens. The SEM images show a smooth fracture surface for the pure epoxy sample (Fig. 5a) and a significantly rougher fracture for 1 wt% MXene-epoxy composite (Fig. 5b). MXenes appear as particles with dimensions ranging from 1 to 5 µm, as can be observed from the cluster in the centre of the image in Fig. 5b. Such fractured surface suggests good adhesion properties between MXene and epoxy matrix.

4. Conclusions

In this study, Ti₃C₂T_x MXenes were prepared by the hydrochloric acid/lithium fluoride etching of Ti₃AlC₂. The characterisation of MXenes, MXene coatings, and MXene-epoxy nanocomposites was carried out with XPS, AFM, and SEM analyses. The wettability properties of MXenes, surface energies, and work of adhesion were estimated by calculating the contact angles of polar and non-polar liquids. The wettability improved with an increase in the number of coating layers for all the considered liquids. This was confirmed by AFM investigations; the smooth hydrophilic surface of monolayer MXene coating exhibited

an average roughness of 11.98 nm, whereas that of the 10-layer coating was 84.93 nm.

The surface energy of the 10-layer MXene coating ranged between 47.98 and 64.48 mJ/m², depending on the probe liquid used. The surface energy of epoxy with 1 wt% of randomly distributed MXenes increased relative to that of the pure MXene coating. According to the work of adhesion values (92.14–123.6 mJ/m²), the interfacial adhesion between the MXene particles and the epoxy is high. The results presented in this article suggest that MXene addition can lead to an improvement in the mechanical properties of MXene-epoxy-fibre composites, MXene-polymer coatings, and polymer-based sensors, which can be utilised for various multifunctional applications.

CRedit authorship contribution statement

K. Zukiene: Conceptualization, Methodology, Validation, Formal analysis, Investigation, Writing - original draft, Writing - review & editing, Visualization. **G. Monastyreckis:** Validation, Formal analysis, Investigation, Writing - original draft, Writing - review & editing, Visualization. **S. Kilikevicius:** Methodology, Formal analysis, Investigation, Writing - review & editing, Visualization. **M. Procházka:** Methodology, Formal analysis, Investigation, Writing - review & editing, Visualization. **M. Micusik:** Methodology, Formal analysis, Investigation, Writing - review & editing, Visualization. **M. Omastová:** Conceptualization, Methodology, Validation, Formal analysis, Investigation, Resources, Writing - original draft, Writing - review & editing, Supervision, Project administration, Funding acquisition. **A. Aniskevich:** Conceptualization, Formal analysis, Investigation, Resources, Writing - review & editing, Supervision, Project administration, Funding acquisition. **D. Zeleniakienė:** Conceptualization, Methodology, Validation, Formal analysis, Investigation, Resources, Writing - original draft, Writing - review & editing, Supervision, Project administration, Funding acquisition.

Declaration of competing interest

The authors declare that they have no known competing financial interests or personal relationships that could have appeared to influence the work reported in this paper.

Acknowledgements

This work was developed under the M-era.Net research project titled NANO2COM-Advanced Polymer Composites Filled with Novel 2D Nanoparticles. The research was funded by grants No. S-M-ERA.NET-18-1 from the Research Council of Lithuania, No. 1.1.1.5/ERANET/18/02 from Latvian State Education Development Agency, and No. M-ERA-NET-18-414-Nano2Com from the Slovak Academy of Sciences.

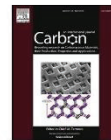
References

- [1] Y. Chen, Z. Fan, Z. Zhang, W. Niu, C. Li, N. Yang, B. Chen, H. Zhang, Two-dimensional metal Nanomaterials: synthesis, properties, and applications, *Chem. Rev.* 118 (2018) 6409–6455, <https://doi.org/10.1021/acs.chemrev.7b00727>.
- [2] C. Tan, X. Cao, X. Wu, Q. He, J. Yang, X. Zhang, J. Chen, W. Zhao, S. Han, G. Nam, M. Sindoro, H. Zhang, Recent advances in ultrathin two-dimensional nanomaterials, *Chem. Rev.* 117 (2017) 6225–6331, <https://doi.org/10.1021/acs.chemrev.6b00558>.
- [3] H. Jin, C. Guo, X. Liu, J. Liu, A. Vasile, Y. Jiao, Y. Zheng, S. Qiao, Emerging two-dimensional nanomaterials for electrocatalysis, *Chem. Rev.* 118 (2018) 6337–6408, <https://doi.org/10.1021/acs.chemrev.7b00689>.
- [4] M. Naguib, M. Kurtoglu, V. Presser, J. Liu, J. Niu, M. Heon, L. Hultman, Y. Gogotsi, M.W. Barsoum, Two-dimensional nanocrystals produced by exfoliation of Ti_3AlC_2 , *Adv. Mater.* 23 (2011) 4248–4253, <https://doi.org/10.1002/adma.201102346>.
- [5] Y. Gogotsi, B. Anasori, The rise of MXenes, *ACS Nano* 13 (2019) 8491–8494, <https://doi.org/10.1021/acsnano.9b06394>.
- [6] M.Q. Zhao, C.E. Ren, Z. Ling, M.R. Lukatskaya, C. Zhang, K.L. Van Aken, M. W. Barsoum, Y. Gogotsi, Flexible MXene/carbon nanotube composite paper with high volumetric capacitance, *Adv. Mater.* 27 (2015) 339–345, <https://doi.org/10.1002/adma.201404140>.
- [7] F. Shalazad, M. Allahbakhsh, C.B. Hatter, B. Anasori, S.M. Hong, C.M. Koo, Y. Gogotsi, Electromagnetic interference shielding with 2D transition metal carbides (MXenes), *Science* 353 (80) (2016) 1137–1140, <https://doi.org/10.1126/science.12421>.
- [8] C.J. Zhang, B. Anasori, A. Serral-ascaso, S. Park, N. Mcevoy, A. Shmeliov, G. S. Duesberg, J.N. Coleman, Y. Gogotsi, V. Nicolosi, Transparent, flexible, and conductive 2D titanium carbide (MXene) films with high volumetric capacitance, *Adv. Mater.* 29 (2017) 1702678, <https://doi.org/10.1002/adma.201702678>.
- [9] A. Lipatov, H. Lu, M. Allahbakhsh, B. Anasori, A. Gruverman, Y. Gogotsi, A. Smit'skii, Elastic properties of 2D $\text{Ti}_3\text{C}_2\text{Tx}$ MXene monolayers and bilayers, *Sci. Adv.* 4 (2018), <https://doi.org/10.1126/sciadv.aan0491>, eaa0491.
- [10] G. Plummer, B. Anasori, Y. Gogotsi, G.J. Tucker, Nanoindentation of monolayer $\text{Ti}_3\text{C}_2\text{Tx}$ MXenes via atomistic simulations: the role of composition and defects on strength, *Comput. Mater. Sci.* 157 (2019) 168–174, <https://doi.org/10.1016/j.compscitech.2018.10.033>.
- [11] D. Zeleniakienė, G. Monastyreckis, A. Aniskevich, P. Griskevicius, Deformation and failure of MXene nanosheets, *Materials* 13 (2020) 1253, <https://doi.org/10.3390/ma13051253>.
- [12] L. Gao, C. Li, W. Huang, S. Mei, H. Liu, Q. Ou, Y. Zhang, J. Guo, F. Zhang, S. Xu, H. Zhang, MXene/polymer Membranes: synthesis, properties, and emerging applications, *Chem. Mater.* 32 (2020) 1703–1747, <https://doi.org/10.1021/acs.chemmater.9b04408>.
- [13] J. Jimmy, B. Kandasubramanian, MXene functionalized polymer composites: synthesis and applications, *Eur. Polym. J.* 122 (2020) 109367, <https://doi.org/10.1016/j.eurpolymj.2019.109367>.
- [14] S.M. George, B. Kandasubramanian, Advancements in MXene-Polymer composites for various biomedical applications, *Ceram. Int.* 46 (2020) 8522–8535, <https://doi.org/10.1016/j.ceramint.2019.12.257>.
- [15] W. Yang, J. Liu, L. Wang, W. Wang, A. Chun, Y. Yuen, S. Peng, B. Yu, H. Lu, G. Heng, C. Wang, Multifunctional MXene/natural rubber composite films with exceptional flexibility and durability, *Compos. Part B* 188 (2020) 107875, <https://doi.org/10.1016/j.compositesb.2020.107875>.
- [16] T. Yun, H. Kim, A. Iqbal, Y.S. Cho, G.S. Lee, M. Kim, S.J. Kim, D. Kim, Y. Gogotsi, S. O. Kim, C.M. Koo, Electromagnetic shielding of monolayer MXene assemblies, *Adv. Mater.* 32 (2020) 1906769, <https://doi.org/10.1002/adma.201906769>.
- [17] Y. Yang, Z. Cao, P. He, L. Shi, G. Ding, R. Wang, $\text{Ti}_3\text{C}_2\text{Tx}$ MXene graphene composite films for wearable strain sensors featured with high sensitivity and large range of linear response, *Nano Energy* 66 (2019) 104134, <https://doi.org/10.1016/j.nanoen.2019.104134>.
- [18] S. Seyedin, S. Uzun, A. Levitt, B. Anasori, G. Dion, Y. Gogotsi, J.M. Razal, MXene composite and coaxial fibers with high stretchability and conductivity for wearable strain sensing textiles, *Adv. Funct. Mater.* 30 (2020) 1910504, <https://doi.org/10.1002/adfm.201910504>.
- [19] C. Prasad, X. Yang, Q. Liu, H. Tang, A. Ramnathan, S. Zul, G. V. Zyryanov, S. Shah, Journal of Industrial and Engineering Chemistry Recent advances in MXenes supported semiconductor based photocatalysts: properties, synthesis and photocatalytic applications, *J. Ind. Eng. Chem.* 85 (2020) 1–33, <https://doi.org/10.1016/j.jiec.2019.12.003>.
- [20] Z. Fu, N. Wang, D. Legut, C. Si, Q. Zhang, S. Du, T.C. Germann, J.S. Francisco, R. Zhang, Rational design of flexible two-dimensional MXenes with multiple functionalities, *Chem. Rev.* 119 (2019) 11980–12031, <https://doi.org/10.1021/acs.chemrev.9b00348>.
- [21] S.J. Kim, H.J. Koh, C.E. Ren, O. Kwon, K. Maleski, S. Cho, B. Anasori, C. Kim, Y. Choi, J. Kim, Y. Gogotsi, Metallic $\text{Ti}_3\text{C}_2\text{Tx}$ MXene gas sensors with ultrahigh signal-to-noise ratio, *ACS Nano* 12 (2018) 986–993, <https://doi.org/10.1021/acsnano.7b07460>.
- [22] Z. Wang, K. Yu, Y. Feng, R. Qi, J. Ren, Z. Zhu, Stabilizing $\text{Ti}_3\text{C}_2\text{Tx}$ -MXenes with TiO_2 nanospheres intercalation to improve hydrogen evolution reaction and humidity-sensing performance, *Appl. Surf. Sci.* 496 (2019) 143729, <https://doi.org/10.1016/j.apsusc.2019.143729>.
- [23] Z. Ling, C.E. Ren, M.-Q. Zhao, J. Yang, J.M. Giannunzio, J. Qiu, M.W. Barsoum, Y. Gogotsi, flexible and conductive MXene films and nanocomposites with high capacitance, *Proc. Natl. Acad. Sci.* 111 (2014) 16676–16681, <https://doi.org/10.1073/pnas.1414215111>.
- [24] X. Zhang, J. Xu, H. Wang, J. Zhang, H. Yan, B. Pan, Ultrathin nanosheets of MAX phases with enhanced thermal and mechanical properties in polymeric composites: $\text{Ti}_3\text{Al}_2\text{Al}_0.2\text{C}_2$, *Angew. Chem. Int. Ed.* (2013) 4361–4365, <https://doi.org/10.1002/anie.201300285>.
- [25] Y. Zou, L. Fang, T. Chen, M. Sun, C. Lu, Z. Xu, Near-infrared light and solar light activated self-healing epoxy coating having enhanced properties using MXene flakes as multifunctional fillers, *Polymers* 10 (2018), <https://doi.org/10.3390/polym10050474>.
- [26] R. Kang, Z. Zhang, L. Guo, J. Cui, Y. Chen, X. Hou, Enhanced thermal conductivity of epoxy composites filled with 2D transition metal carbides (MXenes) with ultralow loading, *Sci. Rep.* 9 (2019) 9135, <https://doi.org/10.1038/s41598-019-45664-4>.
- [27] L. Wang, L. Chen, P. Song, C. Liang, Y. Lu, H. Qiu, Y. Zhang, J. Kong, Fabrication of the annealed $\text{Ti}_3\text{C}_2\text{Tx}$ MXene/Epoxy nanocomposites for electromagnetic interference shielding application, *Compos. Part B* 171 (2019) 111–118, <https://doi.org/10.1016/j.compositesb.2019.04.050>.
- [28] G. Monastyreckis, L. Mishnaevsky Jr., C.B. Hatter, A. Aniskevich, Y. Gogotsi, D. Zeleniakienė, Micromechanical modeling of MXene-polymer composites, *Carbon* 162 (2020) 402–409, <https://doi.org/10.1016/j.carbon.2020.02.070>.
- [29] S. Kilikevicius, S. Kvietkaite, K. Zukiene, M. Omastova, A. Aniskevich, D. Zeleniakienė, Numerical investigation of the mechanical properties of a novel hybrid polymer composite reinforced with graphene and MXene nanosheets, *Comput. Mater. Sci.* 174 (2020) 109497, <https://doi.org/10.1016/j.commatsci.2019.109497>.
- [30] M. Chidi, M.R. Lukatskaya, M. Zhao, Y. Gogotsi, M.W. Barsoum, Conductive two-dimensional titanium carbide 'clay' with high volumetric capacitance, *Nature* 516 (2014) 78–81, <https://doi.org/10.1038/nature13970>.
- [31] K.M. Kang, D.W. Kim, C.E. Ren, K.M. Cho, S.J. Kim, J.H. Choi, Y.T. Nam, Y. Gogotsi, H. Jung, Selective molecular separation on $\text{Ti}_3\text{C}_2\text{Tx}$ -Graphene oxide membranes during pressure driven filtration: comparison with graphene oxide and MXenes, *ACS Appl. Mater. Interfaces* 9 (2017) 46687–46694, <https://doi.org/10.1021/acsmaterials.7b02847>.
- [32] M. Allahbakhsh, K. Maleski, B. Anasori, P. Lelyukh, L. Clark, S. Sin, Y. Gogotsi, Guidelines for synthesis and processing of two dimensional titanium carbide ($\text{Ti}_3\text{C}_2\text{Tx}$ MXene), *Chem. Mater.* 29 (2017) 7633–7644, <https://doi.org/10.1021/acs.chemmater.7b02847>.
- [33] V. Gajdosova, L. Lorencova, M. Prochazka, M. Micusik, M. Omastova, S. Prochazkova, F. Kveton, M. Jerigova, D. Velic, P. Kasak, J. Tkac, Remarkable differences in the voltaic response towards hydrogen peroxide, oxygen and $\text{Ru}(\text{NH}_3)_6^{3+}$ of electrode interfaces modified with HF or LiF-HCl etched $\text{Ti}_3\text{C}_2\text{Tx}$ MXene, *Microchimica Acta* 187 (52) (2020), <https://doi.org/10.1007/s00604-019-4049-6>.
- [34] P.M. Fowkes, Additivity of intermolecular forces at interfaces. I. Determination of the contribution to surface and interfacial tensions of dispersion forces in various liquids, *J. Phys. Chem.* 67 (1963) 2538–2541, <https://doi.org/10.1021/j100806a008>.
- [35] S. Wu, Calculation of interfacial tension in polymer systems, *J. Polym. Sci. Part C Polym. Symp.* 34 (1971) 19–30, <https://doi.org/10.1002/pole.5070340105>.
- [36] D.K. Owens, R.C. Wendt, Estimation of the surface free energy of polymers, *J. Appl. Polym. Sci.* 13 (1969) 1741–1747, <https://doi.org/10.1002/app.1969.070130815>.
- [37] A. Dupre, P. Dupre, *Théorie mécanique de la chaleur*, Gauthier Villars, Paris, 1869.
- [38] D. Feldman, in: D.W. van Krevelen (Ed.), *Properties of Polymers*, third ed., Elsevier Science, New York, 1990, p. 875, <https://doi.org/10.1002/polb.1991.090291313>.
- [39] M. Naguib, O. Mashtalir, J. Carle, V. Presser, J. Lu, L. Hultman, Y. Gogotsi, M. W. Barsoum, Two dimensional transition metal carbides, *ACS Nano* 6 (2012) 1322–1331, <https://doi.org/10.1021/nl204153h>.
- [40] M. Naguib, Y. Gogotsi, Synthesis of two-dimensional materials by selective extraction, *Acc. Chem. Res.* 48 (2015) 128–135, <https://doi.org/10.1021/ar500346b>.
- [41] F. Liu, A. Zhou, J. Chen, J. Jia, W. Zhou, L. Wang, Q. Hu, Preparation of Ti_3C_2 and Ti_3C_2 MXenes by fluoride salts etching and methane adsorptive properties, *Appl. Surf. Sci.* 416 (2017) 781–789, <https://doi.org/10.1016/j.apsusc.2017.04.239>.
- [42] J. Hailin, K.M. Cooc, M. Naguib, P. Eklund, Y. Gogotsi, J. Rosen, M.W. Barsoum, Applied Surface Science X-ray photoelectron spectroscopy of select multi layered transition metal carbides (MXenes), *Appl. Surf. Sci.* 362 (2016) 406–417, <https://doi.org/10.1016/j.apsusc.2015.11.089>.
- [43] M. Boca, P. Barborik, M. Micusik, M. Omastova, X ray photoelectron spectroscopy as detection tool for coordinated or uncoordinated fluorine atoms demonstrated on f luoride systems NaF , K_2TaF_7 , K_3TaF_6 , K_2ZrF_6 , $\text{Na}_2\text{Zr}_2\text{F}_{11}$ and K_2ZrF_6 , *Solid State Sci.* 14 (2012) 828–832, <https://doi.org/10.1016/j.solidstatesciences.2012.04.018>.
- [44] J. Mikuliczyn, R. Starosta, The study of linear correlation between surface roughness parameters and adhesion of flame sprayed coatings, *Journal of KONES Powertrain and Transport* 23 (2016) 223–229, <https://doi.org/10.5604/12314005.1213573>.
- [45] Y.J. Shin, Y. Wang, H. Huang, G. Kalon, A. Thye, S. Wee, Z. Shen, C.S. Bhatia, H. Yang, Surface-energy engineering of graphene, *Langmuir* 26 (2010) 3798–3802, <https://doi.org/10.1021/la100231u>.
- [46] S. Wang, Y. Zhang, N. Abidi, L. Cabralles, Wettability and surface free energy of graphene films, *Langmuir* 25 (2009) 11078–11081, <https://doi.org/10.1021/la901402z>.
- [47] J.G. Swadener, K.M. Liechti, A.L. Lozano, The intrinsic toughness and adhesion mechanisms of a glass/epoxy interface, *J. Mech. Phys. Solids*. 47 (1999) 112–147.



Contents lists available at ScienceDirect

Carbon

journal homepage: www.elsevier.com/locate/carbon

Micromechanical modeling of MXene-polymer composites

G. Monastyreckis^{a,*}, L. Mishnaevsky Jr.^b, C.B. Hatter^c, A. Aniskevich^d, Y. Gogotsi^c,
D. Zeleniakiene^a

^a Department of Mechanical Engineering, Kaunas University of Technology, Studentų st. 56, 51424, Kaunas, Lithuania

^b Department of Wind Energy, Technical University of Denmark, 2000, Roskilde, Denmark

^c Department of Materials Science and Engineering and A. J. Drexel Nanomaterials Institute, Drexel University, 3141 Chestnut St, Philadelphia, PA, 19104, USA

^d Institute for Mechanics of Materials, University of Latvia, 23 Aizkraukles st, LV-1006, Riga, Latvia



ARTICLE INFO

Article history:

Received 24 January 2020

Received in revised form

11 February 2020

Accepted 23 February 2020

Available online 24 February 2020

ABSTRACT

Polymer composites are considered among the most promising materials for functional and structural applications. Improvement of mechanical properties of polymer composites using nanomaterials has generated much interest in recent years. This study aimed to predict the tensile strength and determine the damage mechanism of MXene-polyvinyl alcohol and MXene-epoxy composites. All parameters such as particle size, mechanical properties and interface layer strength were calibrated by finite element modeling with respect to experimental results. The influence of aspect ratio, volume fraction and MXene flake alignment on final mechanical properties of representative volume element models were investigated. Simulation results showed that aligned and higher aspect ratio particles significantly increase Young's modulus and tensile strength of the composite. Compared with neat epoxy, a model with 30 vol% aligned MXene flakes resulted in increased Young's modulus of 743% and tensile strength of 91.4%.

© 2020 Elsevier Ltd. All rights reserved.

1. Introduction

Polymers have gained much attention in recent years due to their easy processability, low weight, flexibility and low cost. However, the addition of nanomaterial fillers offers a wide range of new tunable properties resulting in new multi-functional composite materials for various uses in aerospace, energy storage, and electromagnetic interference shielding [1–3]. MXenes, a large family of two-dimensional (2D) materials discovered in 2011, have gained much attention due to their unique properties, such as high metallic conductivity and excellent mechanical properties coupled with hydrophilicity due to surface terminations present after etching [4,5]. These properties make MXenes ideal candidates for designing new multi-functional polymer composites.

Titanium carbide ($\text{Ti}_3\text{C}_2\text{T}_x$), the most commonly studied MXene to date, has been investigated in several different polymer systems [2,6,7]. Ti_3AlC_2 MAX phase precursor [8] is selectively etched to remove Al, resulting in a multi-layer MXene structure followed by delamination processes to obtain single flakes [9]. As a result, the

MXene surface is covered with functional groups (T_x) like -O, -OH, and -F creating hydrophilic properties and making MXenes easily dispersible in various polar solvents [10,11]. High aspect ratio (AR) nanomaterials, such as graphene, have been shown to increase fatigue resistance within polymer nanocomposites by limiting micro-crack growth and propagation [12,13]. However, due to lack of surface functional groups on the graphene surface, incorporation into polymer systems becomes more difficult. High AR $\text{Ti}_3\text{C}_2\text{T}_x$ MXene flakes have been synthesized using different delamination methods [14], making them a promising conductive and reinforcing additive for polymer nanocomposites, especially if their higher bending rigidity [15] and conductivity [6], compared to graphene, is taken into account.

The shape, length and flake thickness of 2D nanoparticles are the main geometrical parameters when predicting mechanical improvement of a composite material. Fig. 1a illustrates the particle shape of the MAX phase precursor, which varies from an unsymmetrical rectangular to a complex polygon, as can be seen in scanning electron microscope (SEM) images [16]. During the etching process, the area and depth of etched aluminum atoms can be irregular, resulting in interconnected MXene sheets (Fig. 1b) [17–20]. Interconnected layers can fracture during etching and delamination, producing rough surfaces and multi-layered

* Corresponding author.

E-mail address: gediminas.monastyreckis@ktu.edu (G. Monastyreckis).

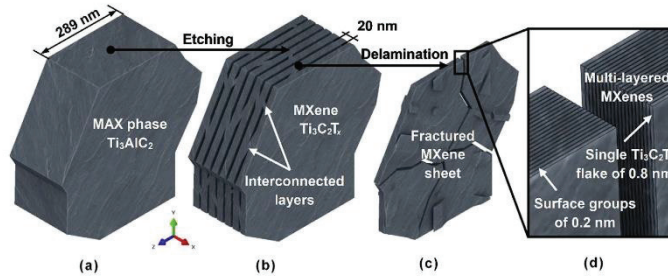


Fig. 1. An illustration of Ti_3AlC_2 MAX phase and corresponding $\text{Ti}_3\text{C}_2\text{T}_x$ MXene: (a) MAX phase – Ti_3AlC_2 ; (b) MXene shape after partial etching with interconnected layers; (c) Multi-layer and fractured $\text{Ti}_3\text{C}_2\text{T}_x$ sheet with a rough surface after delamination; (d) Thickness values of different multi-layered $\text{Ti}_3\text{C}_2\text{T}_x$ structure components. (A colour version of this figure can be viewed online.)

structures of varying thickness containing multiple layers of MXene flakes (Fig. 1c). Further processing using sonication methods can be used to obtain single flakes of different sizes, which are determined by sonication time and intensity [14,21]. Average nanoparticle size can be determined by dynamic light scattering (DLS) method [22]. It was shown that after 1-h treatment, the mean lateral flake size of $\text{Ti}_3\text{C}_2\text{T}_x$ was around 500 nm [21]. The thickness of a single $\text{Ti}_3\text{C}_2\text{T}_x$ flake is approximately 0.8 nm (Fig. 1d). However, the presence of surface functional groups increases that thickness to approximately 1 nm. The thicknesses of multi-layered MXenes can be from 5 to 30 nm producing an AR of approximately 17–100 [18,23–25].

Early modeling using Molecular Dynamics (MD) simulation predicted a single non-terminated Ti_3C_2 flake to have Young's modulus of 502 GPa and tensile strength of 22 GPa [26]. MD nanoindentation simulations of $\text{Ti}_3\text{C}_2\text{T}_x$ monolayer with 1% titanium and 10% carbon atom defects, predicted Young's modulus of 386 GPa [27]. The influence of wrinkles, damaged flakes, multi-layered structure, and atomic defects [28] lead to decreased mechanical properties. In a recent experimental indentation study, $\text{Ti}_3\text{C}_2\text{T}_x$ was shown to have a slightly lower modulus and tensile strength of 330 GPa and 17 GPa, respectively [29].

Multi-scale modeling analysis, including unit cell modeling and homogenization approach, is frequently used to assess mechanical properties of various complex polymer nanocomposites [30–34]. The interaction between nanomaterial fillers and surrounding matrix is usually taken into account as the interface plays a significant role in stress transfer from polymer to nanomaterial, affecting overall mechanical properties. Previous studies using inverse modeling have been used to estimate interfacial properties of nanoparticles such as graphene and clays in nanocomposites [35,36]. Thus far, no modeling studies examining stress-transfer at the $\text{Ti}_3\text{C}_2\text{T}_x$ -polymer interface have been explored.

The aim of this work is to develop a suitable methodology based on finite element (FE) homogenization approach for the prediction of elastic properties and micro-structural damage behavior of novel MXene-polymer composites. Here, inverse modeling methods were used to calculate strength at the interface. The modeling calibration was performed with respect to experimental results of MXene-PVA films with aligned flakes and MXene-epoxy specimens with randomly oriented sheets.

2. Models and methods

2.1. Model development and material properties

Simulations of MXene-polymer composites were performed with ABAQUS CAE software. The geometry of representative volume element (RVE) models was generated by DIGMAT FE code. All models were analyzed under tension conditions with dynamic-explicit methods. The displacement was applied to one side of RVE's mesh nodes and symmetrical boundary conditions were set for the opposite side. Initial stress-strain curve of Ti_3C_2 [26] was inserted into ABAQUS, but it did not have much influence on simulation results, because MXenes were only elastically deformed (Section 2.3). In order to simulate realistic elastic behavior, $\text{Ti}_3\text{C}_2\text{T}_x$ Young's modulus obtained from nanoindentation [29] was used. Experimental stress-strain curves of PVA [6] and epoxy were also inserted in the program. The main mechanical properties of materials are presented in Table 1.

Damage criterion of $\text{Ti}_3\text{C}_2\text{T}_x$ was assumed ductile due to metallic titanium layers and computational modeling results [26], which presented tensile elongation at break of 9.5%. For the simulation of matrix cracking, we used the same maximum principal stress criterion that was previously investigated for polymer matrix with nanoclays [38]. The smallest mesh size for 2D models was set to 0.2 nm, giving an overall number of 200,000–300,000 quadrilateral elements (S4R). For 3D RVE models, the minimum mesh size was set to 5 nm, resulting in a total number of 1–2 million tetrahedral elements (C3D4). Mesh element growth rate for the matrix between the particles was set to 1.5. The crack growth rate was controlled with damage evolution parameter – displacement at failure. Output results of summed reaction forces were obtained from constrained surface nodes of the model mesh.

Initial elastic properties were evaluated using periodic unit cell (PUC) model. In the PUC, we assumed a multi-layer structure with a single MXene flake having a thickness of 0.8 nm and surface functional groups – 0.2 nm (Fig. 2a). The elements of surface functional groups of inner MXene flakes were removed from the model to simulate weak inter-laminar forces between individual MXene flakes. The initial model and particle calibrations with respect to experimental results [6] were performed with PUC. Output results of reaction forces were controlled by the following

Table 1
Mechanical properties of Ti₃C₂T_x, PVA and epoxy.

Material properties	Nanoparticle	Matrices	
	Ti ₃ C ₂ T _x	PVA [6]	epoxy exp.
Young's modulus (GPa)	330 ^a [29]	0.91	0.97
Tensile strength (MPa)	22000 ^b [26]	35	41.9
Tensile elongation at break (%)	9.5 ^b [26]	13.75	11.6
Poisson's ratio	0.23 ^b , accepted as in Ref. [37]	0.4	0.4

^a Measured experimentally.

^b Calculated theoretically.

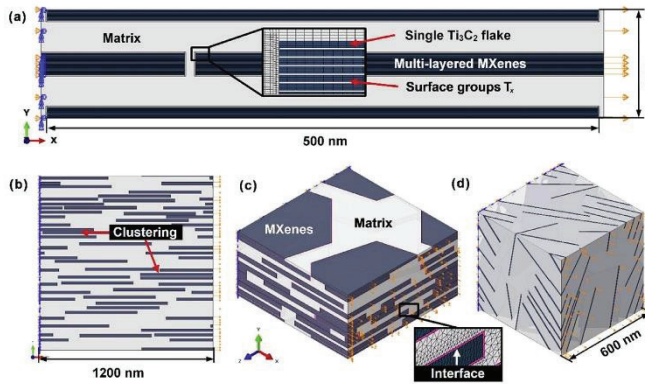


Fig. 2. Examples of FE models with loading and constraints: (a) Periodic unit cell model: 40 vol% aligned multi-layered structure with MXene flakes; (b) 2D RVE model: 40 vol% aligned homogenized MXene sheets; (c) 3D RVE model: 40 vol% aligned hexagonal homogenized MXenes with interface and AR of 25; (d) 3D RVE model: 5 vol% randomly oriented hexagonal homogenized MXenes, AR of 100. (A colour version of this figure can be viewed online.)

geometrical parameters: length of MXene flakes, thickness of multi-layered MXenes, thickness of matrix between parallel MXenes, a gap between longitudinal flakes edges, and length between overlapping flakes.

The calibration of 2D and 3D RVE models (Fig. 2b, c, d) were performed in a similar way: interface layer strength, AR (diameter-to-thickness ratio), and homogenized properties of multi-layered MXenes structure were changed accordingly. The modeling methods of the interface layer and homogenization procedure are explained in Section 2.2 and 2.3, respectively. After the calibration with experimental results, further prediction analysis was performed with various MXene-epoxy models, in order to understand which properties influence tensile results the most (Section 3.4).

2.2. Interface layer modeling

MXene-polymer interface layer was used to evaluate the bonding strength (adhesion) between the filler and the matrix. Preliminary results were done by inverse modeling techniques. Previous studies predicting an interfacial strength of graphene-polymer composites suggested lower values at the filler-matrix interface than polymer itself [36]. For this MXene-polymer study, we followed a similar concept and assumed Young's modulus and interface strength with a factor of 0.25–1, with respect to neat polymer Young's modulus and tensile strength values. FE modelling studies, which analyzed interface properties of single-layer graphene and MXene, used 1 nm thickness for the interface layer [36,39]. MD studies, which analyzed the interfacial region between

PVA and the silica nanospheres assumed the thickness of the interface layer as a single polymer chain size [40] and between poly(2-vinylpyridine) and silica nanofiller the thickness was 4–5 nm [41]. In this article, for multi-layered MXenes we chose an interface layer of 5 nm. Varying the thickness would result in a slightly different tensile result, as the layer occupies only a few percentages of the RVE volume. Eventually, after the calibration, there were no differences in the thickness, because both MXene-PVA and MXene-epoxy interfaces were calculated to have the same properties as the matrix (Section 3.2 and 3.3).

2.3. Homogenization of multi-layered MXenes

The purpose of 2D PUC analysis was to evaluate the stress distribution in a multi-layered MXene structure see the damage behavior of polymer matrix and to arrange homogenization technique for further 3D RVE models. The length of the PUC was set to 672 nm, the length of MXenes – 600 nm and a number of layers – 24. The first cracking appeared at the edges of MXene flakes at the strain of 0.35% (Fig. 3a). Just before the cracking, the stress values of surface flakes reached 542 MPa, while the secondary flakes reached only 48 MPa and the middle one – 29 MPa. After the first cracking, the stress values of inner MXenes dropped to zero and the crack started to grow from the edges of MXenes into PVA matrix (Fig. 3b). At the PUC strain of 1.8%, surface MXenes reached a maximum stress value of 1.8 GPa, while the theoretical strength of a single flake is much higher (Table 1). From this point, the stress values of the PUC started to decrease and eventually PVA matrix fractured.

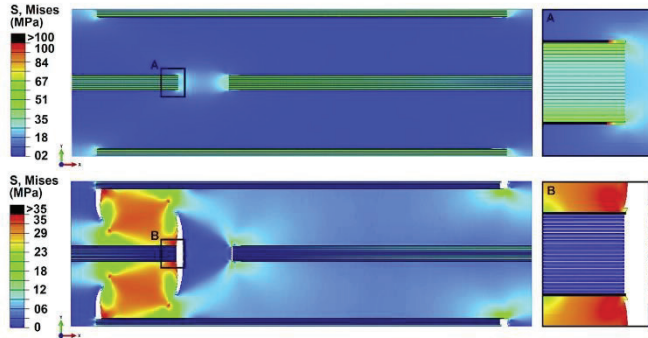


Fig. 3. 2D PUC model in FE simulation – stress distribution and PVA cracking: (a) PUC strain of 0.35%, just before the first matrix cracking – Surface of MXene under 542 MPa stress; (b) PUC strain of 1.8% – zero stress values inside inner MXene flakes and 1.8 GPa stress for surface MXene flakes. (A colour version of this figure can be viewed online.)

In order to extend the calibration and prediction work with much larger 2D and 3D RVE models, the multi-layered structure had to be considered as a single homogenized particle with lowered Young's modulus, respectively to the proportional value of surface flakes thickness (2×0.8 nm) and the multi-layered MXene structure thickness.

3. Results

3.1. Sensitivity analysis of 2D and 3D RVE models

The first task was to check how tensile simulation results might change to imprecise randomly generated RVE models with the same volume fraction of particles. The RVE size was set to 2.4 times larger than particle length. Using the same mechanical properties, loading conditions and mesh sizes, RVE model was repeatedly generated and calculated five times. The scatter of tensile results were the following: Young's modulus – less than 1%, tensile strength and fracture strain – less than 5%.

The second task was to check if the longitudinal shape geometry of the particles could influence tensile results. The cross-sectional SEM images of $\text{Ti}_3\text{C}_2\text{T}_x$ film showed wavy and wrinkled structure of multi-layered MXenes [6]. The films were designed as 2D RVE models with multi-layered MXenes and PVA as a matrix (Fig. 4a, b, c). The length, thickness and homogenized Young's modulus of MXenes were set to 500 nm, 20 nm, and 26.4 MPa, respectively. Tensile results of the simulation are shown in Fig. 4d. The model representing straight multi-layered flakes (2D-RVE-straight) had Young's modulus of 3.15 GPa and tensile strength of 39.8 MPa. The model with 5° inclination of 1.5 sinusoidal waved flakes (2D-RVE-waved) had a modulus of 4.12 GPa and tensile strength of 48.7 MPa, and the model with vertically edged surfaces of 10 nm (2D-RVE-edged) – 4.09 GPa and 47.2 MPa, respectively. The model representing straight morphology MXenes had a significantly higher occurrence of clustering, while wavy and edged type models showed more even distribution of multi-layer flakes throughout the matrix. As a result, elastic and tensile strength properties of wavy and edged models were 30% and 22% higher, respectively.

The tensile simulation of 3D RVE under different tension directions was performed with randomly oriented hexagonal 10 vol% $\text{Ti}_3\text{C}_2\text{T}_x$ -epoxy models. Theoretically, with randomly orientated particles in 3D model, mechanical properties are expected to be

homogeneous in all directions. However, due to imprecise distribution and limited size of RVE, the corresponding stress-strain modeling curves showed tensile strength difference of 9.6% while Young's modulus remained the same (Fig. 4e).

To assess the effect of 3D geometrical shape, the modeling of circular and hexagonal shaped $\text{Ti}_3\text{C}_2\text{T}_x$ was performed. Results of predicted mechanical properties showed no significant differences when altering MXene shape (Fig. 4f). However, the computational time for the model with circular-shaped MXenes was twice as fast when compared to the hexagonal model. Therefore, the circular-shaped MXene model was used for further investigation.

3.2. Interface analysis of MXene-PVA composite

The calibration of MXene-PVA model was done with 2D models first. It was only possible to achieve elastic properties as experimental [6], but not the tensile strength. Therefore, 3D RVE models were developed (Fig. 5a). The calibration of 3D models followed the same procedure as 2D models: the change of AR, homogenized Young's modulus of MXene sheet and interface layer properties.

In order to evaluate the influence of the interface layer on RVE's tensile results, interface layer stress-strain curve was used as an input for software and was obtained by multiplying PVA stress-strain curve with coefficients 0.25; 0.5; 0.75; 1, which gave the strength values of 8.8; 17.5; 26.3; 35 MPa, respectively. The range of tensile results is presented in Fig. 5b. RVE models showed similar results compared to experimental (tensile strength of 86.2 MPa versus 91 MPa) when the interface layer had the same mechanical properties as the matrix (35 MPa). Final simulation parameters of the calibrated model are these: length of MXenes – 600 nm, thickness – 24 nm, homogenized Young's modulus of multi-layered $\text{Ti}_3\text{C}_2\text{T}_x$ – 22 GPa, Young's modulus of the interface layer – 0.91 GPa, interface layer strength – 35 MPa, damage evolution parameter of PVA and interphase – 4 nm displacement at failure.

3.3. Model calibration of MXene-epoxy composite

The purpose of this analysis was to calibrate the FE model with randomly oriented particles to preliminary tensile experiments. To properly distribute 10 wt% MXenes inside the epoxy, 1-h probe sonication was used. Approximate thickness of MXene sheet (Fig. 6a and b) was evaluated with transmission electron microscope (TEM). Intercalation of the epoxy between individual MXenes

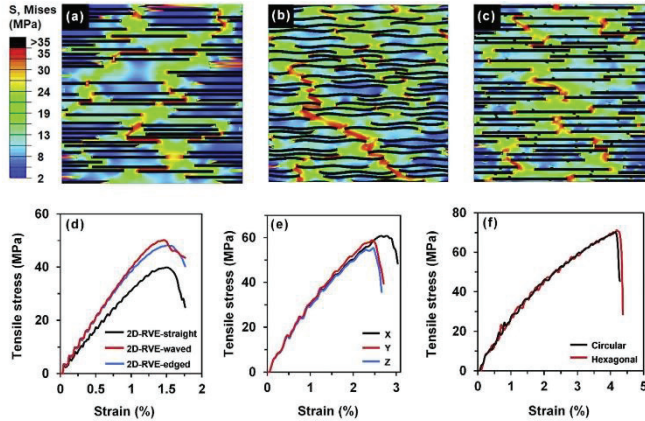


Fig. 4. Sensitivity analysis of different 2D and 3D RVE models: (a) Stress distribution in MXene-PVA model with aligned and straight MXenes (2D-RVE-straight); (b) A model with aligned and waved MXenes (2D-RVE-waved); (c) A model with aligned and edged MXenes (2D-RVE-edged); (d) 2D RVE MXene-PVA tensile results with straight, waved and edged MXenes; (e) 3D RVE MXene-epoxy tensile results with randomly oriented hexagonal-shaped MXenes under different tension directions; (f) 3D RVE MXene-epoxy tensile results with randomly oriented circular and hexagonal-shaped MXenes. (A colour version of this figure can be viewed online.)

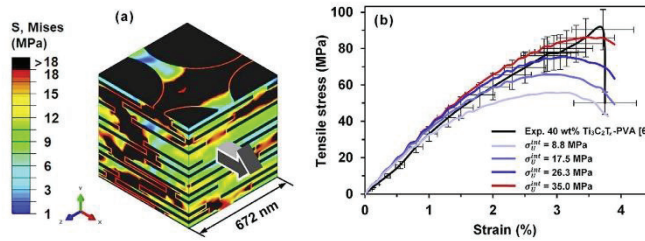


Fig. 5. 3D RVE aligned $\text{Ti}_3\text{C}_2\text{Tx}$ -PVA model calibration with experiment results: (a) Example of stress distribution inside 3D RVE model with an interface strength of 17.5 MPa; (b) Stress-strain curves of 3D RVE models with different interface strengths and comparison to experimental results, σ_y^{eff} – interface strength. (A colour version of this figure can be viewed online.)

flakes was also observed in several images (Fig. 6c), but such structure was not analyzed in the modeling.

The initial model was made of 3.6 vol% (10 wt%) MXenes, using the mass density of $\text{Ti}_3\text{C}_2\text{Tx}$ – 3.7 g/cm^3 [42] and neat epoxy – 1.25 g/cm^3 . Initial MXene's length was set for 200 nm, thickness for 10 nm and homogenized Young's modulus for 53 GPa, following the methods presented in Section 2.3. The adhesion between MXenes and epoxy was known to be strong due to its surface groups [43,44]. Therefore, the initial properties of the interface layer were the same as the matrix. A maximum principal stress criterion of 41.9 MPa was set for the epoxy matrix as the initiation of damage (Table 1).

Simulation results showed high-stress concentration at the edges of MXene sheets and low-stress values between the parallel particles (Fig. 6d). Crack pinning and deflection of the matrix were observed in fractured models (Fig. 6e). However, MXene sheets were not damaged during the tensile. Initial matrix cracks began to form at the strain of 2.7%, and complete fracture occurred at 4.4%. Tensile strength of the calibrated model was 34.7 MPa with 3.5% difference to experimental results (Fig. 6f).

From the calibration analysis, the following model parameters were obtained: MXene length – 250 nm, thickness – 8 nm,

homogenized Young's modulus of multi-layered MXenes – 66 GPa, damage evolution parameter of the epoxy – 0.5 nm displacement at failure. Homogenized Young's modulus of multi-layered MXenes was also in a good agreement with other studies [45], which analyzed anisotropic elastic properties of multi-layered $\text{Ti}_3\text{C}_2\text{Tx}$. Due to successful model calibration of MXene-epoxy composites with strong interface layer, further prediction modeling analysis of MXene-epoxy composites was carried without an interface layer.

3.4. Prediction analysis of MXene-epoxy composites

In both calibrations of MXene-PVA and MXene-epoxy models, interface properties were the same as the original matrix. All stress-strain curves simulated under dynamic explicit procedures were redefined with 6th-degree polynomial functions. Firstly, the comparison between randomly oriented and aligned MXene-epoxy models was made. The properties for both models were: 5 vol% and 100 AR of $\text{Ti}_3\text{C}_2\text{Tx}$ sheets. Both Young's modulus and tensile strength increased with the alignment of MXenes: from 4.1 GPa to 8 GPa, and from 52.7 MPa to 72.2 MPa, respectively (Fig. 7a).

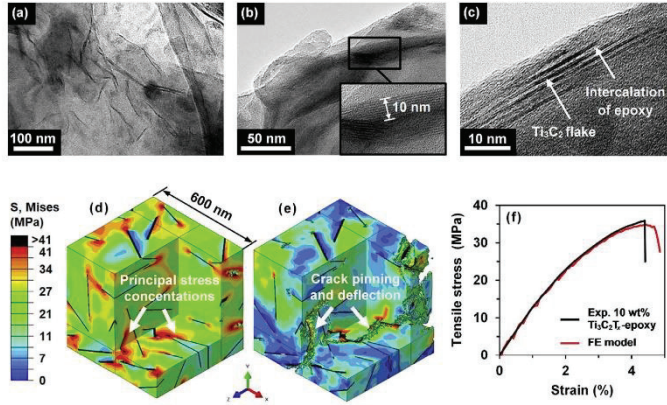


Fig. 6. MXene-epoxy composite, tensile experiment and modeling results: (a) TEM images of $\text{Ti}_3\text{C}_2\text{T}_x$ -epoxy composite with randomly oriented MXene sheets; (b) Multi-layered structure of MXene sheet; (c) Epoxy intercalation between the individual $\text{Ti}_3\text{C}_2\text{T}_x$ flakes; (d) Stress distribution inside 3.6 vol% randomly oriented $\text{Ti}_3\text{C}_2\text{T}_x$ -epoxy model, and the first crack formation (cut view); (e) Crack propagation within the model and stress drop after a full model fracture (cut view); (f) Stress-strain curve of calibrated 3D RVE model with 3.6 vol% (10 wt%) randomly oriented $\text{Ti}_3\text{C}_2\text{T}_x$ sheets and comparison with tensile experiment. (A colour version of this figure can be viewed online.)

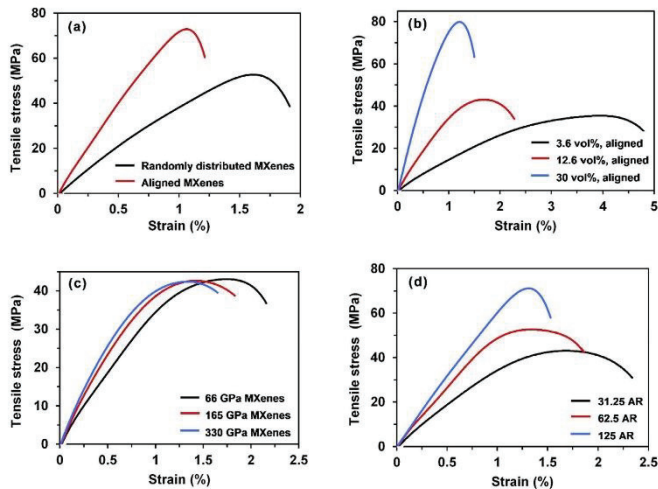


Fig. 7. Prediction analysis of various MXene-epoxy models: (a) The comparison of randomly oriented and aligned MXene flakes: 5 vol%, 100 AR; (b) The influence of volume fraction of aligned MXenes: 31.25 AR, 66 GPa homogenized Young's modulus; (c) The influence of homogenized Young's modulus of aligned MXenes: 12.6 vol%, 31.25 AR; (d) The influence of aspect ratio of aligned MXenes: 12.6 vol%, 66 GPa homogenized Young's modulus. (A colour version of this figure can be viewed online.)

The influence of volume fraction (3.6, 12.6 and 30 vol%) of aligned MXenes on tensile results was also explored. For these models, AR was set for 31.25 and homogenized MXene Young's modulus for 66 GPa, as obtained in Section 3.3. Modeling results showed that Young's modulus and tensile strength of RVE increased together with higher MXene volume fraction, from 1.5 GPa to 8.2 GPa and from 34.8 MPa to 80.3 MPa, respectively (Fig. 7b).

Another simulation was performed with different values of homogenized Young's modulus of aligned multi-layer $\text{Ti}_3\text{C}_2\text{T}_x$: 66,

165 and 330 GPa. The AR of MXenes was set for 31.25 and the volume fraction for 12.6%. No significant difference in tensile strength was noticed. However, Young's modulus increased from 3.8 GPa to 5.2 GPa (Fig. 7c).

The last simulation was performed with different AR values: 31.25, 62.5 and 125 (diameter of 250, 500, 1000 nm and thickness of 8 nm). These values were considered constant: Young's modulus of aligned MXenes – 66 GPa and volume fraction – 12.6%. From the simulation results, both Young's modulus and tensile strength

increased together with higher AR: from 3.9 GPa to 6.3 GPa and from 43.6 MPa to 73.1 MPa, respectively (Fig. 7d).

4. Conclusions

We performed a comprehensive computational analysis of multilayer MXene-PVA and MXene-epoxy models under tension for prediction of Young's modulus, tensile strength, and damage behaviors. Additionally, 3D RVE models with varying volume fractions, aspect ratios, alignment and Young's modulus of MXene sheets were analyzed. The model calibration was performed with aligned MXene-PVA films and randomly orientated MXene-epoxy tensile specimens, and the interaction between the matrices and particles was evaluated. The strength properties of the interface layer were calculated to be the same as the matrices for both MXene-PVA and MXene-epoxy composites, respectively. Homogenized Young's modulus of multi-layered MXenes was estimated for 22–66 GPa. The influence of the nanoparticle shape on mechanical properties was analyzed, assuming a circular MXene sheet. The average values of aspect ratio ranging from 25 to 31.25 were obtained from the calibrations of the model. Simulation results showed that Young's modulus and tensile strength increased with higher aspect ratio, volume fraction and alignment of the flakes. Much higher characteristics of MXene-epoxy composite were achieved with 30 vol% aligned MXenes when compared to neat epoxy. Young's modulus value increased 8.4 times and tensile strength – 1.91 times. Predicted mechanical properties received from the modeling give insights for further high-strength multifunctional MXene-polymer film development, which can be considered for structural health monitoring applications or lightweight coatings for electromagnetic interference shielding.

Declaration of competing interest

The authors declare that they have no known competing financial interests or personal relationships that could have appeared to influence the work reported in this paper.

CRediT authorship contribution statement

G. Monastyreckis: Methodology, Software, Validation, Formal analysis, Investigation, Resources, Data curation, Writing - original draft, Writing - review & editing, Visualization. **L. Mishnaevsky:** Conceptualization, Methodology, Software, Formal analysis, Resources, Writing - review & editing, Visualization, Supervision. **C.B. Hatter:** Validation, Investigation, Data curation, Writing - review & editing. **A. Aniskevich:** Conceptualization, Formal analysis, Resources, Writing - review & editing, Supervision, Project administration, Funding acquisition. **Y. Gogotsi:** Conceptualization, Formal analysis, Resources, Writing - review & editing, Visualization, Supervision. **D. Zeleniakieni:** Conceptualization, Methodology, Software, Validation, Formal analysis, Investigation, Resources, Writing - original draft, Writing - review & editing, Visualization, Supervision, Project administration, Funding acquisition.

Acknowledgment

This project has received funding from the European Union's Horizon 2020 research and innovation program under the Marie Skłodowska-Curie grant agreement No 777810.

Appendix A. Supplementary data

Supplementary data to this article can be found online at <https://doi.org/10.1016/j.carbon.2020.02.070>.

References

- [1] M.Q. Zhao, C.E. Ren, Z. Ling, M.R. Lukatskaya, C. Zhang, K.L. Van Aken, et al., Flexible MXene/carbon nanotube composite paper with high volumetric capacitance, *Adv. Mater.* 27 (2015) 339–345, <https://doi.org/10.1002/adma.201404140>.
- [2] F. Shahzad, M. Alhabeib, C.B. Hatter, B. Anasori, S.M. Hong, C.M. Koo, et al., Electromagnetic interference shielding with 2D transition metal carbides (MXenes), *Science* 353 (2016) 1137–1140, <https://doi.org/10.1126/science.aag2421>.
- [3] C.J. Zhang, B. Anasori, A.S. Ascaso, S.-H. Park, N. McEvoy, A. Shmeliov, et al., Transparent, flexible, and conductive 2D titanium carbide (MXene) films with high volumetric capacitance, *Adv. Mater.* (2017) 1–9, <https://doi.org/10.1002/adma.201702678>, 1702678.
- [4] M. Naguib, M. Kurtoglu, V. Presser, J. Lu, J. Niu, M. Heon, et al., Two-dimensional nanocrystals produced by exfoliation of Ti_3AlC_2 , *Adv. Mater.* 23 (2011) 4248–4253, <https://doi.org/10.1002/adma.201102306>.
- [5] M. Naguib, O. Mashtalir, J. Carle, V. Presser, J. Lu, L. Hultman, et al., Two-dimensional transition metal carbides, *ACS Nano* 6 (2012) 1322–1331, <https://doi.org/10.1021/nm204153h>.
- [6] Z. Ling, C.E. Ren, M.-Q. Zhao, J. Yang, J.M. Giammarco, J. Qiu, et al., Flexible and conductive MXene films and nanocomposites with high capacitance, *Proc. Natl. Acad. Sci. Unit. States Am.* 111 (2014) 16676–16681, <https://doi.org/10.1073/pnas.1414215111>.
- [7] W. Zhi, S. Xiang, R. Bian, R. Lin, K. Wu, T. Wang, et al., Study of MXene-filled polyurethane nanocomposites prepared via an emulsion method, *Compos. Sci. Technol.* 168 (2018) 404–411, <https://doi.org/10.1016/j.compscitech.2018.10.026>.
- [8] S. Li, X. Zou, X. Xiong, K. Zheng, X. Lu, Z. Zhou, et al., Electrosynthesis of Ti_3AlC_2 from oxides/carbon precursor in molten calcium chloride, *J. Alloys Compd.* 735 (2018) 1901–1907, <https://doi.org/10.1016/j.jallcom.2017.11.342>.
- [9] M. Alhabeib, K. Maleski, B. Anasori, P. Lelyukh, L. Clark, S. Sin, et al., Guidelines for synthesis and processing of two-dimensional titanium carbide ($\text{Ti}_3\text{C}_2\text{T}_x$ MXene), *Chem. Mater.* 29 (2017) 7633–7644, <https://doi.org/10.1021/acs.chemmater.7b02847>.
- [10] K. Maleski, V.N. Mochalin, Y. Gogotsi, Dispersions of two-dimensional titanium carbide MXene in organic solvents, *Chem. Mater.* 29 (2017) 1632–1640, <https://doi.org/10.1021/acs.chemmater.6b04830>.
- [11] M.A. Huse, A.C. Forse, K.J. Griffith, M.R. Lukatskaya, M. Ghidui, Y. Gogotsi, et al., NMR reveals the surface functionalisation of $\text{Ti}_3\text{C}_2\text{MXene}$, *Phys. Chem. X* 18 (2016) 5099–5102, <https://doi.org/10.1039/c6cp00330c>.
- [12] L. Mishnaevsky Jr., G. Dai, Hybrid and hierarchical nanoreinforced polymer composites : computational modelling of structure – properties relationships, *Compos. Struct.* 117 (2014) 156–168, <https://doi.org/10.1016/j.comstruct.2014.06.027>.
- [13] G. Dai, L. Mishnaevsky Jr., Fatigue of multiscale composites with secondary nanoplatelet reinforcement : 3D computational analysis, *Compos. Sci. Technol.* 91 (2014) 71–81, <https://doi.org/10.1016/j.compscitech.2013.11.024>.
- [14] A. Lipatov, M. Alhabeib, M.R. Lukatskaya, A. Bosh, Y. Gogotsi, A. Sinitskii, Effect of synthesis on quality, electronic properties and environmental stability of individual monolayer Ti_3C_2 MXene flakes, *Adv. Electron. Mater.* 2 (2016) 1–9, <https://doi.org/10.1002/aeml.201600255>, 1600255.
- [15] V.N. Borysiuk, V.N. Mochalin, Y. Gogotsi, Bending rigidity of two-dimensional titanium carbide (MXene) nanoribbons: a molecular dynamics study, *Comput. Mater. Sci.* 143 (2018) 418–424, <https://doi.org/10.1016/j.commatsci.2017.11.028>.
- [16] A. Feng, Y. Yu, F. Jiang, Y. Wang, L. Mi, Y. Yu, et al., Fabrication and thermal stability of NH_4HF_2 -etched Ti_3C_2 MXene, *Ceram. Int.* 43 (2017) 6322–6328, <https://doi.org/10.1016/j.ceramint.2017.02.039>.
- [17] S. Xu, G. Wei, J. Li, W. Han, Y. Gogotsi, Flexible MXene-graphene electrodes with high volumetric capacitance for integrated co-cathode energy conversion/storage devices, *J. Mater. Chem.* 5 (2017) 17442–17451, <https://doi.org/10.1039/c7ja005721k>.
- [18] Y. Cao, Q. Deng, Z. Liu, D. Shen, T. Wang, Q. Huang, et al., Enhanced thermal properties of poly(vinylidene fluoride) composites with ultrathin nanosheets of MXene, *RSC Adv* 7 (2017) 20494–20501, <https://doi.org/10.1039/C7RA00184C>.
- [19] A.M. Jastrzębska, A. Szuplewska, T. Wojciechowski, M. Chudy, W. Ziemkowska, L. Chlubny, et al., In vitro studies on cytotoxicity of delaminated Ti_3C_2 MXene, *J. Hazard Mater.* 339 (2017) 1–8, <https://doi.org/10.1016/j.jhazmat.2017.06.004>.
- [20] T. Zhang, L. Pan, H. Tang, F. Du, Y. Guo, T. Qiu, et al., Synthesis of two-dimensional $\text{Ti}_3\text{C}_2\text{T}_x$ MXene using $\text{HCl}+\text{LiF}$ etchant: enhanced exfoliation and delamination, *J. Alloys Compd.* 695 (2017) 818–826, <https://doi.org/10.1016/j.jallcom.2016.10.127>.
- [21] K. Maleski, C.E. Ren, M.-Q. Zhao, B. Anasori, Y. Gogotsi, Size-dependent physical and electrochemical properties of two-dimensional MXene flakes, *ACS Appl. Mater. Interfaces* 10 (2018) 24491–24498, <https://doi.org/10.1021/acsmi.8b04652>.
- [22] O. Mashtalir, M. Naguib, V.N. Mochalin, Y. Dall'Agnesse, M. Heon, M.W. Barsoum, et al., Intercalation and delamination of layered carbides and carbonitrides, *Nat. Commun.* 4 (7) (2013) 1716, <https://doi.org/10.1038/ncomms2664>.
- [23] A.M. Jastrzębska, E. Karwowska, T. Wojciechowski, W. Ziemkowska,

- A. Rozmystowska, L. Chlubny, et al., The atomic structure of Ti_3C_2 and Ti_3C_2 MXenes is responsible for their antibacterial activity toward *E. coli* bacteria, *J. Mater. Eng. Perform.* 28 (2018) 1272–1277, <https://doi.org/10.1007/s11665-018-3223-z>.
- [24] W. Feng, H. Luo, Y. Wang, S. Zeng, Y. Tan, H. Zhang, et al., Ultrasonic assisted etching and delaminating of Ti_3C_2 MXene, *Ceram. Int.* 44 (2018) 7084–7087, <https://doi.org/10.1016/j.ceramint.2018.01.147>.
- [25] L. Chen, X. Shi, N. Yu, X. Zhang, Xiaoze Du, J. Lin, Measurement and analysis of thermal conductivity of $Ti_3C_2T_x$ MXene films, *Materials (Basel)* 11 (2018) 1701, <https://doi.org/10.3390/ma11091701>.
- [26] V.N. Borysiuk, V.N. Mochalin, Y. Gogotsi, Molecular dynamic study of the mechanical properties of two-dimensional titanium carbides $Ti_{n+1}C_n$ (MXenes), *Nanotechnology* 26 (2015) 265705, <https://doi.org/10.1088/0957-4484/26/26/265705>.
- [27] G. Plummer, B. Anasori, Y. Gogotsi, G.J. Tucker, Nanoindentation of monolayer $Ti_{n+1}C_nT_x$ MXenes via atomistic simulations: the role of composition and defects on strength, *Comput. Mater. Sci.* 157 (2019) 168–174, <https://doi.org/10.1016/j.commatsci.2018.10.033>.
- [28] X. Sang, Y. Xie, M. Lin, M. Alhabeb, K.L. Van Aken, Y. Gogotsi, et al., Atomic defects in monolayer titanium carbide, *ACS Nano* 10 (2016) 9193–9200, <https://doi.org/10.1021/acsnano.6b05240>.
- [29] A. Lipatov, H. Lu, M. Alhabeb, B. Anasori, A. Gruverman, Y. Gogotsi, et al., Elastic properties of 2D $Ti_3C_2T_x$ MXene monolayers and bilayers, *Sci. Adv.* 4 (2018), <https://doi.org/10.1126/sciadv.aat0491> eaat0491.
- [30] L. Wu, L. Noels, L. Adam, I. Doghri, A multiscale mean-field homogenization method for fiber-reinforced composites with gradient-enhanced damage models, *Comput. Methods Appl. Mech. Eng.* (2012) 233–236, <https://doi.org/10.1016/j.cma.2012.04.011>, 164–179.
- [31] M. Pahlavanpour, P. Hubert, M. Lévesque, Numerical and analytical modeling of the stiffness of Polymer-Clay Nanocomposites with aligned particles: one- and two-step methods, *Comput. Mater. Sci.* 82 (2014) 122–130, <https://doi.org/10.1016/j.commatsci.2013.09.038>.
- [32] L. Mishnaevsky Jr., Micromechanical analysis of nanocomposites using 3D voxel based material model, *Compos. Sci. Technol.* 72 (2012) 1167–1177, <https://doi.org/10.1016/j.compscitech.2012.03.026>.
- [33] D. Zeleniakienė, P. Griskevičius, V. Norvydas, A. Aniskevich, K. Zukienė, Simulation of mechanical behaviour of polychloroprene/versatic acid vinyl ester/methyl methacrylate/2-ethylhexyl acrylate copolymer blend, *Iran. Polym. J.* 27 (2018) 97–103, <https://doi.org/10.1007/s13726-017-0590-5>.
- [34] A. Tchalla, W.L. Azoti, Y. Koutsawa, A. Makradi, S. Belouettar, H. Zahrouni, Incremental mean-fields micromechanics scheme for non-linear response of ductile damaged composite materials, *Compos. Part B Eng.* 69 (2015) 169–180, <https://doi.org/10.1016/j.compositesb.2014.08.055>.
- [35] L. Mishnaevsky Jr., Composites : Part B Nanostructured interfaces for enhancing mechanical properties of nanocomposites : computational micro-mechanical studies, *Compos. Part B.* 68 (2015) 75–84, <https://doi.org/10.1016/j.compositesb.2014.08.029>.
- [36] G. Dai, L. Mishnaevsky Jr., Graphene reinforced nanocomposites: 3D simulation of damage and fracture, *Comput. Mater. Sci.* 95 (2014) 684–692, <https://doi.org/10.1016/j.commatsci.2014.08.011>.
- [37] S. Wang, J.X. Li, Y.L. Du, C. Cui, First-principles study on structural, electronic and elastic properties of graphene-like hexagonal Ti_2C monolayer, *Comput. Mater. Sci.* 83 (2014) 290–293, <https://doi.org/10.1016/j.commatsci.2013.11.025>.
- [38] G. Dai, L. Mishnaevsky Jr., Damage evolution in nanoclay-reinforced polymers: a three-dimensional computational study, *Compos. Sci. Technol.* 74 (2013) 67–77, <https://doi.org/10.1016/j.compscitech.2012.10.003>.
- [39] S. Kilikevicius, S. Kvietaikė, K. Zukienė, M. Omastová, A. Aniskevich, D. Zeleniakienė, Numerical investigation of the mechanical properties of a novel hybrid polymer composite reinforced with graphene and MXene nanosheets, *Comput. Mater. Sci.* 174 (2020) 109497, <https://doi.org/10.1016/j.commatsci.2019.109497>.
- [40] J. Liu, Y. Wu, J. Shen, Y. Gao, L. Zhang, D. Cao, Polymer–nanoparticle interfacial behavior revisited: a molecular dynamics study, *Phys. Chem. Chem. Phys.* 13 (2011) 13058–13069, <https://doi.org/10.1039/c0cp02952a>.
- [41] S.E. Harton, S.K. Kumar, H. Yang, T. Koga, K. Hicks, H. Lee, et al., Immobilized polymer layers on spherical nanoparticles, *Macromolecules* 43 (2010) 3415–3421, <https://doi.org/10.1021/ma902484d>.
- [42] J. Yan, C.E. Ren, K. Maleski, C.B. Hatter, B. Anasori, P. Urbankowski, et al., Flexible MXene/graphene films for ultrafast supercapacitors with outstanding volumetric capacitance, *Adv. Funct. Mater.* 27 (10) (2017) 1701264, <https://doi.org/10.1002/adfm.201701264>.
- [43] R. Liu, W. Li, High-Thermal-Stability and high-thermal-conductivity $Ti_3C_2T_x$ MXene/poly(vinyl alcohol) (PVA) composites, *ACS Omega* 3 (3) (2018) 2609–2617, <https://doi.org/10.1021/acsomega.7b02001>.
- [44] H. Zhang, L. Wang, A. Zhou, C. Shen, Y. Dai, F. Liu, et al., Effects of 2-D transition metal carbide $Ti_3C_2T_x$ on properties of epoxy composites, *RSC Adv.* 6 (90) (2016) 87341–87352, <https://doi.org/10.1039/c6ra14560d>.
- [45] J. Come, Y. Xie, M. Naguib, S. Jesse, S.V. Kalinin, Y. Gogotsi, et al., Nanoscale elastic changes in 2D $Ti_3C_2T_x$ (MXene) pseudocapacitive electrodes, *Adv. Energy Mater.* (9) (2016) 1502290, <https://doi.org/10.1002/aenm.201502290>.

Article

Deformation and Failure of MXene Nanosheets

Daiva Zeleniakienė^{1,*}, Gediminas Monastyreckis¹, Andrey Aniskevich²
and Paulius Griskevicius¹

¹ Department of Mechanical Engineering, Kaunas University of Technology, 51424 Kaunas, Lithuania; gediminas.monastyreckis@ktu.edu (G.M.); paulius.griskevicius@ktu.lt (P.G.)

² Institute for Mechanics of Materials, University of Latvia, LV-1004 Riga, Latvia; andrey.aniskevich@pmi.lv

* Correspondence: daiva.zeleniakienė@ktu.lt; Tel.: +37-037-323-498

Received: 10 February 2020; Accepted: 8 March 2020; Published: 10 March 2020



Abstract: This work is aimed at the development of finite element models and prediction of the mechanical behavior of MXene nanosheets. Using LS-Dyna Explicit software, a finite element model was designed to simulate the nanoindentation process of a two-dimensional MXene $Ti_3C_2T_z$ monolayer flake and to validate the material model. For the evaluation of the adhesive strength of the free-standing $Ti_3C_2T_z$ -based film, the model comprised single-layered MXene nanosheets with a specific number of individual flakes, and the reverse engineering method with a curve fitting approach was used. The interlaminar shear strength, in-plane stiffness, and shear energy release rate of MXene film were predicted using this approach. The results of the sensitivity analysis showed that interlaminar shear strength and in-plane stiffness have the largest influence on the mechanical behavior of MXene film under tension, while the shear energy release rate mainly affects the interlaminar damage properties of nanosheets.

Keywords: MXene; mechanical behavior; finite element modeling

1. Introduction

A new class of two-dimensional (2D) nanomaterials, MXenes, was discovered in the last decade [1]. MXenes are transition metal carbides or nitrides produced by the etching of the A element from the MAX phases. Typically, nanomaterials can be divided into two groups: hydrophilic but not conductive, such as transition metal oxides or clays; and conductive but not hydrophilic, such as graphene. However, some MXenes (Ti_2CT_z , $Ti_3C_2T_z$) have the unique characteristics of both groups. Due to the combination of the electrical conductivity of transition metal carbides and the hydrophilicity of hydroxyl or oxygen-terminated surfaces, these MXenes behave as “conductive clays” [2].

MXenes have been widely investigated during the past few years. The main interest has been directed at the electric properties, their applications for sensors, energy storage (batteries, supercapacitors, hydrogen evolution reaction catalysts), harvesting, electromagnetic shielding, tribology, etc. [3–6]. Pioneer studies of the mechanical properties of MXenes showed promising results [1,2,7]. Elastic properties were obtained experimentally by nanoindentation with the tip of an atomic force microscope (AFM) and the elastic modulus of the most investigated MXene material, $Ti_3C_2T_z$, was obtained at 0.33 ± 0.03 TPa [8]. According to classical molecular dynamics simulation [7], which does not take into account various material defects, the modulus was higher and equal to 0.502 TPa.

MXenes exhibit a high bending stiffness [9]. The critical deformations are much higher than the graphene ones, and this is an important feature of flexible electronics [4,10,11]. MXenes have good interactions with polymeric matrices for polymer composite applications [4,12,13]. For these reasons, MXene could be a good candidate to provide electrical conductivity for fiber-reinforced plastic composites without losing desirable mechanical properties and imparting additional self-sensing

functions. While some of the mechanical properties of MXene have been determined theoretically or experimentally, the mechanical behavior of MXene, and particularly its failure mechanisms, has not been studied well, and there is a huge lack of data that are needed for the development of polymer composites filled with MXene 2D nanosheets.

The aim of this study was to investigate the micromechanical behavior of MXene nanosheets by developing finite element (FE) computational models. The objectives were to (1) develop an FE model composed of single-layered MXenes nanosheets with a specific number of individual flakes for explicit analysis; and (2) identify the material parameters by FE simulation of interface shearing. The novelty of this study is that it shows first insights into the deformation and failure mechanisms of this new nanomaterial, as well as providing a basis for the future design of polymer composites reinforced with MXene nanosheets, and the development of MXene–polymer coatings with high-density MXene–MXene interactions.

2. Modeling Methods

2.1. FE Model of Nanoindentation

The main purpose of this presimulation was to build an explicit FE model of a $\text{Ti}_3\text{C}_2\text{T}_z$ MXene monolayer flake for analysis of the nanoindentation process in LS-Dyna software and, using the force vs. deflection curve, validate the FE model and material characteristics. The FE model (Figure 1) was developed according to the experimental data presented by Lipatov et al. [8], where it was considered that the MXene flake has isotropic properties, and therefore, the membrane can be parametrized using Young's modulus, E and Poisson's ratio, ν .

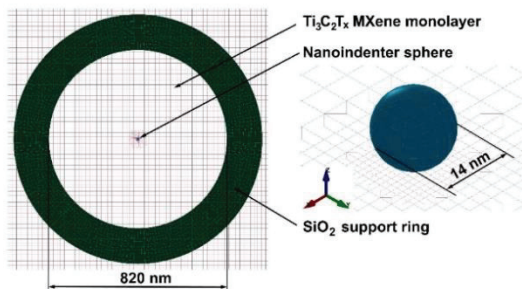


Figure 1. Finite element (FE) model for the nanoindentation process analysis.

The thickness of the $\text{Ti}_3\text{C}_2\text{T}_z$ monolayer flake is an important parameter as it influences the results of the nanoindentation experiments. Using AFM for the determination of the thickness of monolayers of 2D materials has some limitations. The $\text{Ti}_3\text{C}_2\text{T}_z$ MXene flake thicknesses obtained by AFM can differ significantly [8,14], and this directly affects the determined value of Young's modulus. MXene flakes with a thickness of 0.98 nm were modeled [1,2,11]. The mechanical properties of MXenes and the SiO_2 support ring used in the model are based on the analysis of the literature data. The indenter was a diamond crystal with a modulus of 1 TPa. The mechanical properties of the materials used in the nanoindentation simulation are presented in Table 1.

Table 1. Mechanical properties of materials used in the simulation of nanoindentation.

Material	Density, ρ , g/cm ³	Elastic Modulus, E , GPa	Poisson's Ratio, ν	Tensile Strength, σ_u , GPa
Ti ₃ C ₂ T ₂	3.19 [8]	333 [8]	0.227 [15]	17.3 [8]
SiO ₂ [16]	2.65	70.0	0.17	-
Diamond nanoindenter	3.50	1000	0.20	-

The 2D Ti₃C₂T₂ MXene flake was modeled with shell elements using a linear elastic material model. The size of the shell elements was 10 nm, while the center of the monolayer (contact zone with nanoindenter) was decreased to as little as 1.25 nm. The nanoindenter was defined as an elastic solid sphere (diameter 14 nm). The bottom of the MXene flakes was supported on the ring surface of SiO₂, which was fully fixed. Two pinball-type contacts (AUTOMATIC_NODES_TO_SURFACE) were used: surface of SiO₂—bottom flake, and surface of the nanoindenter—top flake. Two simulations were performed with initial pretension and without. As it was an explicit analysis, the initial pretension initiated the oscillation of the flake; therefore, the *CONTROL_DYNAMIC_RELAXATION must be activated.

The indentation was described by the dependence of the displacement on time. By linearly increasing the displacement, which gives a constant velocity, a small impact phenomenon was obtained in the model, and this initiated the vibrations of the MXene monolayer flake. Finally, a smooth increase in the displacement was chosen based on the assumption that the average speed of the nanoindenter is equal to ~1 m/s, and the speed increases linearly from 0 up to the $2v_{avg}$. The loading curve displacement vs. time was obtained by the function $u(t) = \int v(t)dt$.

A methodology for deriving the material parameters from experimental results, known as parameter identification, was applied here using the optimization procedure. The same nanoindentation FE model without initial pretension has been chosen to evaluate the sensitivity of the material and the geometric parameters to the mechanical behavior of the sample. The Young's modulus and flake thickness were chosen as variables. The Young's modulus varied between 200 and 400 GPa and the thickness from 0.4 to 1.5 nm. The mean square error was used as a curve fitting metric. The experimental force, F vs. deflection δ curve can be described by the following equation [8]:

$$F = \sigma_0^{2D} \pi r \delta + E^{2D} q^3 \frac{\delta^3}{r^2}, \quad (1)$$

where $\sigma_0^{2D} = \frac{\sigma}{h}$ represents the prestress in the membrane, $E^{2D} = \frac{E}{h}$ is the 2D elastic modulus (thickness $h = 0.98$ nm), and r is the radius of the well [8]. The dimensionless constant, q , is related to ν as $q = 1/(1.049 - 0.15\nu - 0.16\nu^2) = 0.9933$. The first term in Equation (1) corresponds to the prestretched membrane regime and is valid for small loads. The second term for the nonlinear membrane behavior is characterized by a cubic $F \sim \delta^3$ relationship with a coefficient of E^{2D} , which dominates at large loads. For comparison, only the second part of Equation (1) was used; therefore, the prestretching was not taken into account during the simulation.

2.2. FE Model of Pure MXene Film

The stability of the stacked two-dimensional transition metal carbides and their interlayered friction in different configurations are comparatively studied by means of density functional theory. In recent years, the adhesive interactions of monolayers and few-layer 2D materials have been intensively investigated. At equilibrium, a larger interlayer distance corresponds to a smaller binding energy, suggesting an easier sliding between the layers [17]. Nanoindentation has been widely used to characterize the adhesion of thin films [18–20]. One of the important questions is to understand how the properties—in particular, adhesive strength—change when transitioning from bulk to 2D forms of the material. However, to our knowledge, no theoretical or experimental studies of the adhesive

properties of MXenes have been reported to date. The results of direct AFM measurements of adhesion of two MXenes, $Ti_3C_2T_z$ and Ti_2CT_z , with a SiO_2 -coated Si spherical tip is one of the recent studies of adhesion properties [17].

One of the ways to analyze adhesive strength is to apply the reverse engineering method. Assuming that adhesion energy between surfaces of free-standing MXene nanosheets exists [21], then the strength of the interlayer surface has to depend on the overlapping area. For the study of adhesive interactions, the experimental tensile test data of the assembled free-standing $Ti_3C_2T_z$ -based films [4] were used. It was assumed that the single-layered nanosheet has a square form of $1 \mu m$ length [22–25], consisting of 18 $Ti_3C_2T_z$ individual flakes and an average thickness of 20 nm [25]. In total, 164 layers of single-layered nanosheets per film of $3.3 \mu m$ thickness were used in experimental testing [4]. As the overlapping of nanosheets has an essential influence on the strength of the interlayer surface, a 2D analysis of randomly placed rectangle nanosheets was performed using materials modeling software, Digimat. For the overlapping analysis, MXene nanosheets with dimensions of $1000 \times 20 \text{ nm}$ were chosen. The overall thickness of MXene film formed from these nanosheets was $3.3 \mu m$, as it was in testing [4] (Figure 2a). The results show that the average overlapping of nanosheets is 20% (Figure 2b). This overlap value was used to create the FE model.

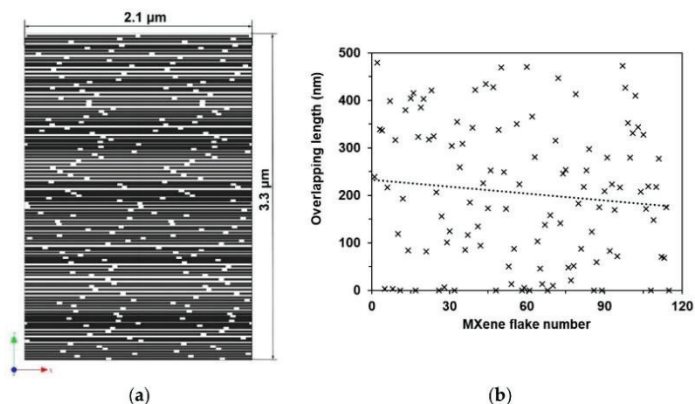


Figure 2. Estimation of nanosheets overlapping: (a) segment of the Digimat model of free-standing $Ti_3C_2T_z$ film, (b) obtained overlapping length distribution by simulation of randomly placed nanosheets.

For FE simulation of the interface shear strength of MXene nanosheets ($1000 \text{ nm} \times 1000 \text{ nm} \times 20 \text{ nm}$), three- (Figure 3a) and nineteen- (Figure 3b) layer models were developed with an overlapping length of 200 nm (20%).

The FE model was designed taking into account the experimental setup data presented in the study [4]. The single-layered $Ti_3C_2T_z$ MXene nanosheet was modeled with shell elements. The Young's modulus of the MXene nanosheet was set at 333 GPa; Poisson's ratio—0.227; the size of shell elements—5 nm. The nodes on the left-side edges had a fixed 4 degrees-of-freedom, allowing free contraction in the x -direction and rotation about the z -axis. For the right-side nodes, the displacement vs. time $u(t)$ was applied with a speed of 1 mm/ms. The interface between the single-layered nanosheets was modeled using tiebreak contact, *CONTACT_AUTOMATIC_ONE_WAY_SURFACE_TO_SURFACE_TIEBREAK. The discrete crack model with power-law damage, which works with offset shell elements (option = 11), shown in Figure 4, was chosen. The parameters needed to describe tiebreak contact are presented in Table 2.

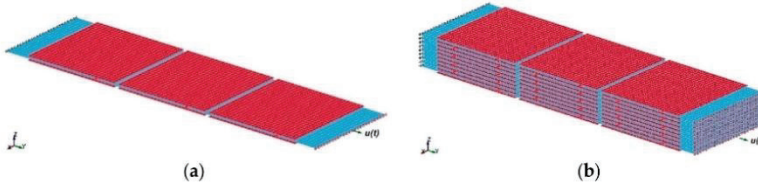


Figure 3. FE model for the simulation of MXene nanosheet interface shear strength with 20% overlapping length: (a) 3-nanosheets-thick model, (b) 19-nanosheets-thick model. Red and blue colors are used for contrast to better show the single-layered nanosheets.

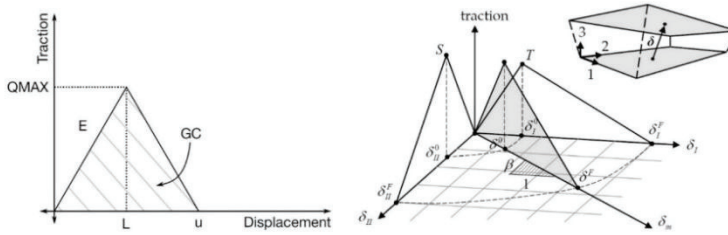


Figure 4. Bilinear traction–separation and the mixed-mode traction–separation law [26].

Table 2. The parameters used for the simulation of shear strength between nanosheet interfaces.

Normal Failure Stress, nfs (T), MPa	Shear Failure Stress, sfs (S), Mpa	Normal Energy Release Rates, eraten (G _{1c}) nj/m ²	Shear Energy Release Rates, erates (G _{IIc}) nj/m ²	Ratio of Tangential Stiffness to Normal Stiffness, ct2cn	Normal Stiffness, Cn ϵ, MPa/μm
2 ÷ 4	2 ÷ 4	30 ÷ 60	30 ÷ 60	1	200–350

The internal force acting per nanosheet was calculated from the experimentally determined [4] tensile strength value as follows,

$$F_{1L} = \sigma_u h w, \tag{2}$$

where σ_u —experimentally determined [4] ultimate stress; h —nanosheet thickness; w —nanosheet width. $F_{1L} = \sigma_{max} h w = 22(\text{Mpa}) \times 20(\text{nm}) \times 1(\text{nm}) = 440.0 \text{ nN}$.

The strength of the assembled free-standing $\text{Ti}_3\text{C}_2\text{T}_x$ -based film depends on the nanosheet interface shear strength,

$$\tau_u = \frac{F_{1L}}{OVL \times L \times w} = \frac{\sigma_u h}{OVL \times L} \tag{3}$$

where OVL —overlapping coefficient; L —nanosheet length; $\tau_u = \frac{22(\text{MPa}) \times 20(\text{nm})}{0.2 \times 1000(\text{nm})} = 2.2 \text{ MPa}$.

The minimum interlayer strength value achieved by an average overlapping length of 20% satisfies the experimental results [4]. For an FE model of three layers of MXene nanosheets $L_{ovl} = 2200 \text{ nm}$, the maximum resultant load acting on MXenes nanosheet cross-sections is the following:

$$F_{max} = \tau_u(\text{Mpa}) \times n_l \times OVL \times L \times w = 2.2 \times 2 \times 0.2 \times 1000(\text{nm}) \times 1000(\text{nm}) = 880 \text{ nN} \tag{4}$$

where n_l —the number of interfaces between three nanosheets.

This value was used as the criteria to validate the FE model for interface shear strength simulation. The graphical optimization tool LS-OPT was used for the identification of material constants.

The material parameters were obtained using the curve fitting approach with the parameterized simulation of the physical tests and calibration to the test results. The objective was to minimize the mean squared error between the test results [4] and the FE simulation results.

The loading was described by a curve of linearly increased displacement vs. time. As was mentioned before, this gives a constant velocity, which initiates vibration of the structure and makes its behavior uncertain. Therefore, in the second step, a smooth increase of displacement was chosen for loading, from the assumption that an average speed of tensile loading is equal to ~ 1 m/s, and speed is increasing linearly from 0 up to the $2v_{avg}$. The loading curve, displacement versus time, was obtained by integrating the linearly increasing velocity function: $u(t) = \int v(t)dt$ (Figure 5a). The response $F(t)$ was used for the curve fitting procedure and, for FE model validation, it was transformed into the $F(u)$ curve (Figure 5b). Using Equation (2), the experimental tensile curve [4] was recalculated into a force versus displacement curve and used for model validation.

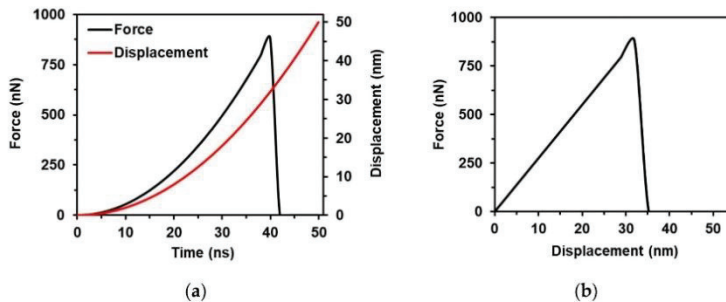


Figure 5. Dependencies for FE modeling: (a) displacement vs. time curve used for loading (red) and force vs. time for the curve fitting procedure (black); (b) force vs. displacement curve recalculated from the experiments [4].

3. Results

3.1. FE Simulation of Nanoindentation

The simulated deflection field of the indented MXene monolayer flake is presented in Figure 6. The highest deflection of 34 nm was reached at the center point of the MXene flake. The dependence of velocity of the nanoindenter and the center point of the MXene monolayer flake on time shows a linear behavior (Figure 7a). Analyzing the deflection of the nanoindenter and the center point of the MXene monolayer flake as a function of time, the dependence is observed to be nonlinear (Figure 7b).

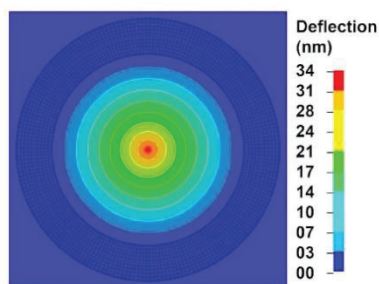


Figure 6. Simulated deflection field of the Ti₃C₂T_x MXene monolayer.

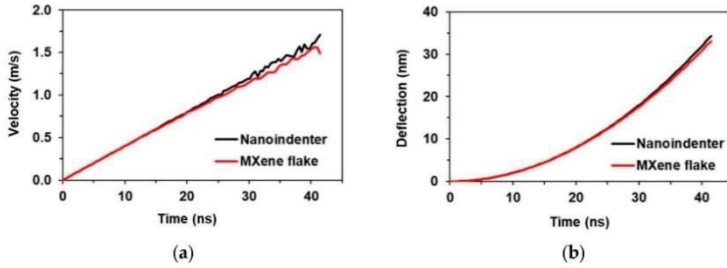


Figure 7. FE results of the nanoindentation simulation: (a) velocity of the nanoindenter and the center point of the MXene monolayer flake, (b) deflection of the nanoindenter and the center point of the MXene monolayer flake.

The influence of MXene monolayer flake thickness (Figure 8a) and Young's modulus (Figure 8b) on the force vs. deflection curve was analyzed. The results of thickness influence showed that if the Young's modulus of the MXene monolayer flake is set as $E = 333$ GPa, the best fit to the experimental result is obtained when the thickness is equal to 1.1 nm, which is higher than results presented in the literature [1,2,11]. On the other hand, if we use a thickness of 0.98 nm, the best fit appears at a Young's modulus of 380 MPa. To achieve the same results as the experimental ones, for finite element modeling, the thickness of the MXene monolayer flake should be increased from 0.98 to 1.1 nm, or the Young's modulus should be increased from 333 to 380 GPa.

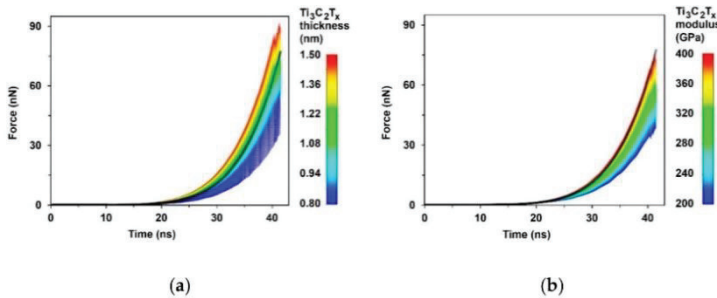


Figure 8. Sensitivity analysis results: (a) thickness influence on the force vs. deflection curve when $E = 333$ GPa; (b) Young's modulus influence on the force vs. deflection curve when $h = 0.98$ nm.

3.2. FE Simulation of Pure MXene Film

To simulate the behavior of pure MXene film under tension conditions, three constants were selected for calibration and sensitivity analysis: interlaminar shear strength, stiffness, and the energy release rate used for damage calculation. The results obtained by the curve fitting approach are shown in Figure 9. The best fitted FE curve was obtained using an interlaminar shear strength $\tau_{interl} = 2.2$ MPa, in-plane stiffness $E_{interl} = 0.26 \frac{\text{GPa}}{\mu\text{m}}$, and a shear energy release rate $G_{IIc} = 3.8 \cdot 10^{-2} \frac{\text{J}}{\text{m}^2}$. The results show that the behavior of tensioned film of free-standing MXene nanosheets is most sensitive to their interlaminar shear strength and in-plane stiffness, while the shear energy release rate mainly influences the interlaminar damage properties of nanosheets.

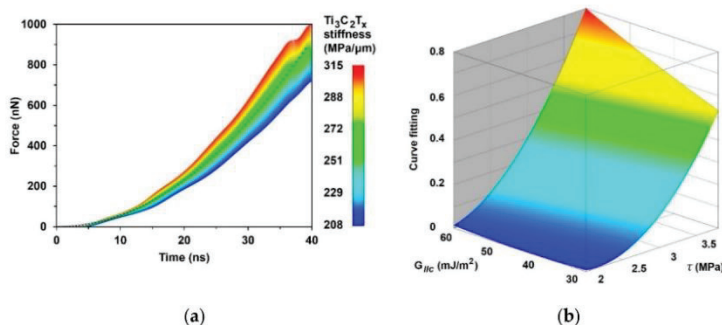


Figure 9. Sensitivity analysis of free-standing three-layer MXene nanosheets: (a) force vs. time curve sensitivity upon in-plane stiffness E_{interl} ; \times —experimental results obtained from [4] and curve fitting of MXenes, (b) influence of the interlaminar shear strength and shear energy release rate as $E_{interl} = 0.26 \frac{G_{IC}}{\mu m}$.

The material parameters identified by FE modeling were based on 20% of the random average overlapping of nanosheets. In the validated FE model, we changed the overlapping of nanosheets by up to 50% and evaluated the behavior of the ideal overlapping case (Figure 10a). By the FE simulations obtained, the force versus displacement relations were transformed into stress–strain curves and compared with the experimental tensile curve [4] (Figure 10b). The simulation results, based on previously identified material parameters and maximum overlapping (50%) compared with the experimental tensile curve, show the increase of the free-standing $Ti_3C_2T_z$ film strength, stiffness, and failure strain when the overlapping is increased.

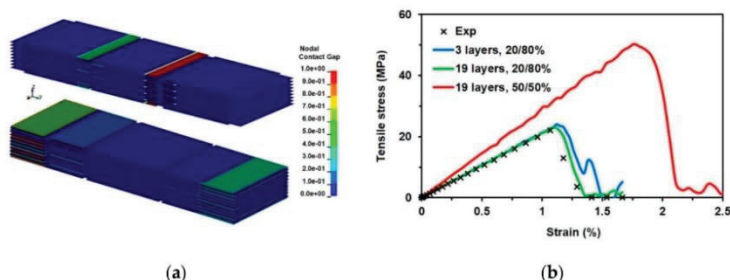


Figure 10. FE simulation results: (a) Tiebreak contact gap development episode in cases of 20%/80% and 50%/50% overlap; (b) tensile stress–strain curves of different thicknesses for free-standing MXene films; the experimental results are recalculated from the literature [4].

It is clearly seen (Figure 10b, red curve) that the random overlapping of nanosheets decreases the strength and stiffness of films assembled from free-standing MXene nanosheets. The FE models with curve fitting approaches can be used for material constants and adhesion energy identification, and only a proper statistical interpretation of the geometrical parameters of the nanosheets is needed.

4. Conclusions

The explicit FE model was developed in LS-Dyna to simulate the nanoindentation process of the 2D $Ti_3C_2T_z$ MXene monolayer flake and validate the material model. Sensitivity analysis of

Young's modulus and the flake thickness was performed. The obtained force versus deflection curves showed lower results than the experimental ones. To achieve similar results to the experimental ones, the thickness of the MXene flake should be increased from 0.98 up to 1.1 nm, or the Young's modulus should be increased from 333 up to 380 GPa.

The reverse engineering method with the curve fitting approach was applied to evaluate the adhesive strength of the assembled free-standing $\text{Ti}_3\text{C}_2\text{T}_x$ -based films. The interlaminar shear strength, stiffness, and energy release rate were selected as the main variables; these variables affect the tensile strength of the assembled free-standing $\text{Ti}_3\text{C}_2\text{T}_x$ -based film. The experimental tensile test data has been used for the curve fitting approach. A simulation was performed using three and nineteen layers of single-layered nanosheets with 20% overlap. The best fitted FE curve was obtained using an interlaminar shear strength $\tau_{\text{interl}} = 2.2 \text{ MPa}$, in-plane stiffness $E_{\text{interl}} = 0.26 \frac{\text{GPa}}{\mu\text{m}}$, and shear energy release rate $G_{\text{IIC}} = 3.8 \cdot 10^{-2} \frac{\text{J}}{\text{m}^2}$. The results of the sensitivity analysis showed that the largest influences on the behavior of tensioned film of free-standing MXene nanosheets are interlaminar shear strength and in-plane stiffness, while the shear energy release rate mainly affects the interlaminar damage properties of nanosheets. The simulation results based on identified material parameters showed an increase in the free-standing $\text{Ti}_3\text{C}_2\text{T}_x$ film strength, stiffness, and failure strain when the overlapping was increased by 50%.

The developed FE models with curve fitting approaches are of general purpose and can be used to determine material strength and stiffness properties and adhesion energy identification in different cases; however, a proper statistical interpretation of the single-layered nanosheet geometrical parameters is needed.

The obtained values of interlaminar shear strength, stiffness, and energy release rate in MXene are very important parameters for further investigation of MXene-polymer composites by finite element modeling. Areas for further research include analysis of the influence of multilayered or agglomerated nanosheets on the composite properties as well as development of MXene-polymer coatings with high-density MXene-MXene interactions.

Author Contributions: Conceptualization, D.Z. and P.G.; methodology, P.G. and G.M.; software, P.G.; validation, P.G.; formal analysis, D.Z., P.G., and A.A.; investigation, D.Z. and P.G.; resources, D.Z., P.G., and A.A.; data curation, P.G. and G.M.; writing—Original draft preparation, D.Z. and P.G.; writing—Review and editing, D.Z., P.G., G.M., and A.A.; visualization, D.Z.; supervision, D.Z.; project administration, D.Z. and A.A.; funding acquisition, D.Z. and A.A. All authors have read and agreed to the published version of the manuscript.

Funding: This project has received funding from the European Union's Horizon 2020 research and innovation programme under the Marie Skłodowska-Curie grant agreement No 777810.

Conflicts of Interest: The authors declare no conflict of interest.

References

1. Naguib, M.; Kurtoglu, M.; Presser, V.; Lu, J.; Niu, J.; Heon, M.; Hultman, L.; Gogotsi, Y.; Barsoum, M.W. Two-dimensional nanocrystals produced by exfoliation of Ti_3AlC_2 . *Adv. Mater.* **2011**, *23*, 4248–4253. [[CrossRef](#)] [[PubMed](#)]
2. Naguib, M.; Mochalin, V.N.; Barsoum, M.W.; Gogotsi, Y. 25th anniversary article: MXenes: A new family of two-dimensional materials. *Adv. Mater.* **2014**, *26*, 992–1005. [[CrossRef](#)] [[PubMed](#)]
3. Ronchi, R.M.; Arantes, J.T.; Santos, S.F. Synthesis, structure, properties and applications of MXenes: Current status and perspectives. *Ceram. Int.* **2019**, *45*, 18167–18188. [[CrossRef](#)]
4. Ling, Z.; Ren, C.E.; Zhao, M.-Q.; Yang, J.; Giammarco, J.M.; Qiu, J.; Barsoum, M.W.; Gogotsi, Y. Flexible and conductive MXene films and nanocomposites with high capacitance. *Proc. Natl. Acad. Sci. USA* **2014**, *111*, 16676–16681. [[CrossRef](#)] [[PubMed](#)]
5. Anasori, B.; Lukatskaya, M.R.; Gogotsi, Y. 2D metal carbides and nitrides (MXenes) for energy storage. *Nat. Rev. Mater.* **2017**, *2*, 1609. [[CrossRef](#)]
6. Ghidui, M.; Lukatskaya, M.; Zhao, M.; Gogotsi, Y.; Barsoum, M. Conductive two-dimensional titanium carbide 'clay' with high volumetric capacitance. *Nature* **2015**, *516*, 78–81. [[CrossRef](#)]

7. Borysiuk, V.N.; Mochalin, V.N.; Gogotsi, Y. Molecular dynamic study of the mechanical properties of two-dimensional titanium carbides $Ti_{n+1}C_n$ (MXenes). *Nanotechnology* **2015**, *26*, 1–10. [[CrossRef](#)]
8. Lipatov, A.; Lu, H.; Alhabet, M.; Anasori, B.; Gruverman, A.; Gogotsi, Y.; Sinitskii, A. Elastic properties of 2D $Ti_3C_2T_x$ MXene monolayers and bilayers. *Sci. Adv.* **2018**, *4*, 1–7. [[CrossRef](#)]
9. Borysiuk, V.N.; Mochalin, V.N.; Gogotsi, Y. Bending rigidity of two-dimensional titanium carbide (MXene) nanoribbons: A molecular dynamics study. *Comput. Mater. Sci.* **2018**, *143*, 418–424. [[CrossRef](#)]
10. Guo, Z.; Zhou, J.; Si, C.; Sun, Z. Flexible two-dimensional $Ti_n + 1C_n$ ($n = 1, 2$ and 3) and their functionalised MXenes predicted by density functional theories. *Phys. Chem.* **2015**, *17*, 15348–15354.
11. Zhao, M.Q.; Ren, C.E.; Ling, Z.; Lukatskaya, M.R.; Zhang, C.; Van Aken, K.L.; Barsoum, M.W.; Gogotsi, Y. Flexible MXene/carbon nanotube composite paper with high volumetric capacitance. *Adv. Mater.* **2015**, *27*, 339–345. [[CrossRef](#)]
12. Kilikevičius, S.; Kvietaikaitė, S.; Žukienė, K.; Omastová, M.; Aniskevich, A.; Zeleniakienė, D. Numerical investigation of the mechanical properties of a novel hybrid polymer composite reinforced with graphene and MXene nanosheets. *Comput. Mater. Sci.* **2020**, *174*, 109497. [[CrossRef](#)]
13. Monastyracki, G.; Mishnaevsky, L., Jr.; Hatter, C.B.; Aniskevich, A.; Gogotsi, Y.; Zeleniakienė, D. Micromechanical modeling of MXene-polymer composites. *Carbon* **2020**, *162*, 402–409. [[CrossRef](#)]
14. Shearer, C.J.; Slattery, A.D.; Stapleton, A.J.; Shapter, J.G.; Gibson, C.T. Accurate thickness measurement of graphene. *Nanotechnology* **2016**, *27*, 125704. [[CrossRef](#)]
15. Fu, Z.H.; Zhang, Q.F.; Legut, D.; Si, C.; Germann, T.C.; Lookman, T.; Du, S.Y.; Francisco, J.S.; Zhang, R.F. Stabilization and strengthening effects of functional groups in two-dimensional titanium carbide. *Phys. Chem.* **2016**, *94*, 104103. [[CrossRef](#)]
16. Jang, J.; Suhr, J.; Gibson, R.F. Combined numerical/experimental investigation of particle diameter and interphase effects on coefficient of thermal expansion and Young's modulus of SiO_2 /epoxy nanocomposites. *Polym. Compos.* **2012**, *33*, 1415–1423. [[CrossRef](#)]
17. Zhang, H.; Fu, Z.H.; Legut, D.; Germann, T.C.; Zhang, R.F. Stacking stability and sliding mechanism in weakly bonded 2D transition metal carbides by van der Waals force. *RSC Adv.* **2017**, *7*, 55912–55919. [[CrossRef](#)]
18. Jiang, T.; Zhu, Y. Measuring graphene adhesion using atomic force microscopy with a microsphere tip. *Nanoscale* **2015**, *7*, 10760–10766. [[CrossRef](#)] [[PubMed](#)]
19. Burnham, N.A.; Dominguez, D.D.; Mowery, R.L.; Colton, R.J. Probing the surface forces of monolayer films with an atomic-force microscope. *Phys. Rev. Lett.* **1990**, *64*, 1931–1934. [[CrossRef](#)] [[PubMed](#)]
20. Cappella, B.; Kapp, M. Force measurements with the atomic force microscope: Technique, interpretation and applications. *Surf. Sci. Rep.* **2005**, *59*, 1–152.
21. Li, Y.; Huang, S.; Wei, C.; Wu, C.; Mochalin, V.N. Adhesion of two-dimensional titanium carbides (MXenes) and graphene to silicon. *Nat. Commun.* **2019**, *10*, 3014. [[CrossRef](#)] [[PubMed](#)]
22. Mashtalir, O.; Naguib, M.; Mochalin, V.N.; Dall'Agnese, Y.; Heon, M.; Barsoum, M.W.; Gogotsi, Y. Intercalation and delamination of layered carbides and carbonitrides. *Nat. Commun.* **2013**, *4*, 1–7. [[CrossRef](#)] [[PubMed](#)]
23. Jastrzębska, A.M.; Karwowska, E.; Wojciechowski, T.; Ziemkowska, W.; Rozmysłowska, A.; Chlubny, L.; Olszyna, A. The atomic structure of Ti_2C and Ti_3C_2 MXenes is responsible for their antibacterial activity toward *E. coli* bacteria. *J. Mater. Eng. Perform.* **2019**, *28*, 1272–1277. [[CrossRef](#)]
24. Wang, H.; Zhang, J.; Wu, Y.; Huang, H.; Li, G.; Zhang, X.; Wang, Z. Applied Surface Science Surface modified MXene Ti_3C_2 multilayers by aryl diazonium salts leading to large-scale delamination. *Appl. Surf. Sci.* **2016**, *384*, 287–293. [[CrossRef](#)]
25. Chen, L.; Shi, X.; Yu, N.; Zhang, X.; Du, X. Measurement and analysis of thermal conductivity of $Ti_3C_2T_x$ MXene films. *Materials* **2018**, *11*, 1701. [[CrossRef](#)]
26. *LS-DYNA Keyword User's Manual*; Livermore Software Technology Corporation (LSTC): Livermore, CA, USA, 2014; Volume II, pp. 1–1265.



Article

Strain Sensing Coatings for Large Composite Structures Based on 2D MXene Nanoparticles

Gediminas Monastyreckis ¹ , Anastasiia Stepura ², Yaryna Soyka ², Hanna Maltanova ³ , Sergey K. Poznyak ³ , Mária Omastová ² , Andrey Aniskevich ⁴  and Daiva Zeleniakiene ^{1,*} 

¹ Department of Mechanical Engineering, Kaunas University of Technology, Studentu St. 56, 51424 Kaunas, Lithuania; gediminas.monastyreckis@ktu.edu

² Polymer Institute, Slovak Academy of Sciences, Dúbravská cesta 9, 845 41 Bratislava, Slovakia; anastasiia.stepura@savba.sk (A.S.); upolyaso@savba.sk (Y.S.); maria.omastova@savba.sk (M.O.)

³ Research Institute for Physical Chemical Problems, Belarusian State University, 220030 Minsk, Belarus; maltanova@bsu.by (H.M.); poznyak@bsu.by (S.K.P.)

⁴ Institute for Mechanics of Materials, University of Latvia, Jelgavas str. 3, LV-1004 Riga, Latvia; andrey.aniskevich@pmi.lv

* Correspondence: daiva.zeleniakiene@ktu.lt

Abstract: Real-time strain monitoring of large composite structures such as wind turbine blades requires scalable, easily processable and lightweight sensors. In this study, a new type of strain-sensing coating based on 2D MXene nanoparticles was developed. A $Ti_3C_2T_x$ MXene was prepared from Ti_3AlC_2 MAX phase using hydrochloric acid and lithium fluoride etching. Epoxy and glass fibre-reinforced composites were spray-coated using an MXene water solution. The morphology of the MXenes and the roughness of the substrate were characterised using optical microscopy and scanning electron microscopy. MXene coatings were first investigated under various ambient conditions. The coating experienced no significant change in electrical resistance due to temperature variation but was responsive to the 301–365 nm UV spectrum. In addition, the coating adhesion properties, electrical resistance stability over time and sensitivity to roughness were also analysed in this study. The electromechanical response of the MXene coating was investigated under tensile loading and cyclic loading conditions. The gauge factor at a strain of 4% was 10.88. After 21,650 loading cycles, the MXene coating experienced a 16.25% increase in permanent resistance, but the response to loading was more stable. This work provides novel findings on electrical resistance sensitivity to roughness and electromechanical behaviour under cyclic loading, necessary for further development of MXene-based nanocoatings. The advantages of MXene coatings for large composite structures are processability, scalability, lightweight and adhesion properties.

Keywords: MXenes; coatings; strain sensors; electrical properties; cyclic loading



Citation: Monastyreckis, G.; Stepura, A.; Soyka, Y.; Maltanova, H.; Poznyak, S.K.; Omastová, M.; Aniskevich, A.; Zeleniakiene, D. Strain Sensing Coatings for Large Composite Structures Based on 2D MXene Nanoparticles. *Sensors* **2021**, *21*, 2378. <https://doi.org/10.3390/s21072378>

Academic Editor: Nandika Anne D'Souza

Received: 13 March 2021

Accepted: 26 March 2021

Published: 29 March 2021

Publisher's Note: MDPI stays neutral with regard to jurisdictional claims in published maps and institutional affiliations.



Copyright: © 2021 by the authors. Licensee MDPI, Basel, Switzerland. This article is an open access article distributed under the terms and conditions of the Creative Commons Attribution (CC BY) license (<https://creativecommons.org/licenses/by/4.0/>).

1. Introduction

In the past decade, the demand for nanosensors and electrically conductive polymer composites has grown considerably [1,2]. The tunability of properties based on nanoparticle materials and their mixtures can meet the requirements for various electronic devices and sensors. Currently, one of the largest known 2D nanoparticle families is the MXenes [3,4]. The most studied MXene particle is the titanium carbide $Ti_3C_2T_x$, which has shown excellent mechanical and electrical properties (both in pristine form and in polymer composites) from nanoindentation measurements [5], molecular dynamics simulations [6], and finite element simulations [7,8]. Despite the relatively low van der Waals forces between 2D nanoflakes [9], pure MXene films have shown very high tensile strengths (590 MPa for a 980 nm thick film), which was obtained using large-diameter aligned flakes and the blade-casting method [10]. These properties can be influenced by different delamination methods [11,12]. During the etching and delamination process, the flake size and thickness

of MXene particles can differentiate [13]. In addition, surface functional groups (T_z), such as $-O$, $-OH$, and $-F$ [14] (which are responsible for adhesion and wettability properties), can be modified during the process. Experimental research and finite element modelling have shown that MXenes adhere to epoxies and polymers [15–17]. Easily processable and scalable methods, such as spray coating [18], vacuum filtration [19], 3D printing [20] and casting [10], have shown that MXenes are also very attractive nanoparticles for coatings and thin-film applications. MXenes have already been investigated and have revealed good results for Li-ion batteries [21], organic solar cells [22], electromagnetic interference shielding [23] and supercapacitors [24].

The unique multilayered and porous structure of MXene films can cause a highly sensitive response to deformation and morphology changes. Owing to the molecular intercalation between the nanolayers, MXene films behave as very sensitive multi-gas sensors [25] and humidity sensors [26]. Furthermore, MXene aerogel foams and other layered polymer nanocomposites can be used as ultra-sensitive pressure sensors with detection limits of up to 100 Pa [27]. Sandwich-type nanolaminates and nanosensors developed from a mixture of 2D nanoflakes, nanowires, and nanospheres [28–30] have shown a very wide strain-sensing range owing to their enhanced electrical conductivity and flake-to-flake sliding ability. One of the most sensitive strain sensors was obtained using MXene-intercalated textile yarns. Knittable and washable MXene-coated yarns have been shown to have ultra-sensitive strain responses with a gauge factor ($GF_{152\%}$ at a strain of 152%) of up to 12,900 [31]. Another study was performed with MXene-silver nanowire coatings under tensile loading [28], where the $GF_{5\%}$ reached approximately 10. The same experiment was performed with graphene-silver nanowire coatings, where $GF_{5\%}$ reached only 2.5 [32]. Meanwhile, carbon nanotube (CNT) modified polymers [33] possessed much lower strain sensing capability, where $GF_{5\%}$ varied between 0.1 and 0.25.

The electromechanical mechanism of nanoparticle-based strain sensors is well explained by an analytical approach [34]. Surface topography images also provide in-depth details on how the structure of the nanocoating behaves under a wide range of deformations (0–60%) [32]. It was also found that the electrical sensitivity was enhanced by electron tunnelling effects [35], which mostly occur when the distance between the nanoparticles is less than 3 nm. An analytical approach describing the tunnelling effect explains how electric resistance can change under nanoscale deformations [36].

Traditional sensors, such as strain gauges, accelerometers, piezoelectric transducers, and fibre optic cables, have been used for wind turbine monitoring [37]. These sensors typically experience adhesion problems and application difficulties, requiring precise sensor calibration and complex signal processing [38]. Despite this, fibre Bragg grating (FBG) optical sensors are widely used due to their most accurate strain measurements. FBG sensors are still being improved by materials such as magnetostrictive Terfenol-D ($Tb_{0.3}Dy_{0.7}Fe_{1.92}$), with whom the sensitivity of the system is improved by a factor of 4 [39].

Until now, MXenes have not been investigated as strain-sensing coatings for fibre-reinforced polymer composites. The aim of this study is to develop an easily processable and scalable MXene coating that can detect the low strain values typical for fibre-reinforced composites. The main tasks were to characterise the morphology and uniformity of the coating, investigate the response to environmental conditions (such as temperature and UV irradiation), analyse the surface roughness influence on sensing performance and study the sensing behaviour under tensile loading and cyclic loading conditions. The strain sensing ability of the MXene coating was based on the change in electrical resistance. Simple spray-coating methods and electrical resistance monitoring systems were a priority during the experiments.

2. Materials and Methods

2.1. Materials

$Ti_3C_2T_z$ MXenes were prepared from Ti_3AlC_2 MAX phase with a particle size of $<40\ \mu m$ and purity of 98 wt.% (MRC, Kiev, Ukraine) using a previously documented

method [12]. The etching solvents used were hydrochloric acid (37 wt.%, Merck, Darmstadt, Germany) and lithium fluoride (>99 wt.%, Sigma Aldrich, Munich, Germany). LiF was mixed with HCl to generate HF in the system. The MAX phase was slowly added and stirred for 24 h. The multilayer MXene sediment was further delaminated using 99 wt.% LiCl (Sigma Aldrich, Munich, Germany). The resulting solution was centrifuged 10–15 times at 3500 rpm and washed with deionised water until the pH of the supernatant reached 6.5. The concentration of the delaminated MXenes in the supernatant was 0.335 mg/mL, but it was further centrifuged until the concentration reached 3.3 mg/mL to be more suitable for the spraying process.

The thermosetting epoxy resin Bisphenol F-epichlorohydrin (Biresin[®] CR122, Sika AG, Baar, Switzerland) and an amine curing agent (Biresin[®] CH122-5) were mixed at a ratio of 10:3. Epoxy tensile specimens (ISO-527-2-5A) were cast in silicone moulds. Glass fibre-reinforced polymer (GFRP) tensile specimens and sandwich-type GFRP specimens were prepared for adhesion tests by hand-layup and vacuum bagging methods. GFRP tensile specimens (15 cm × 1.5 cm) were made of 5 plies of twill-weave 2/2 (163 g/m²) Interglas 92110 (Porcher Industries, Erbach, Germany), and adhesion specimens (14 cm × 2.5 cm) were made of a total of 8 plies and 4 mm thick AIREX C70.75 foam (Airex AG, Sins, Switzerland). All specimens were cured at room temperature for 24 h and post-cured in a convection oven for 5 h at 100 °C. Additionally, epoxy samples were roughened in the Y direction (parallel to loading), X direction (perpendicular to loading), and YX direction (roughened in both directions) using P280 sandpaper (52.2 µm average particle diameter). All samples were plasma-treated and spray-coated with a water-based MXene solution, as described below.

2.2. Preparation of MXene Coating

To enhance the adhesion between the epoxy substrate and MXenes, a surface plasma treatment was performed using a Zepto Diener low-pressure plasma cleaner (Diener Electronic GmbH & Co. KG, Ebhausen, Germany) and a K1050X RF plasma cleaner (Quorum Technologies, Laughton, UK). The samples were treated under vacuum with no additional gases for 3 min with 100 W power at 40 kHz frequency. The water contact angle was reduced from 68.7° (for pristine epoxy) to 25.3° (for the modified epoxy surface). Another treatment was performed in a vacuum with an oxygen and argon enriched atmosphere for 3 min with 100 W at 13.56 MHz. The contact angle was reduced to 20.1°. After the epoxy surface plasma treatment, water-based MXenes were sprayed using a Sparmax HB-040 airbrush with a 0.4 mm diameter nozzle and a Sparmax DC-25X 2.07 bar compressor with 0.1 mL/s paint yield (Anest Iwata Sparmax Co., Taipei, Taiwan). The MXene coating was applied by spraying for 10 s at a distance of 15 cm, which naturally dried over 5–10 s at room temperature. Copper wires were directly soldered onto the MXene films using the commercially available electrically conductive polymer Protospasta (Protoplant, Inc., Vancouver, WA, USA). This polymer is made from a mixture of polylactic acid (PLA) (4043D PLA, Natureworks, Minnetonka, MN, USA) and carbon black (CB). The volume resistivity of the polymer is 30 Ωcm, and the melting point is 155 °C. The soldering needle temperatures were set to 200 °C, similar to the 3D printer nozzle temperatures. The soldered wires were additionally covered with a thin layer of silver paste. The distance between the silver paste contacts for both the epoxy and GFRP samples was 30 mm. The epoxy specimen sprayed with MXenes and a monitoring system (described in Section 2.3) are presented in Figure 1.

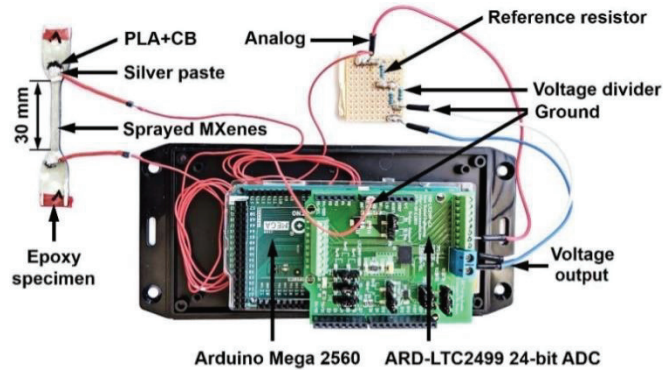


Figure 1. MXene-coated epoxy specimen and electrical resistance measurement system.

2.3. Characterisation and Testing Equipment

X-ray photoelectron spectroscopy characterisation of the same Ti_3AlC_2 MAX phase and $\text{Ti}_3\text{C}_2\text{T}_z$ MXenes was previously reported by Zukiene et al. [16]. The thickness and topography of the MXene coatings were characterised using scanning electron microscopy (SEM) (JEOL JSM 6610, JEOL Ltd., Tokyo, Japan). Gold-coated samples were measured under high-vacuum mode with an accelerating voltage of 15 kV.

The homogeneity of the MXene coating after plasma treatment and the roughness of the substrate were investigated using a Leica DVM6 optical microscope (Leica Microsystems, Wetzlar, Germany). 3D optical topographical scanning was performed using the image rendering software LAS X (Leica Microsystems), based on the stacking of 2D images in the Z direction.

Tensile and fatigue tests were performed using Tinius Olsen H25 KT (Tinius Olsen, Salfords, UK) and Instron ElectroPuls E10000T (Instron, Norwood, MA, USA) equipment, respectively. Deformations in the longitudinal direction between four strain markings (2.5 cm distance) and transversal deformations between six strain markings (4 mm distance), were measured using Manta G-146B visual extensometer (Allied Vision Technologies, Stadtroda, Germany). Peeling on epoxy samples (5 cm \times 0.5 cm) covered with the MXene coating was investigated using simple household adhesive tape. Pull-out tests of MXene-coated sandwich-type GFRP specimens were performed using an Adheometr PM 420/63 under ISO-4624 standards. For the UV light absorbance experiment, a UV DRT230 lamp with a 301–365 nm emission wavelength and a surface power density of 3–7 mW/cm² was used. Experiments were performed on an MXene-coated sandwich-type GFRP specimen (13.5 cm \times 2.5 cm). The response of the MXene coating to direct sunlight was measured under a clear sky with a solar elevation angle of 54° (Riga, Latvia).

The temperature and initial electrical resistance values were monitored using a Fluke 287 True-RMS logging multimeter (Fluke Corporation, Everett, WA, USA). The temperature of MXenes was measured using a temperature probe soldered to aluminium foil (0.3 mm \times 25 \times 30 mm), which was pressed to a 0.2 mm thick protective epoxy layer on top of the MXene coating. An MXene coating area of the same size (25 mm \times 30 mm) was heated with 10–90 V (DC) using AX-12001DBL external power supply (Transfer Multisort Elektronik, Łódź, Poland). For the tensile-tensile fatigue tests, electrical resistance values were measured using Arduino Mega 2560 microcontroller (Figure 1) and ATmega2560 microchip (Arduino, Turin, Italy). Additionally, a 24-bit analogue-to-digital converter (ARD-LTC2499, Iowa Scaled Engineering, Elbert, CO, USA) with a precise 4.096 V output voltage and 7 Hz measurement frequency was used for high-accuracy electrical resistance

measurements. The electrical resistance monitoring during mechanical loading was based on the voltage difference between a single reference resistor and the MXene coating.

3. Results

3.1. MXene Coating Topography

The morphology of the MXene flakes and the coating was studied using SEM. The average thickness of the coating was approximately 1 μm , as evident in the cross-sectional view of the fractured epoxy sample presented in Figure 2a. A plasma-treated smooth epoxy sample coated with MXenes is presented in Figure 2b (top view). A $\text{Ti}_3\text{C}_2\text{T}_z$ flake with a size of $20\ \mu\text{m} \times 10\ \mu\text{m}$ can be seen, while sizes, ranging from 1 to 5 μm are the most common, as it was reported in previous SEM analysis [16]. The MXene-coated GFRP sample is shown in Figure 2c (top view), in which glass fibre filament markings and MXene flake edges can be seen.

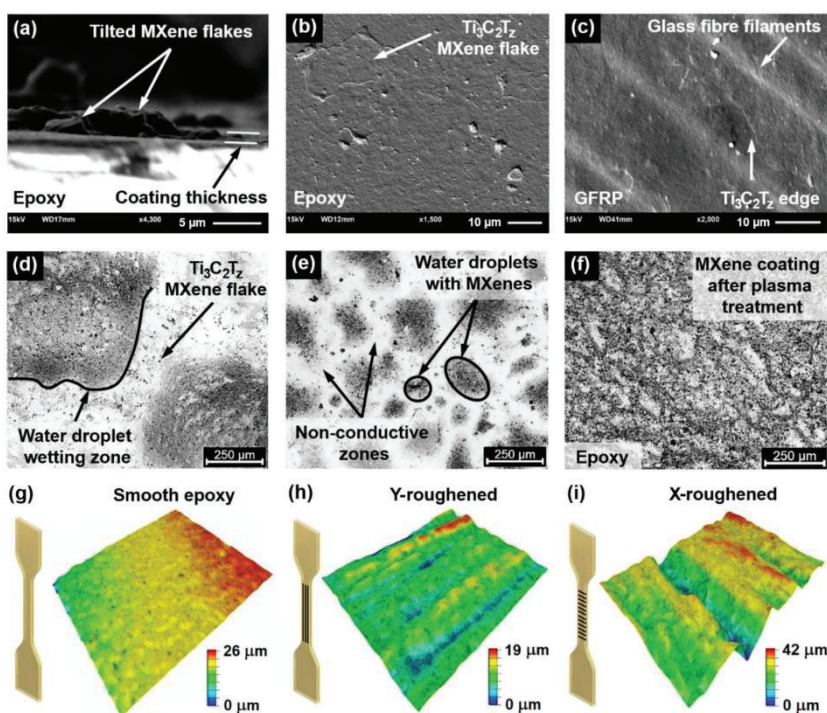


Figure 2. Scanning electron microscopy images of the sprayed MXenes: (a) thickness of the coating; (b) topography of MXenes on epoxy, and (c) glass fibre–reinforced polymer samples. Optical microscopy images of the MXene coatings: (d) sprayed for 2 s at 3 cm; (e) sprayed for 10 s at 15 cm; and (f) sprayed for 10 s at 15 cm on a plasma-treated epoxy sample. Optical topography images of epoxy samples that were (g) smooth, (h) roughened in the Y direction, and (i) roughened in the X direction.

Owing to the optical transparency of the epoxy and MXenes [40], the overall quality of the coating was analysed using an optical microscope with an external light source. First, small water droplets containing higher (darker areas) and lower (lighter areas) concentrations of MXene flakes were observed in optical microscopy images (Figure 2d).

The primary reason for this effect was the hydrophobic epoxy surface. In addition, the size of these droplets and coating uniformity depended on the spraying time and nozzle distance. For example, when sprayed for 2 s at 3 cm from the surface, water droplets were 250–500 μm in size (Figure 2d), while spraying for 10 s at 15 cm reduced the droplet size to 50–250 μm (Figure 2e). Plasma treatment was performed to enhance the hydrophilic properties of the epoxy surface, which increased the conductivity and uniformity of the coating (Figure 2f). The sensitivity of strain sensors based on nanoparticles depends on the morphology of the substrate surface [41]. To investigate this effect, epoxy tensile specimens were roughened in the Y, X, and YX directions. 3D optical topography images (600 $\mu\text{m} \times 450 \mu\text{m}$) are presented in Figure 2g–i, and detailed average roughness values are presented in Section 3.4.

3.2. MXene Coating Adhesion and Stability

The adhesion to epoxy and the stability of the MXene coatings were investigated using SEM images and electrical resistance changes during every peel-off attempt with adhesive tape. An SEM image of the sample before peeling is presented in Figure 3a, where an MXene coating with small fragments can be seen. After the first peel-off, the surface of the MXene coating became smooth and no fragments, rupture spots, or debonding from the epoxy was observed (Figure 3b). However, the relative electrical resistance increased with every peel-off attempt (Figure 3c). After the first peel-off, the relative resistance increased 3.2 times, and it increased 8.6 times after the fifth. After five peeling attempts, no damage to the coating was observed, which suggests that adhesion between the MXenes and the epoxy was strong, as mentioned in several previous studies [15–17]. To extend the adhesion experiments, an MXene coating pull-out test was performed (Figure 3d). The $\text{Ti}_3\text{C}_2\text{T}_z$ water solution was sprayed on a more rigid sandwich-type GFRP composite. In total, six pull-out attempts were performed on two GFRP specimens, and an average pull-out stress of 2.14 MPa was obtained. Despite the pull-out, the inner area retained MXene flakes, whose electrical resistance increased roughly 19 times compared to the initial values (Figure 3d). Therefore, the actual pull-out stress (2.14 MPa) was obtained between MXene-MXene flakes in the perpendicular direction. This stress is roughly 10 times lower than the tensile strength of pure MXene-MXene films [42,43]. These results are very important for the further development of strain sensing MXene coatings.

Coatings based on $\text{Ti}_3\text{C}_2\text{T}_z$ MXenes tend to degrade by their oxidation to TiO_2 in various exploitation conditions [44]. In this article, the MXene coating stability was investigated over a four-week period at room temperature (Figure 3e). The relative electrical resistance over four weeks of a sample peeled one time was 2.49, while that of a non-peeled sample was 3.80. This suggests that a coating with a smoother surface will oxidise slower owing to the smaller nanoparticle area exposed to air. The best electrical resistance stability of the MXene coatings was achieved with a protective epoxy layer. In comparison, the electrical resistance of the sample without a covering layer increased the fastest, and the resistance after four weeks was 3.7 times higher than that of the covered sample. Such oxidation rates of MXenes do not satisfy application requirements for sensors, where on the contrary, MAX phase-based sensors show long-term stability [45]. Therefore, the focus still remains on the development of new oxidation preventing methods such as hydrogen annealing [46] and L-ascorbic acid treatment [47], which have already shown positive effects.

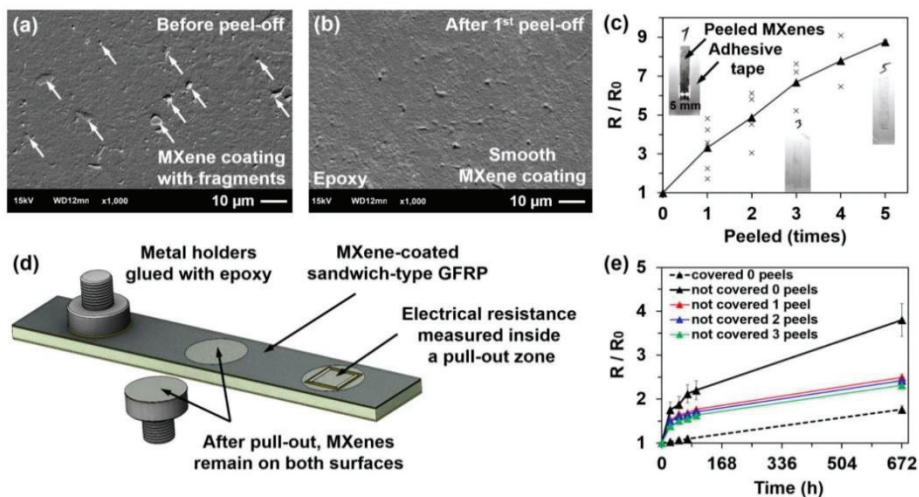


Figure 3. Scanning electron microscopy images of the MXene coating (a) before peeling and (b) after the first peel-off attempt; (c) electrical resistance change during five peel-off attempts; (d) MXene coating pull-out test; and (e) electrical resistance change over a 4 week period.

3.3. MXene Coating UV and Temperature Response

Experiments were performed to understand deviations in the electrical signal from the MXene coatings due to ambient conditions, such as direct sunlight and temperature. Several studies have shown that MXene films can experience high heating temperatures (114 °C) under an applied voltage of 6 V [48]. In this study, coating temperatures under 10–90 V were investigated. When 10 V was applied, the temperature of the MXenes only increased from 24 to 27 °C (Figure 4a) owing to the high resistance of the coating (0.91 kΩ). In comparison, at 50 V, the coating temperature increased to 103.8 °C, and at 90 V, the coating temperatures plateaued at 183.7 °C, which is close to the epoxy melting temperature. Detailed results of the temperature response under different voltages are presented in Figure 4a. The electrical resistance was measured after 50 V was applied and then removed, and the coating cooled naturally from 103.8 to 35.6 °C over 300 s (Figure 4b). During this process, the electrical resistance decreased to 0.8%. The electric current was also monitored during the heating process with an applied voltage (Figure 4c). When the temperature of the coating reached 156 °C (70 V), the resistance of the coating began to increase, and the electric current dropped. This occurred because of the softened epoxy surface, which resulted in a change in the morphology and a rearrangement of the MXene flakes. In addition, no degradation of $Ti_3C_2T_z$ could occur, according to previous thermogravimetric analysis [49], which shows that the MXene is thermally stable and loses only 4–7% of its weight at 700 °C.

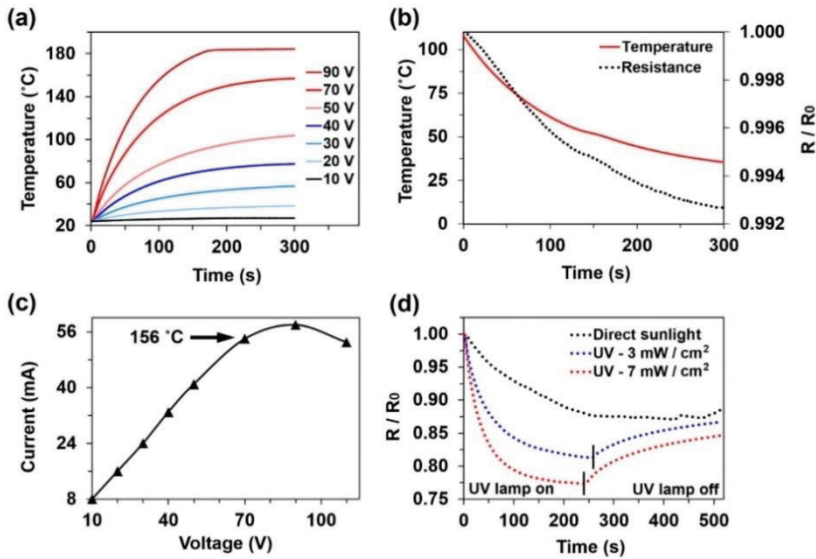


Figure 4. (a) Increase in the MXene coating temperature under different applied voltages; (b) change in the electrical resistance during the natural cooling process of the sample; (c) response of the electric current to applied voltage; and (d) relative electrical resistance response of the MXene coating to direct sunlight and UV irradiation.

As described in several articles [50], MXene and other nanoparticles, such as graphene, exhibit high absorbance in the 200–400 nm UV spectrum. Therefore, the electrical resistance response of the MXene coating to direct sunlight was measured. After 5 min under direct sunlight, the electrical resistance of the coating decreased by 12.5% (Figure 4d). Depending on the UV lamp irradiance intensity, the response of the coating reached a steady state after 4 min, and the electrical resistance decreased by 22.7% at 7 mW/cm² (35 °C specimen temperature). These results are important because they help to avoid electrical signal disturbance due to ambient conditions. Therefore, tensile and fatigue tests were performed without daylight, and the temperatures of the samples were monitored during the testing.

3.4. Tensile Tests of MXene-Coated Epoxy Specimens

In this experiment, the electromechanical behaviour of MXene coatings under tensile loading was monitored on smooth and roughened epoxy samples. The average roughness values in the X and Y directions, initial resistance values (R_0), resistance values at the sample breaking point (R_b), and gauge factors at strains of 1% ($GF_{1\%}$) and 4% ($GF_{4\%}$) of 4 samples with different roughness values (0, Y, X, and YX) are presented in Table 1.

Table 1. Electrical resistance response of the MXene coatings during tensile tests.

Roughening Direction	Average Roughness in X/Y Directions (μm)	R_0 (k Ω)	R_b (k Ω)	$GF_{1\%}$	$GF_{4\%}$
0	0.56	8.48	49.3	1.02	4.17
Y	0.68/2.31	48.3	1049	1.12	4.81
X	2.54/1.32	674	14924	1.29	10.88
YX	1.67/1.63	647	3604	1.08	5.01

The relative electrical resistance response of the MXene coatings to 5 initial loading cycles, with amplitudes of 10 to 50 MPa, are presented in Figure 5a. A considerable difference in initial resistance was obtained between the smooth and X-roughened samples (8.48 k Ω versus 674 k Ω , respectively). In addition, the X-roughened sample with a roughness of 2.54 μm had the highest GF_{1%} of 1.29, while the smooth sample with an average roughness of 0.56 μm showed only 1.02 (Figure 5b). Notable changes in the relative resistance curves for all the samples appeared between strains of 0.5% and 1.1% (Figure 5b). Previous research on pure MXene films under tensile conditions yielded similar fracture strain values, which are marked in the figure as MXene fracture points (FP): FP-1 [48], FP-2 [49], and FP-3 [42,43]. These results suggest that MXene flakes began to debond from one another as the resistance began to increase drastically. Another important comparison is presented in Figure 5c,d, which shows that the resistance behaviour on the smooth epoxy substrate was stable during cycling, while on the rough substrate, the values were more chaotic. These results help to understand the electrical signal response under different strain values as well as to illuminate how even a small difference in roughness can have a substantial impact on the coating sensitivity. For instance, MXene-silver nanowire coatings reached GF_{5%} of 10 [28], while in this research, depending on the roughness, GF_{4%} was obtained in the range of 4.17–10.88.

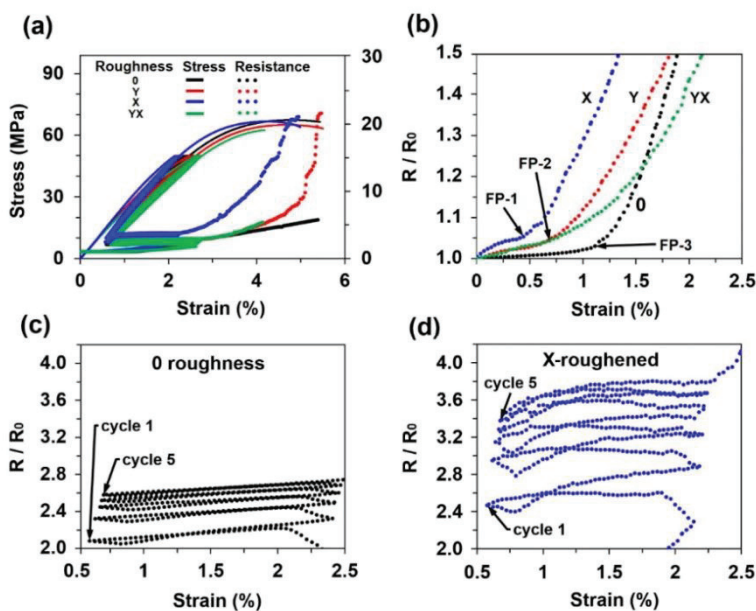


Figure 5. Results from tensile tests with five initial loading cycles on smooth and roughened MXene-coated epoxy samples: (a) mechanical response and relative electrical resistance measurements of four samples with different roughening; (b) magnified region showing the electrical resistance at low strains; and MXene resistance response under five loading cycles with 10–50 MPa amplitudes on (c) a smooth epoxy sample and (d) an X-roughened sample.

3.5. Fatigue Tests of MXene-Coated Epoxy Specimens

After the initial tensile tests, tensile-tensile fatigue tests were performed with smooth MXene-coated epoxy specimens. Loading cycles were performed in the elastic region of

the specimens at 0.5 Hz and an 8.33–25 MPa loading amplitude (0.31–0.97% strain). The specimen temperatures were monitored throughout the tests and were maintained at 25 °C. The change in electrical resistance over 21,650 cycles can be seen in Figure 6a. The electrical resistance amplitude (ΔR) at the beginning of the fatigue test can be seen in the magnified region showing the first 100 cycles (Figure 6b), where ΔR was approximately 2%. It is important to note that the electrical resistance permanently increased after every cycle, and after 21,650 loading cycles, the MXene coating experienced an irreversible resistance increase of 16.25%. The last 50 cycles are shown in Figure 6c, where ΔR decreased from 2% to 1%, which indicates that the coating became less sensitive. However, the important result was that the rate of increase of the irreversible resistance became much lower, i.e., the MXene coating electrical signal became more stable to mechanical loading. The results of the variation in the electrical resistance of the MXene coating over twenty-one thousand cycles under the same loading conditions are important for the development of signal processing algorithms and further coating improvements.

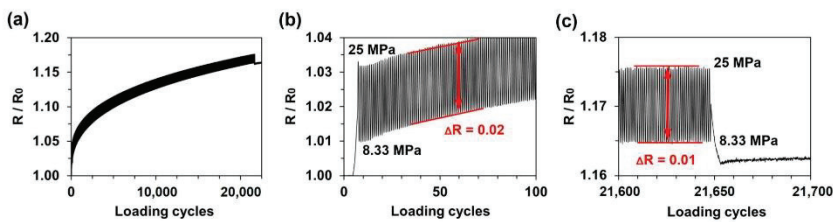


Figure 6. Fatigue test results of a smooth MXene-coated epoxy sample: (a) relative resistance during fatigue testing with an 8.33–25 MPa amplitude, and magnified regions showing (b) the first 100 cycles and (c) the last 50 cycles.

3.6. Fatigue Tests of MXene-Coated GFRP Specimens

The tensile-tensile fatigue response of the MXene coating was further investigated using 0° and 45° fibre angle GFRP specimens. The samples were first tested until fracture, and tensile strengths of 393.3 and 120.3 MPa and fracture strains of 2.86% and 6.98% were obtained for the 0° and 45° fibre specimens, respectively. The $GF_{2\%}$ of the 0° specimen was 1.72, and that of the 45° specimen was 1.08. The fatigue tests were performed at 0.5 Hz with a variable loading amplitude. Detailed loading properties are presented in Table 2 and labelled according to the loading steps (force, stress, and strain).

Table 2. Fatigue loading steps: loading amplitude, tensile stress, and tensile strain.

Loading Step	Loading Amplitude (kN)	Tensile Stress (MPa)	Tensile Strain (%)
0	0	0	0
1	0.25–1.25	33–165	0.21–1.07
2	0.50–1.50	66–198	0.42–1.33
3	0.75–1.75	99–231	0.63–1.59
4	1.00–2.00	132–264	0.85–1.86

The fatigue tests of the MXene-coated 0° and 45° fibre angle GFRP specimens showed similar strain sensing tendencies; therefore, only the results of the 0° specimen under different loading steps are presented in Figure 7a. In total, four loading step sequences (0-1-2-3-4-3-2-1-0) were applied. It can be observed that the MXene coating sensitivity to strain becomes more stable with repeated loading steps. First, the irreversible resistance increased at every loading step, but after several thousand cycles, the permanent resistance only increased during the fourth step, which had a high loading amplitude (Figure 7b). After four series of loading step sequences, the sample was loaded with low amplitude steps (1-2-1) (Figure 7c). During this stage, the strain sensing of the MXene coating was

stable, and it was possible to identify the exact tensile stress (and strain) according to the relative resistance values. A magnified region showing the electrical resistance is presented in Figure 7d. The accuracy obtained using only a single reference resistor scheme with no additional filtering or amplification of the signal demonstrate that the MXenes are strain-sensitive nanoparticles. Although, the resistance amplitude at small strain regions (0.21–1.07%) is not very high ($\Delta R = 2.7\%$), when compared to CNT intercalated MXene sensors ($\Delta R = 5.5\%$ at 0.2–1% strain) [29]. Pure MXene coatings can still be competitive due to their processability, scalability and good adhesion properties when compared to MXene-CNT nanocoatings.

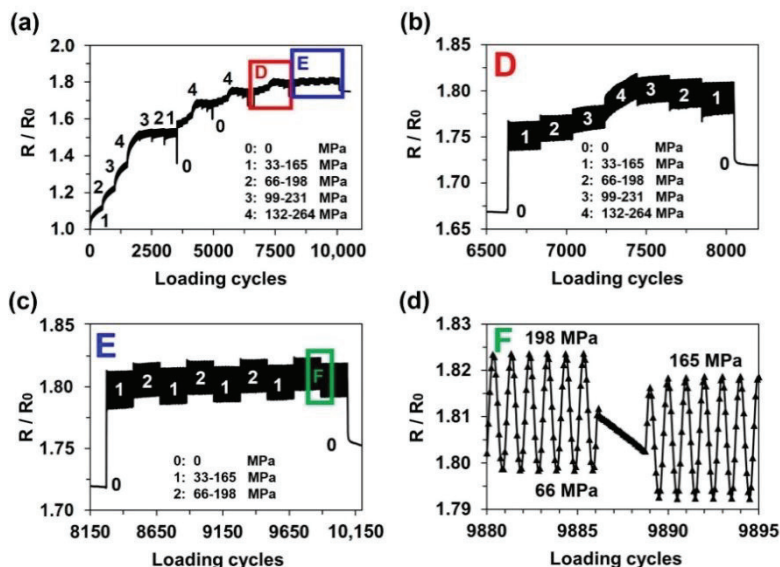


Figure 7. Fatigue test results for MXene-coated 0° glass fibre-reinforced polymer specimen: (a) relative electrical resistance response under 10000 loading cycles with varying amplitude; (b) magnified region showing the loading step series 0-1-2-3-4-3-2-1-0; (c) magnified region showing the loading step series 1-2-1; and (d) magnified region showing the loading step change from 2 to 1.

4. Conclusions

In this study, a comprehensive electromechanical investigation of MXene-coated epoxy and GFRP specimens was performed. $Ti_3C_2T_x$ was synthesised using HCl and LiF etching. A water-based MXene solution was sprayed onto plasma-treated epoxy and GFRP samples.

Before the tensile experiments, the response of MXene coatings to heating and UV irradiation was analysed. The MXene coating experienced no significant increase in electrical resistance until the epoxy substrate began to degrade at 156°C . After 5 min under direct sunlight, the coating resistance decreased by 12.5% and reached a plateau. Under 301–365 nm UV light, the resistance decreased by 22.7%.

To investigate the strain sensitivity behaviour of the MXene coating, epoxy samples were roughened in directions perpendicular and parallel to the tensile loading. The surface roughness was measured using 3D optical microscopy scanning, and the morphology of the MXenes was characterised using SEM. The MXene strain sensitivity was primarily

dependant on the perpendicular roughness, where the gauge factor at 4% strain was 10.88, while that of the parallel roughness was 4.81.

The increase in the electrical resistance of the MXene coatings over time, durability to peeling, and MXene adhesion to the epoxy surface was also studied. The pull-out stress obtained between MXene-MXene particles in the perpendicular direction was 2.14 MPa.

The main focus of this study was to investigate the electrical resistance response of MXene-coated epoxy and GFRP samples under tensile-tensile fatigue loading. After 21,650 loading cycles at a constant loading amplitude, the MXene coating on the epoxy experienced a 16.25% increase in permanent resistance. GFRP samples were tested under varying amplitudes with high tensile loads. After 10,000 cycles, the electrical resistance of the MXene coating permanently increased by 1.8 times, but the response to loading was more stable and equal to 2.7% resistance change at a strain region of 0.21–1.07%.

These results demonstrate that MXenes are a viable material for ultra-thin, scalable, and easily processed strain-sensing coatings for large fibre-reinforced composite structures.

Author Contributions: Conceptualisation, G.M., M.O., A.A. and D.Z.; methodology, G.M., A.S., Y.S., H.M., S.K.P., M.O., A.A. and D.Z.; software, G.M.; validation, G.M. and D.Z.; formal analysis, G.M., S.K.P. and D.Z.; investigation, G.M., A.S., Y.S., H.M., M.O., A.A. and D.Z.; resources, M.O., A.A. and D.Z.; data curation, G.M., A.S., Y.S. and H.M.; writing—original draft preparation, G.M.; writing—review and editing, A.S., Y.S., H.M., S.K.P., M.O., A.A. and D.Z.; visualisation, G.M., H.M. and D.Z.; supervision, S.K.P., M.O., A.A. and D.Z.; project administration, M.O., A.A. and D.Z.; funding acquisition, M.O., A.A. and D.Z. All authors have read and agreed to the published version of the manuscript.

Funding: This project received funding from the European Union’s Horizon 2020 research and innovation program under the Marie Skłodowska-Curie grant agreement No. 777810.

Institutional Review Board Statement: Not applicable.

Informed Consent Statement: Not applicable.

Data Availability Statement: Not applicable.

Acknowledgments: Alena Opalkova Siskova is acknowledged for contributing to the SEM study.

Conflicts of Interest: The authors declare no conflict of interest.

References

- Liu, H.; Li, Q.; Zhang, S.; Yin, R.; Liu, X.; He, Y.; Dai, K.; Shan, C.; Guo, J.; Liu, C.; et al. Electrically Conductive Polymer Composites for Smart Flexible Strain Sensors: A Critical Review. *J. Mater. Chem. C* **2018**, *6*, 12121–12141. [\[CrossRef\]](#)
- Wang, B.; Facchetti, A. Mechanically Flexible Conductors for Stretchable and Wearable E-Skin and E-Textile Devices. *Adv. Mater.* **2019**, *31*, 1901408. [\[CrossRef\]](#)
- Gogotsi, Y.; Anasori, B. The Rise of MXenes. *ACS Nano* **2019**, *13*, 8491–8494. [\[CrossRef\]](#) [\[PubMed\]](#)
- Venkateshalu, S.; Grace, A.N. MXenes—A New Class of 2D Layered Materials: Synthesis, Properties, Applications as Supercapacitor Electrode and Beyond. *Appl. Mater. Today* **2020**, *18*, 100509. [\[CrossRef\]](#)
- Plummer, G.; Anasori, B.; Gogotsi, Y.; Tucker, G.J. Nanoindentation of Monolayer $Ti_{n+1}C_nT_x$ MXenes via Atomistic Simulations: The Role of Composition and Defects on Strength. *Comput. Mater. Sci.* **2019**, *157*, 168–174. [\[CrossRef\]](#)
- Borysiuk, V.N.; Mochalin, V.N.; Gogotsi, Y. Bending Rigidity of Two-Dimensional Titanium Carbide (MXene) Nanoribbons: A Molecular Dynamics Study. *Comput. Mater. Sci.* **2018**, *143*, 418–424. [\[CrossRef\]](#)
- Kilikevičius, S.; Kvietkaitė, S.; Žukienė, K.; Omastová, M.; Aniskevich, A.; Zeleniakienė, D. Numerical Investigation of the Mechanical Properties of a Novel Hybrid Polymer Composite Reinforced with Graphene and MXene Nanosheets. *Comput. Mater. Sci.* **2020**, *174*, 109497. [\[CrossRef\]](#)
- Zeleniakienė, D.; Monastyreckis, G.; Aniskevich, A.; Griskevicius, P. Deformation and Failure of MXene Nanosheets. *Materials* **2020**, *13*, 1253. [\[CrossRef\]](#)
- Zhang, H.; Fu, Z.H.; Legut, D.; Germann, T.C.; Zhang, R.F. Stacking Stability and Sliding Mechanism in Weakly Bonded 2D Transition Metal Carbides by van Der Waals Force. *RSC Adv.* **2017**, *7*, 55912. [\[CrossRef\]](#)
- Zhang, J.; Kong, N.; Uzun, S.; Levitt, A.; Seyedin, S.; Lynch, P.A.; Qin, S.; Han, M.; Yang, W.; Liu, J.; et al. Scalable Manufacturing of Free-Standing, Strong $Ti_3C_2T_x$ MXene Films with Outstanding Conductivity. *Adv. Mater.* **2020**, *32*, 2001093. [\[CrossRef\]](#)
- Lipatov, A.; Alhabeb, M.; Lukatskaya, M.R.; Bosen, A.; Gogotsi, Y.; Sinitskii, A. Effect of Synthesis on Quality, Electronic Properties and Environmental Stability of Individual Monolayer Ti_3C_2 MXene Flakes. *Adv. Electron. Mater.* **2016**, *2*, 1600255. [\[CrossRef\]](#)

12. Alhabeab, M.; Maleski, K.; Anasori, B.; Lelyukh, P.; Clark, L.; Sin, S.; Gogotsi, Y. Guidelines for Synthesis and Processing of Two-Dimensional Titanium Carbide ($\text{Ti}_3\text{C}_2\text{T}_x$ MXene). *Chem. Mater.* **2017**, *29*, 7633–7644. [[CrossRef](#)]
13. Maleski, K.; Ren, C.E.; Zhao, M.Q.; Anasori, B.; Gogotsi, Y. Size-Dependent Physical and Electrochemical Properties of Two-Dimensional MXene Flakes. *ACS Appl. Mater. Interfaces* **2018**, *10*, 24491–24498. [[CrossRef](#)] [[PubMed](#)]
14. Hope, M.A.; Forse, A.C.; Griffith, K.J.; Lukatskaya, M.R.; Ghidui, M.; Gogotsi, Y.; Grey, C.P. NMR Reveals the Surface Functionalisation of Ti_3C_2 MXene. *Phys.Chem.Chem.Phys.* **2016**, *18*, 5099–5102. [[CrossRef](#)] [[PubMed](#)]
15. Monastyreckis, G.; Mishnaevsky Jr., L.; Hatter, C.B.; Aniskevich, A.; Gogotsi, Y.; Zeleniakienė, D. Micromechanical Modeling of MXene-Polymer Composites. *Carbon N.Y.* **2020**, *162*, 402–409. [[CrossRef](#)]
16. Zukiene, K.; Monastyreckis, G.; Kilikevicius, S.; Procházka, M.; Micusik, M.; Omastová, M.; Aniskevich, A.; Zeleniakienė, D. Wettability of MXene and Its Interfacial Adhesion with Epoxy Resin. *Mater. Chem. Phys.* **2021**, *257*, 123820. [[CrossRef](#)]
17. Hatter, C.B.; Shah, J.; Anasori, B.; Gogotsi, Y. Micromechanical Response of Two-Dimensional Transition Metal Carbonitride (MXene) Reinforced Epoxy Composites. *Compos. Part B* **2020**, *182*, 107603. [[CrossRef](#)]
18. Zhao, M.-Q.; Trainor, N.; Ren, C.E.; Torelli, M.; Anasori, B.; Gogotsi, Y. Scalable Manufacturing of Large and Flexible Sheets of MXene/Graphene Heterostructures. *Adv. Mater. Technol.* **2019**, *4*, 1800639. [[CrossRef](#)]
19. Yang, Y.; Shi, L.; Cao, Z.; Wang, R.; Sun, J. Strain Sensors with a High Sensitivity and a Wide Sensing Range Based on a $\text{Ti}_3\text{C}_2\text{T}_x$ (MXene) Nanoparticle–Nanosheet Hybrid Network. *Adv. Funct. Mater.* **2019**, *29*, 1807882. [[CrossRef](#)]
20. Orangi, J.; Hamade, F.; Davis, V.A.; Beidaghi, M. 3D Printing of Additive-Free 2D $\text{Ti}_3\text{C}_2\text{T}_x$ (MXene) Ink for Fabrication of Micro-Supercapacitors with Ultra-High Energy Densities. *ACS Nano* **2020**, *14*, 640–650. [[CrossRef](#)]
21. Tian, Y.; An, Y.; Feng, J. Flexible and Freestanding Silicon/MXene Composite Papers for High-Performance Lithium-Ion Batteries. *ACS Appl. Mater. Interfaces* **2019**, *11*, 10004–10011. [[CrossRef](#)]
22. Tang, H.; Feng, H.; Wang, H.; Wan, X.; Liang, J.; Chen, Y. Highly Conducting MXene–Silver Nanowire Transparent Electrodes for Flexible Organic Solar Cells. *ACS Appl. Mater. Interfaces* **2019**, *11*, 25330–25337. [[CrossRef](#)]
23. Yun, T.; Kim, H.; Iqbal, A.; Cho, Y.S.; Lee, G.S.; Kim, M.; Kim, S.J.; Kim, D.; Gogotsi, Y.; Kim, S.O.; et al. Electromagnetic Shielding of Monolayer MXene Assemblies. *Adv. Mater.* **2020**, *32*, 1906769. [[CrossRef](#)]
24. Wang, Z.; Qin, S.; Seyedin, S.; Zhang, J.; Wang, J.; Levitt, A.; Li, N.; Haines, C.; Ovalle-Robles, R.; Lei, W.; et al. High-Performance Biscrolled MXene/Carbon Nanotube Yam Supercapacitors. *Small* **2018**, *14*, 1802225. [[CrossRef](#)] [[PubMed](#)]
25. Kim, S.J.; Koh, H.-J.; Ren, C.E.; Kwon, O.; Maleski, K.; Cho, S.; Anasori, B.; Kim, C.; Choi, Y.; Kim, J.; et al. Metallic $\text{Ti}_3\text{C}_2\text{T}_x$ MXene Gas Sensors with Ultrahigh Signal-to-Noise Ratio. *ACS Nano* **2018**, *12*, 986–993. [[CrossRef](#)]
26. An, H.; Habib, T.; Shah, S.; Gao, H.; Patel, A.; Echols, I.; Zhao, X.; Radovic, M.; Green, M.J.; Lutkenhaus, J.L. Water Sorption in MXene/Polyelectrolyte Multilayers for Ultrafast Humidity Sensing. *ACS Appl. Nano Mater.* **2019**, *2*, 948–955. [[CrossRef](#)]
27. Wang, L.; Zhang, M.; Yang, B.; Tan, J.; Ding, X. Highly Compressible, Thermally Stable, Light-Weight, and Robust Aramid Nano Fibers/ Ti_3AlC_2 MXene Composite Aerogel for Sensitive Pressure Sensor. *ACS Nano* **2020**, *14*, 10633–10647. [[CrossRef](#)] [[PubMed](#)]
28. Shi, X.; Wang, H.; Xie, X.; Xue, Q.; Zhang, J.; Kang, S.; Wang, C.; Liang, J.; Chen, Y. Bioinspired Ultrasensitive and Stretchable MXene-Based Strain Sensor via Nacre-Mimetic Microscale “Brick-and-Mortar” Architecture. *ACS Nano* **2019**, *13*, 649–659. [[CrossRef](#)] [[PubMed](#)]
29. Cai, Y.; Shen, J.; Ge, G.; Zhang, Y.; Jin, W.; Huang, W.; Shao, J.; Yang, J.; Dong, X. Stretchable $\text{Ti}_3\text{C}_2\text{T}_x$ MXene/Carbon Nanotube Composite Based Strain Sensor with Ultrahigh Sensitivity and Tunable Sensing Range. *ACS Nano* **2018**, *12*, 56–62. [[CrossRef](#)] [[PubMed](#)]
30. Chakraborty, I.; Bodurtha, K.J.; Heeder, N.J.; Godfrin, M.P.; Tripathi, A.; Hurt, R.H.; Shukla, A.; Bose, A. Massive Electrical Conductivity Enhancement of Multilayer Graphene/Polystyrene Composites Using a Nonconductive Filler. *ACS Appl. Mater. Interfaces* **2014**, *6*, 16472–16475. [[CrossRef](#)] [[PubMed](#)]
31. Seyedin, S.; Uzun, S.; Levitt, A.; Anasori, B.; Dion, G.; Gogotsi, Y.; Razal, J.M. MXene Composite and Coaxial Fibers with High Stretchability and Conductivity for Wearable Strain Sensing Textiles. *Adv. Funct. Mater.* **2020**, *30*, 1910504. [[CrossRef](#)]
32. Shi, X.; Liu, S.; Sun, Y.; Liang, J.; Chen, Y. Lowering Internal Friction of 0D–1D–2D Ternary Nanocomposite-Based Strain Sensor by Fullerene to Boost the Sensing Performance. *Adv. Funct. Mater.* **2018**, *28*, 1800850. [[CrossRef](#)]
33. Georgousis, G.; Pandis, C.; Kalamiotis, A.; Georgiopoulos, P.; Kyritsis, A.; Kontou, E.; Pissis, P.; Micusik, M.; Czanikova, K.; Kulicek, J.; et al. Strain Sensing in Polymer/Carbon Nanotube Composites by Electrical Resistance Measurement. *Compos. PART B* **2015**, *68*, 162–169. [[CrossRef](#)]
34. Rizzi, L.; Zienert, A.; Schuster, J.; Köhne, M.; Schulz, S.E. Electrical Conductivity Modeling of Graphene-Based Conductor Materials. *ACS Appl. Mater. Interfaces* **2018**, *10*, 43088–43094. [[CrossRef](#)]
35. Clark, K.W.; Zhang, X.; Vlasiouk, I.V.; He, G.; Feenstra, R.M.; Li, A. Spatially Resolved Mapping of Electrical Conductivity across Individual Domain (Grain) Boundaries in Graphene. *ACS Nano* **2013**, *7*, 7956–7966. [[CrossRef](#)]
36. Hu, N.; Karube, Y.; Yan, C.; Masuda, Z.; Fukunaga, H. Tunneling Effect in a Polymer/Carbon Nanotube Nanocomposite Strain Sensor. *Acta Mater.* **2008**, *56*, 2929–2936. [[CrossRef](#)]
37. Martínez-Luengo, M.; Kolios, A.; Wang, L. Structural Health Monitoring of Offshore Wind Turbines: A Review through the Statistical Pattern Recognition Paradigm. *Renew. Sustain. Energy Rev.* **2016**, *64*, 91–105. [[CrossRef](#)]
38. Du, Y.; Zhou, S.; Jing, X.; Peng, Y.; Wu, H.; Kwok, N. Damage Detection Techniques for Wind Turbine Blades: A Review. *Mech. Syst. Signal Process.* **2020**, *141*, 106445. [[CrossRef](#)]

39. García-Miquel, H.; Barrera, D.; Amat, R.; Kurlyandskaya, G.V.; Sales, S. Magnetic Actuator Based on Giant Magnetostrictive Material Terfenol-D with Strain and Temperature Monitoring Using FBG Optical Sensor. *Measurement* **2016**, *80*, 201–206. [[CrossRef](#)]
40. Zhang, C.J.; Anasori, B.; Seral-Ascaso, A.; Park, S.; Mcevoy, N.; Shmeliov, A.; Duesberg, G.S.; Coleman, J.N.; Gogotsi, Y.; Nicolosi, V. Transparent, Flexible, and Conductive 2D Titanium Carbide (MXene) Films with High Volumetric Capacitance. *Adv. Mater.* **2017**, *29*, 1702678. [[CrossRef](#)]
41. Hassan, G.; Bae, J.; Hassan, A.; Ali, S.; Lee, C.H.; Yohan Choi, Y. Ink-Jet Printed Stretchable Strain Sensor Based on Graphene/ZnO Composite on Micro-Random Ridged PDMS Substrate. *Compos. Part A* **2018**, *107*, 519–528. [[CrossRef](#)]
42. Ling, Z.; Ren, C.E.; Zhao, M.-Q.; Yang, J.; Giammarco, J.M.; Qiu, J.; Barsoum, M.W.; Gogotsi, Y. Flexible and Conductive MXene Films and Nanocomposites with High Capacitance. *Proc. Natl. Acad. Sci. USA* **2014**, *111*, 16676–16681. [[CrossRef](#)] [[PubMed](#)]
43. Fan, Z.; He, H.; Yu, J.; Liu, L.; Liu, Y.; Xie, Z. Lightweight Three-Dimensional Cellular MXene Film for Superior Energy Storage and Electromagnetic Interference Shielding. *ACS Appl. Energy Mater.* **2020**. [[CrossRef](#)]
44. Habib, T.; Zhao, X.; Shah, S.A.; Chen, Y.; Sun, W.; An, H.; Lutkenhaus, J.L.; Radovic, M.; Green, M.J. Oxidation stability of $Ti_3C_2T_x$ MXene nanosheets in solvents and composite films. *npj 2D Mater. Appl.* **2019**, *3*, 8. [[CrossRef](#)]
45. Novoselova, I.P.; Petruhins, A.; Wiedwald, U.; Weller, D.; Rosen, J.; Farle, M.; Salikhov, R. Long-Term Stability and Thickness Dependence of Magnetism in Thin $(Cr_{0.5}Mn_{0.5})_2GaC$ MAX Phase Films. *Mater. Res. Lett.* **2019**, *7*, 159–163. [[CrossRef](#)]
46. Lee, Y.; Kim, S.J.; Kim, Y.-J.; Lim, Y.; Chae, Y.; Lee, B.-J.; Kim, Y.-T.; Han, H.; Gogotsi, Y.; Ahn, C.W. Oxidation-resistant titanium carbide MXene films. *J. Mater. Chem. A* **2020**, *8*, 573. [[CrossRef](#)]
47. Limbu, T.B.; Chitara, B.; Orlando, J.D.; Cervantes, M.Y.G.; Kumari, S.; Li, Q.; Tang, Y.; Yan, F. Green synthesis of reduced $Ti_3C_2T_x$ MXene nanosheets with enhanced conductivity, oxidation stability, and SERS activity. *J. Mater. Chem. C* **2020**, *8*, 4722. [[CrossRef](#)]
48. Zhou, B.; Zhang, Z.; Li, Y.; Han, G.; Feng, Y.; Wang, B.; Zhang, D.; Ma, J.; Liu, C. Flexible, Robust, and Multifunctional Electromagnetic Interference Shielding Film with Alternating Cellulose Nanofiber and MXene Layers. *ACS Appl. Mater. Interfaces* **2020**, *12*, 4895–4905. [[CrossRef](#)] [[PubMed](#)]
49. Yang, W.; Liu, J.-J.; Wang, L.-L.; Wang, W.; Yuen, A.C.Y.; Yuen, Y.; Peng, S.; Yu, B.; Lu, H.-D.; Yeoh, G.H.; et al. Multifunctional MXene/Natural Rubber Composite Films with Exceptional Flexibility and Durability. *Compos. Part B* **2020**, *188*, 107875. [[CrossRef](#)]
50. Chertopalov, S.; Mochalin, V.N. Environment-Sensitive Photoresponse of Spontaneously Partially Oxidized Ti_3C_2 MXene Thin Films. *ACS Nano* **2018**, *12*, 6109–6116. [[CrossRef](#)] [[PubMed](#)]

Article

Scalable MXene and PEDOT-CNT Nanocoatings for Fibre-Reinforced Composite De-Icing

Gediminas Monastyreckis ^{1,*}, Juan Tortosa Siles ¹, Petr Knotek ², Maria Omastova ³, Andrey Aniskevich ⁴ and Daiva Zeleniakienė ¹

¹ Department of Mechanical Engineering, Kaunas University of Technology, Studentu St. 56, 51424 Kaunas, Lithuania; j.tortosa@alumnos.upm.es (J.T.S.); daiva.zeleniakienė@ktu.lt (D.Z.)

² Department of General and Inorganic Chemistry, University of Pardubice, Studentska 573, 532 10 Pardubice, Czech Republic; petr.knotek@upce.cz

³ Polymer Institute, Slovak Academy of Sciences, Dubravska cesta 9, 845 41 Bratislava, Slovakia; maria.omastova@savba.sk

⁴ Institute for Mechanics of Materials, University of Latvia, Jelgavas Str. 3, LV-1004 Riga, Latvia; andrey.aniskevich@pmi.lv

* Correspondence: gediminas.monastyreckis@ktu.edu; Tel.: +370-61104007

Abstract: In this study, the de-icing performance is investigated between traditional carbon fibre-based coatings and novel MXene and poly(3,4-ethylenedioxythiophene)-coated single-walled carbon nanotube (PEDOT-CNT) nanocoatings, based on simple and scalable coating application. The thickness and morphology of the coatings are investigated using atomic force microscopy and scanning electron microscopy. Adhesion strength, as well as electrical properties, are evaluated on rough and glossy surfaces of the composite. The flexibility and electrical sensitivity of the coatings are studied under three-point bending. Additionally, the influence of ambient temperature on coating's electrical resistance is investigated. Finally, thermal imaging and Joule heating are analysed with high-accuracy infrared cameras. Under the same power density, the increase in average temperature is 84% higher for MXenes and 117% for PEDOT-CNT, when compared with fibre-based coatings. Furthermore, both nanocoatings result in up to three times faster de-icing. These easily processable nanocoatings offer fast and efficient de-icing for large composite structures such as wind turbine blades without adding any significant weight.

Keywords: nanocoatings; thermal imaging; de-icing; fibre-reinforced composites; MXenes; PEDOT-CNT



check for updates

Citation: Monastyreckis, G.; Siles, J.T.; Knotek, P.; Omastova, M.; Aniskevich, A.; Zeleniakienė, D. Scalable MXene and PEDOT-CNT Nanocoatings for Fibre-Reinforced Composite De-Icing. *Materials* **2022**, *15*, 3535. <https://doi.org/10.3390/ma15103535>

Academic Editor: Andrew Ruys

Received: 15 April 2022

Accepted: 9 May 2022

Published: 14 May 2022

Publisher's Note: MDPI stays neutral with regard to jurisdictional claims in published maps and institutional affiliations.



Copyright: © 2022 by the authors. Licensee MDPI, Basel, Switzerland. This article is an open access article distributed under the terms and conditions of the Creative Commons Attribution (CC BY) license (<https://creativecommons.org/licenses/by/4.0/>).

1. Introduction

Wind turbine farms expand offshore and in cold regions due to higher wind speeds and air density, resulting in more energy production [1]. On the other hand, harsh climate conditions usually affect their functionality and lifetime [2,3]. Ice formation on the blades is one of the most severe problems, causing disturbed aerodynamic flow and reducing the wind turbine's efficiency by up to 20% [4,5]. Additionally, it can cause excessive vibrations, unequal load distribution, and ice debris can damage the composite structures [6,7], leading to higher maintenance costs [8]. Ice preventing systems, so-called anti-icing, are based on various hydrophobic coatings, whereas de-icing is based on active heating using embedded heaters or hot air tubing [9,10]. Traditional de-icing systems are not always efficient and can result in a turbine's power consumption of 5–10% [11]. Moreover, metal-based heaters usually experience face-sheet debonding and are vulnerable to lightning strikes [12,13], while carbon fibre (CF) based heaters require specific manufacturing integration during the moulding of the blade [14]. Until now, the demand for highly efficient, green, and scalable de-icing coating technology remains.

In the early 21st century, the fabrication of nanoparticles such as graphenes (GP) and carbon nanotubes (CNT) has led researchers to explore their new applicability [15–17]. Due

to high electrical conductivity and low thickness, the formation of ultrathin coatings for Joule heating has gained attention [18]. Joule heating is a process when a current flowing through a resistor, in this case, a resistive nanocoating or carbon-based fabric, is transformed into heat, following Joule's first law. Pure carbon-based nanocoatings possess hydrophobic properties and can be vulnerable to scratching. Therefore, conductive polymers such as poly(3,4-ethylenedioxythiophene) (PEDOT) can be used as shells of the nanoparticles, improving their electrical properties and stability [19]. The de-icing coating based on Joule heating using GP doped epoxy was analysed by Redondo et al. [20]. At the filler amount of 12 wt%, the heating rate of 13.6 °C/min was obtained under a power density of 0.125 W/cm². Another study was based on GP coated glass fibre (GF) rowing, which increased by 80 °C after 180 s of 10 V heating [21]. Raji et al. [22] used epoxy-GP nanoribbon composite (5 wt%) and under 0.375 W/cm² power density, achieved a heating rate of ~30 °C/min. Ten-layered aligned CNT coating of 6 µm thickness was also investigated for de-icing coatings by Yao et al. [23]. The coating showed 48 °C/min at 0.128 W/cm².

Another novel two-dimensional (2D) nanoparticle similar to GP is MXene. The most studied MXene particle Ti₃C₂T_z has shown excellent mechanical and electrical properties [24–26]. These properties can be influenced by different delamination methods [27]. Good compatibility and wettability properties between MXenes and epoxy-based composites were also reported [28–30]. In addition, MXenes are thermally stable and can heat up to 700 °C with minor degradation [31]. Easily processable methods of MXenes, and scalable application technology such as spray coating, are attractive for de-icing [32]. Despite this, Joule heating of MXenes was investigated only recently. Jia et al. [33] deposited Ti₃C₂ MXenes on a wood-pulp fabric grid followed by a hydrophobic methyltrimethoxysilane layer. By applying 0.174 W/cm², a heating rate of 63 °C/min was achieved. Another experiment was performed by Li et al. [34], who prepared free-standing MXene-montmorillonite (MMT) thin film with the weight ratios of MXene to MMT of 90:10. The heating rate of the film was 100 °C/min under a power density of 4.58 W/cm². The authors also reported the film to be stable under heating cycles.

Until now, only a few nanocoatings have been investigated for fibre-reinforced composite de-icing. In this work, for the first time, novel MXene and PEDOT-CNT nanocoatings are used. This research aimed to develop such nanocoatings using scalable water-based spray-coating methods and investigate their adhesion strength, flexibility, heating properties, and de-icing performance.

2. Materials and Methods

2.1. Materials and Specimens

Ti₃C₂T_z MXenes were prepared from Ti₃AlC₂ MAX phase with a particle size of <40 µm and purity of 98 wt% (MRC, Kyiv, Ukraine). The etching solvents were hydrochloric acid (37 wt%, Merck, Darmstadt, Germany) and lithium fluoride (>99 wt%, Merck, Darmstadt, Germany). MAX phase was stirred for 24 h at room temperature. The multi-layer MXene sediment was further delaminated using 99 wt% LiCl (Merck, Darmstadt, Germany). The resulting solution was centrifuged 12 times at 3500 rpm and washed until the pH of the supernatant reached above 6. The concentration of the delaminated MXenes in the supernatant was reconcentrated from 0.34 mg/mL to 3 mg/mL, more suitable for spraying. PEDOT/(CNT+SO₃H) aqueous paste with a 1:1 ratio (SYNPO, Pardubice, Czech Republic) was used for CNT coating preparation. The paste was reconcentrated to 0.33 mg/mL, which was more suitable for spraying without nozzle jamming.

Sandwich structured glass fibre-reinforced polymer (GFRP) composites were prepared by hand-layup and vacuum bagging methods. The samples consisted of 8 plies 163 g/m² twill-weave Interglas 92110 (Porcher Industries, Erbach, Germany), separated by 4 mm thick polyvinyl chloride foam (AIREX[®] C70.75, Sins, Switzerland). The thermosetting epoxy resin Bisphenol F-epichlorohydrin and an amine curing agent were mixed at a ratio of 10:3 (Biresin[®] CR-122-5, Sika, Zürich, Germany). All specimens were cured at room temperature for 24 h and post-cured in a convection oven for 4 h at 100 °C. Peel-ply fabric

polyamide 6.6 (plain weave, 64 g/m²) and polyethylene film were used to make rough and glossy surfaces of the specimens, respectively.

2.2. Coating Preparation

Unidirectional CF coating was made from 160 g/m² plain weave fabric (R&G GmbH, Waldenbuch, Germany) by removing horizontal fibres and leaving four separated 3000 filament stripes for the wire connection (Figure S1a). The coating was used as the last layer of the composite and was cured using the vacuum bagging technique. Copper wires were glued to the coating by melting electrically conductive polylactic acid (PLA) (Protopasta, Protoplant, Inc., Vancouver, Canada), which was additionally covered with a thin layer of silver paint to reduce the contact resistance. The chopped CF coating (Figure S1b) was made from 3 mm CF strands (R&G GmbH, Germany) mixed with epoxy resin at a weight fraction of 1%. The coating was additionally covered with a 3000 CF “fork-type” filament grid and pressed and cured under the vacuum for the sedimentation of chopped fibres. The composite samples used for nanocoatings were firstly treated with Ar enriched plasma for 3 min at 80 W and 40 kHz, using a Zepto Diener low-pressure plasma cleaner (Diener electronic GmbH & Co. KG, Ebhausen, Germany). As a result, the water contact angle of the glossy composite surface was reduced from 70 to 25°, which determined more uniform nanocoatings. After the plasma treatment, water-based MXenes with a 3 mg/mL concentration were spray-coated several times, depending on the investigation (Figure S1c). Here, one-time sprayed means one coating layer made from 1 mL/85 cm² spray yield, followed by a natural drying of 10 min. The PEDOT-CNT coating was made using the same technique as for MXene coating (Figure S1d). Both nanocoatings were prepared using a Sparmax HB-040 airbrush (Anest Iwata Sparmax Co., Ltd., Taiwan, China). After drying, the nanocoatings were applied with 7 mm silver paint stripes at the edges and additionally coated with a protective epoxy layer of 0.15 mm thickness. All four samples had the same heating area of 85 ± 1 cm².

2.3. Characterisation and Testing

For the characterisation, 3-layer MXene and 5-layer PEDOT-CNT coatings were used. The morphology of the nanocoatings was characterised using scanning electron microscopy (SEM) (S-3400N, Hitachi, Tokyo, Japan). Silicon wafers (1 × 1 cm) were used as nanocoating substrates. The EDX measurements were performed using high vacuum mode, BRUKER Quantax EDS detector, and a working distance of 10 mm. The electron accelerating voltages were 5 keV for both magnifications. The thickness of MXene flakes and MXene coating was measured using atomic force microscopy (AFM) (Dimension Icon, Bruker, Billerica, Massachusetts, USA) based on the scratch method [35]. The topography of the surface was monitored in PeakForce quantitative nanoscale mechanical mode using ScanAsyst-Air tips ($k = 0.4 \text{ N}\cdot\text{m}^{-1}$). The 10 × 10 μm sample images were recorded at a scanning frequency of 0.5 Hz. The roughness of the GFRP composite surface was analysed using 3D optical microscopy (Leica DVM6, Leica Microsystems, Wetzlar, Germany).

Adhesion tests (Figure S2) of the coatings were performed on 8-ply GFRP specimens (15 × 3 cm) with glossy and rough surfaces using an Adheometer PM 420/63, under ISO-4624 standards. The square sheet electrical resistance (Ω/sq) dependencies on the nanocoating layers and substrate roughness were measured using a two-probe Fluke 287 True-RMS multimeter (Fluke Corporation, Everett, Washington, USA). Electrical resistance stability under ambient temperatures was performed in a temperature-controlled oven and a freezer.

Three-point bending tests (Figure S3) were performed with sandwich structured GFRP samples (10 × 2.5 cm) using Tinius Olsen H25 KT universal testing machine (Tinius Olsen, Redhill, UK) under ISO-178 standards. Electrical resistances changes of tensiled and compressed nanocoating surfaces during the bending were measured between two silver paint stripes at the edges of the specimen (8.5 cm distance).

For thermal imaging analysis (Figure S4) and de-icing (Figure S5), the layers of nanocoatings were increased to 5 for MXenes and 8 for PEDOT-CNT, in order to achieve higher conductivity and perform heating in lower voltages. The investigation was performed with sandwich structured GFRP samples (10×10 cm) using an external power supply (Axiomet AX-12001 DBL, Transfer Multisort Elektronik, Łódź, Poland). The DC power (W) for all coatings was determined by first tested chopped CF coating, subjected to 5 V voltage (0.372 A current) and 10 V (0.744 A). Therefore, other coatings were also applied with the same power of 1.86 and 7.44 W. The heating time was chosen for 300 and 180 s, respectively, where the shorter time for 7.44 W was limited to the wire overheating. The temperatures were monitored using an infrared camera FLIR SC7500 (Teledyne FLIR LLC, Wilsonville, Oregon, USA), with a pixel pitch of $30 \mu\text{m}$ and $\pm 1\%$ temperature accuracy. For a de-icing experiment, 5 ± 1 mm thick ice (tap water) was naturally formed on top of the coating in a $-15 \text{ }^\circ\text{C}$ freezer. The de-icing of the coatings was performed at room temperature under DC power of 7.44 W.

3. Results

3.1. Coating Characterisation

The morphology of the nanocoatings, particle sizes, and structural integrity were studied using SEM. A three-layer MXene coating is presented in Figure 1a,b. Here, wrinkles were formed due to non-delaminated fragments and an overlapping structure (yellow arrows). The wrinkle extension of $10 \mu\text{m}$ from the fragment can be seen and is expected to have an effect on electrical conductivity and adhesion properties. Figure 1b shows a magnified region of MXene coating, where fully delaminated and overlapping flakes of $3\text{--}6 \mu\text{m}$ in size can be observed. We can also notice a non-adhered corner of the top flake, and sharp flake waviness, which suggests weak flexural rigidity of fully delaminated MXenes [36]. A five-layer PEDOT-CNT coating is presented in Figure 1c,d, where larger nanotube agglomerations and fibre-like bundles that stretch more than $30 \mu\text{m}$ are observed. Under higher magnification (Figure 1d), we can notice a more uniform single-walled CNT web-like structure. Although, the differences in CNT thickness and lengths are affected by conductive polymer PEDOT, which forms a shell around the tubes and acts as an adhesive matrix.

The thickness of Ti_3C_2 MXene flakes and three-layer coating was measured using AFM. In Figure 2a, we can notice a $0.5 \mu\text{m}$ size and 1.2 ± 0.1 nm thickness MXene flake on top of another flake. This represents a fully delaminated single-layered $\text{Ti}_3\text{C}_2\text{T}_z$ flake, where T_z stands for functional surface groups (-O, -OH, and -F). Then, the bottom flake would roughly stand for a double-layered MXene flake with a thickness of 2.6 ± 0.1 nm, which is in good agreement with other studies [37]. The thickness of the MXene coating near the scratch could be evaluated in Figure 2b. Here, a gradual thickness increase of $2.3\text{--}2.7$ nm can be observed at every $0.5\text{--}1 \mu\text{m}$ length, starting from the silicon wafer substrate and ending at 17 nm. Figure 2c demonstrates the statistical thickness scattering of a three-layer MXene coating, which was measured in three different sample places, with a mean value of 21 nm, standard error (SE) of 2 nm, and minimal and maximal values of 10 and 37 nm, respectively. In Figure 2d, a topographical map of the coating is presented. Here we can notice a smooth surface with several peaks above 60 nm, representing non-delaminated MXenes fragments. The AFM topography image shows that the coating is a well-defined overlapping structure with a lateral flake size of $2\text{--}6 \mu\text{m}$, which corresponds with SEM analysis. PEDOT-CNT coating thickness was not measured using AFM due to its flexible and porous web-like structure, but it was roughly estimated for $150\text{--}250$ nm, assuming a solution concentration of 0.33 mg/mL, one layer spray yield of 1 mL/ 85 cm², the density of CNT, and the film's porosity.

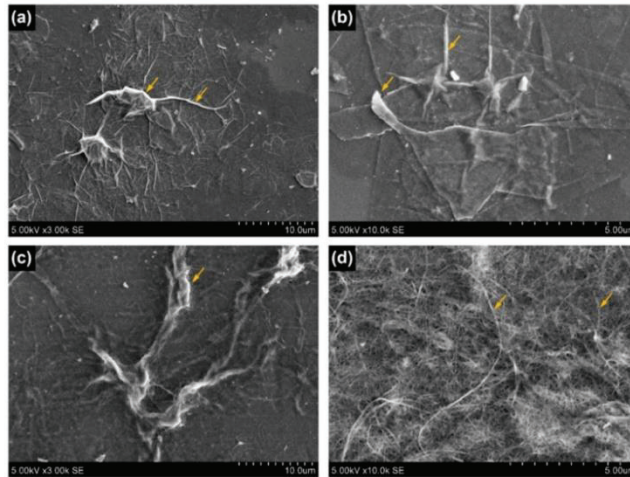


Figure 1. Scanning electron microscopy images of: (a) 3-layer MXene coating (b) magnified region; (c) 5-layer PEDOT-CNT coating (d) magnified region (yellow arrows clarified in the text).

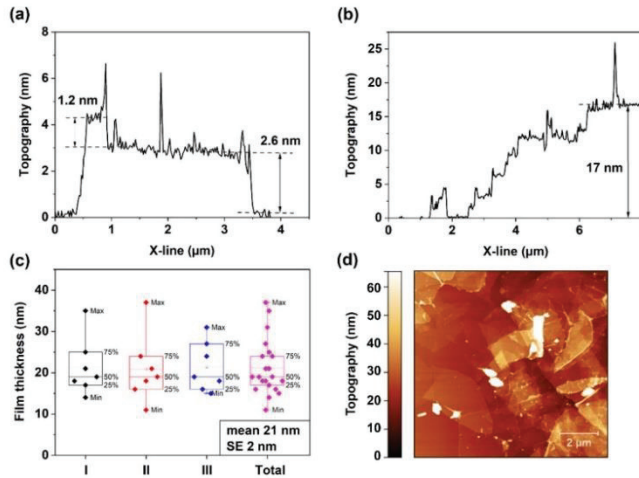


Figure 2. Atomic force microscopy analysis: (a) thickness measurement of delaminated single-layered and double-layered $Ti_3C_2T_x$ MXene flakes; (b) 3-layer MXene coating thickness; (c) statistical thickness analysis of the coating; (d) topographical map of 3-layer MXene coating (close to scratch).

3.2. Electrical Properties and Adhesion Strength

In order to develop a durable and compatible de-icing coating, one must approach its suitable electrical properties and adhesion strength. Firstly, the electrical properties of the coatings were investigated. The square sheet resistance dependence on the coating

layers is shown in Figure 3a. Both coatings were prepared on plasma-treated GFRP samples with a glossy surface. MXene nanocoating showed that the resistance decreased roughly tenfold with every additional layer, starting from $500 \text{ k}\Omega/\text{sq}$ for the first layer and ending at around $200 \pm 20 \text{ }\Omega/\text{sq}$ for the fifth layer. PEDOT-CNT coating did not show such a rapid decrease in resistance, and after the fourth layer, the slope slightly flattened. The first layer showed resistance of $7 \text{ M}\Omega/\text{sq}$, and the fifth layer— $10.5 \pm 0.7 \text{ k}\Omega/\text{sq}$, which is more than 50 times higher when compared with MXenes. It was not efficient to stack up more than eight layers of PEDOT-CNT due to insignificant changes in the resistance (Figure 3a), and the final values were $3 \pm 0.3 \text{ k}\Omega/\text{sq}$. Regarding the thickness of the coatings (see Section 3.1), the conductivity of the final MXene coating on the glossy surface was equal to $\sim 1000 \text{ S/cm}$ and PEDOT-CNT— 15 S/cm .

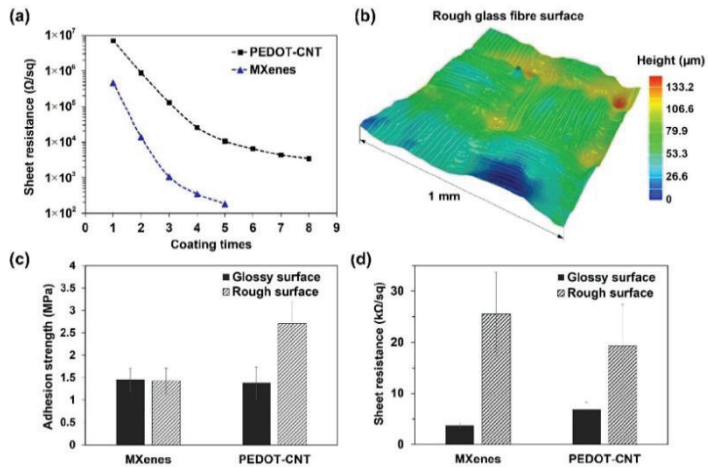


Figure 3. Electrical properties and adhesion strength of the nanocoatings: (a) electrical resistance dependence on the coating layers of MXenes and PEDOT-CNT; (b) 3D optical topography image of rough GFRP composite surface; (c) adhesion strength comparison between 3-layer MXene and 5-layer PEDOT-CNT on glossy and rough surfaces; (d) electrical resistance dependence on rough and glossy surfaces.

It is known that the coating's adhesion and electrical properties depend on the substrate's wettability and roughness [38]. A 3D optical topography image ($1 \times 1 \text{ mm}$) of a rough GFRP surface is presented in Figure 3b, with a roughness of $\sim 50 \text{ }\mu\text{m}$, while a glossy surface was $\sim 1 \text{ }\mu\text{m}$. Adhesion strength results of three-layer MXene and five-layer PEDOT-CNT are presented in Figure 3c. The MXene coating showed roughly 1.5 MPa for both glossy and rough surfaces, while the PEDOT-CNT coating showed 1.4 and 2.7 MPa , respectively. The PEDOT-CNT fracture behaviour on glossy and rough surfaces suggests that the adhesive glue went through the CNT web-like structure and adhered directly with the GFRP sample, resulting in almost twice higher strength. This observation is also supported by the high increase in electrical resistance during the metal holder glueing. In contrast, the adhesion strength of MXene coating on both surfaces was similar, and we could expect MXene–MXene interaction to be the main factor, as was previously reported [39]. In comparison, non-coated GFRP composite resulted in up to three times higher adhesion strength than nanocoatings due to a strong epoxy–epoxy interaction.

The electrical resistance dependence on substrate roughness is shown in Figure 3d. Here, electrical resistance differs up to seven times for MXenes, and only three times for

CNTs when comparing glossy and rough surfaces. These results suggest that CNTs can easily deform and shape against the substrate without losing conductivity, while 2D MXene flakes are less flexible.

3.3. Ambient Temperature and Flexibility

It is important to understand how the electrical properties of the coatings behave in different ambient temperatures and under mechanical deformations during the exploitation. In Figure 4, the electrical resistance changes in the -15 – 60 °C temperature conditions are presented. In Figure 4a, MXene nanocoating shows a stable resistance increase at the ratio of 1.2% per 10 °C. In contrast, PEDOT-CNT coating shows a decrease of 4.7% per 10 °C (Figure 4b). Such behaviour of MXenes is similar to metals, while the opposite behaviour of PEDOT-CNT is similar to carbon-based materials.

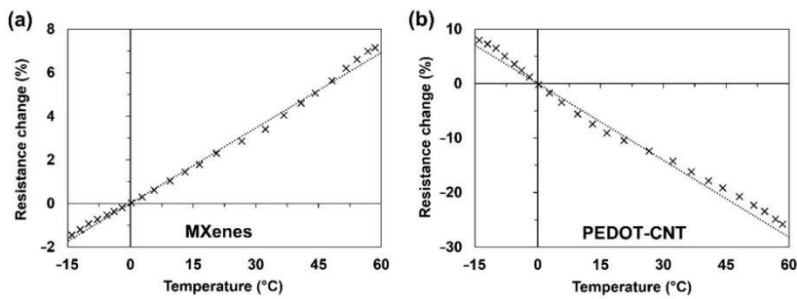


Figure 4. Electrical resistance changes under the ambient temperature of: (a) MXene and (b) PEDOT-CNT coatings.

Another important characteristic of de-icing heaters is the electrical resistance stability during deformation. The resistance was monitored under three-point bending separately for lower and upper surfaces, deforming under tension and compression, respectively (Figure 5). In addition, the bending test included four cycles, each reaching ever higher deflection values of 2, 3, 4, and 8 mm, resulting in flexural strain (ϵ) of 1, 1.5, 2, and 4%, respectively. Tensiled MXenes showed a slight increase in resistance, while the values were opposite under compression (Figure 5a). When the deflection was restored to 0 mm after each cycle, the coating's resistance did not return to the initial value, as was previously reported [39]. In contrast, PEDOT-CNT coating returned almost exactly to the initial resistance value after each cycle (Figure 5b). At $\sim 3\%$ compression strain, both coatings showed a steep electrical resistance increase due to the initial cracking of the composite's top laminate, which together damaged the coating. However, MXene coating resulted in a sudden resistance increase of 30% (not shown in Figure 4a), while PEDOT-CNT coating resulted in only a 1.5% increase. Such results indicate that MXenes are adhered to the substrate and will likely crack together with the surface fibres. The piezo-resistive mechanism of MXenes is based on flake-to-flake conductivity loss. In contrast, PEDOT-CNT coating is more flexible, and a web-like nanotube structure is expected to realign or deform, and in such a way, the tube-to-tube conductivity is maintained. Despite the resistance change due to ambient temperature or deformations, to perform the de-icing procedure under the same power density, one can increase the applied voltage following Joule's first law.

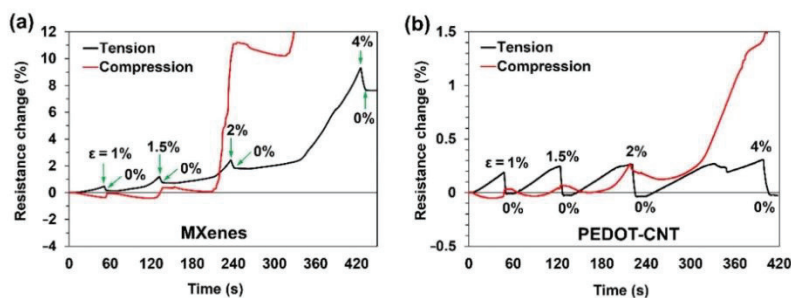


Figure 5. Resistance changes of tensiled and compressed surfaces under three-point bending at different flexural strains of: (a) MXene and (b) PEDOT-CNT coatings.

3.4. Thermal Imaging and De-Icing

Thermal imaging was performed to check coatings integrity, temperature leaks in high resistive areas, and de-icing efficiency. The heating performance of the coatings was compared using the same power density (W/cm^2). In Figure 6, thermal images after continuous heating at room temperature for 300 s with 1.86 W are presented. In the unidirectional CF sample, temperature concentrated near wire connections (Figure 6a), which was caused by high resistivity differences between conductive PLA ($0.15 \Omega m$), silver paint ($10^{-7} \Omega m$), and CF ($10^{-5} \Omega m$). Chopped CF coating showed similar behaviour (Figure 6b), where non-uniformly heated areas appeared due to unevenly distributed CF strands, with temperatures of up to $70^\circ C$. In contrast, MXene nanocoating (Figure 6c) did not possess wire overheating due to the higher resistance of MXenes (245.9Ω). Additionally, the temperature accumulated in the middle of the sample, although the right side was slightly colder due to hand-spraying defects. PEDOT-CNT coating shown in Figure 6d resulted in the best temperature distribution, possibly caused by a web-like structure and more coating layers. In addition, due to the high coating resistance of PEDOT-CNT (3094Ω), no wiring overheating was observed.

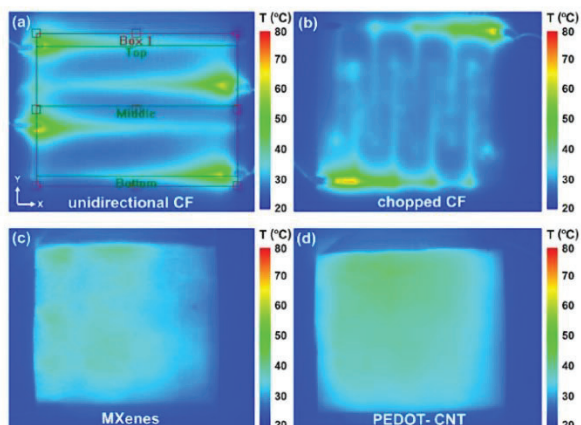


Figure 6. Thermal imaging analysis under 1.86 W power and 300 s of: (a) unidirectional CF; (b) chopped CF; (c) 5-layer MXene and (d) 8-layer PEDOT-CNT coatings.

Joule’s heating (1.86 W, 300 s) is also studied along three linear sections named “Top, Middle, Bottom”, and in the area (85 cm²) named “Box 1”, shown in Figure 6a. Unidirectional CF coating (Figure 7a) shows temperature concentrations at the edges of up to 55 °C, while temperatures in the middle of the sample are relatively uniform and reach 29 °C. A sample with chopped CF shown in Figure 7b follows a similar trend. Here, the temperature at the wiring reached 68 °C and in the middle 31 °C. We can also notice temperature peaks at the CF filament grid connections due to higher contact resistance. In contrast, MXene and PEDOT-CNT coatings (Figure 7c,d) result in a more even temperature distribution along the linear sections, scattering between 34 and 41 °C. However, PEDOT-CNT coating showed smoother translation between individual data points, indicating better heat distribution in web-like CNT structure than overlapping 2D MXene flake structure.

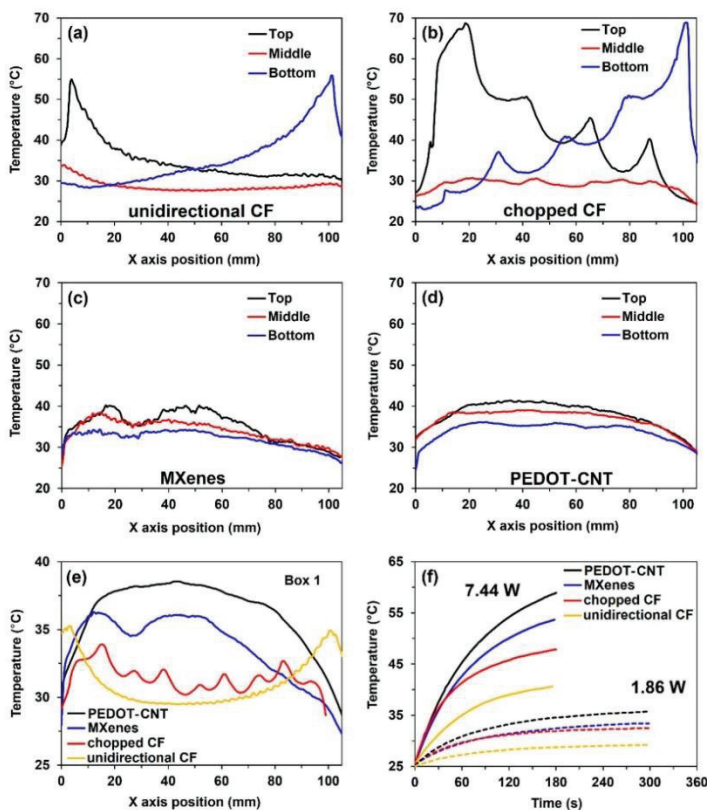


Figure 7. Comparison of temperatures along three linear sections under 1.86 W and 300 s: (a) unidirectional CF; (b) chopped CF; (c) MXenes; (d) PEDOT-CNT; (e) average temperature results of the coatings across the sample length under 1.86 W and 300 s; (f) average temperature increase overtime under 1.86 and 7.44 W.

The average areal temperatures (Box 1) of all four coatings after 300 s under 1.86 W, are compared in Figure 7e. The heat in unidirectional CF coating mostly accumulates at the

sample sides, while the chopped CF sample shows a slightly improved heat distribution but with more chaotic temperature jumps. In comparison, both MXene and PEDOT-CNT nano-coatings produce more heat, with CNTs being slightly better. The average coating temperature (Box 1) increases over time is presented in Figure 7f. Here, samples are additionally tested at four times higher power load (7.44 W) but shorter time—180 s, to avoid wire overheating of CF coatings. The temperature results of unidirectional CF, chopped CF, MXenes, and PEDOT-CNT coatings are 40.6, 47.9, 53.7, and 58.9 °C, respectively. In addition, the initial heating rate of the coatings is equal to 10.1, 16.3, 17.4, and 20.39 °C/min, respectively. Such results suggest the difference in the coating's efficiency, and when comparing maximum temperatures achieved over the same time, MXenes outperform traditional CF coatings by 84%, and PEDOT-CNT outperforms by 117%. The reason for such results is the much smaller thickness of the nano-coatings and fewer heat losses in the wires.

De-icing time of the coatings was evaluated under a 7.44 W power load. The de-icing time, shown in Table 1, was recorded at the moment when ice detached from the vertically positioned sample (Figure S5). A unidirectional CF coating was de-iced after 17 min when most of the ice had melted. Such prolonged time was caused by several low-heated areas, which kept the ice adhered. A similar issue appeared for chopped CF coating due to uneven heat distribution, and it took 13 min for the ice to detach. For both MXene and PEDOT-CNT coatings, the de-icing time was similar. At roughly ~5 min, the whole ice detached as one piece. These results show that nano-coatings can offer faster de-icing and lower energy consumption when compared to traditional CF-based heaters. With simple spray-coating techniques, the nano-coatings could be easily integrated into the manufacturing process or applied to existing composite structures already under exploitation. Due to their ultrathin thickness of a few dozen nanometers, MXene or PEDOT-CNT nano-coatings could also be considered for high-efficiency thermal heaters, e.g., in space applications.

Table 1. De-icing time of different coatings at the same power density of 0.088 W/cm (7.44 W).

Coating Type	Resistance [Ω]	Heating Rate [$^{\circ}\text{C}/\text{min}$]	De-Icing Time [min]
unidirectional CF	2.1	10.1	17 \pm 1
chopped CF	13.4	16.3	13 \pm 1
5-layer MXenes	245.9	17.7	5 \pm 0.5
8-layer PEDOT-CNT	3093.9	20.3	5 \pm 0.5

4. Conclusions

The characterisation of thickness and morphology was performed using AFM and SEM, respectively. The results showed that using fully delaminated MXenes, a uniform and highly conductive (1000 S/cm) nano-coating of up to 37 nm thickness can be obtained.

The coating's adhesion strength and electrical properties were investigated on rough and glossy surfaces of the composite. For MXenes, the resistance was up to seven times higher on a rough surface than on a glossy, and only three times higher for PEDOT-CNT. The adhesion strength between MXene and PEDOT-CNT was marginal.

The influence of ambient temperature on the coating's electrical properties was analysed in the -15 and 60 °C range. MXene coating showed a stable electrical resistance increase at the ratio of 1.2% per 10 °C, while PEDOT-CNT resulted in the opposite and higher ratio—a decrease of 4.7% per 10 °C.

Under three-point bending, MXene coating's electrical response was more sensitive to deformation and resulted in a permanent resistance increase, while PEDOT-CNT coating was more electrically stable and flexible.

Both MXene and PEDOT-CNT coatings resulted in uniform heat distribution throughout the sample and showed no wire-overheating, which was observed in traditional carbon fibre coatings. Additionally, the average coating temperature increase under the same power density and time was 84% higher for MXenes, and 117% for PEDOT-CNT. There-

fore, both nanocoatings resulted in up to three times faster de-icing when compared to fibre-based coatings.

These results demonstrate that MXenes and PEDOT-CNT can be used as viable materials for scalable and easily processable de-icing nanocoatings for fibre-reinforced composites. Furthermore, the nanocoatings' electrical properties and heating performance justify further investigation of onsite testing with full-scale heaters.

Supplementary Materials: The following supporting information can be downloaded at: <https://www.mdpi.com/article/10.3390/ma15103535/s1>, Figure S1: Sandwich structured GFRP composite samples coated with: (a) unidirectional CF; (b) chopped CF; (c) $Ti_3C_2T_2$ MXenes; (d) PEDOT-CNT; Figure S2: Adhesion test setup; Figure S3: Three-point bending test setup; Figure S4: Thermal imaging test setup; Figure S5: De-icing test: (a) ice formation in a $-15\text{ }^\circ\text{C}$ freezer (horizontal). De-icing (vertically positioned sample) at room temperature under 7.44 W power of: (b) unidirectional CF coating after 12 min of heating; (c) chopped CF coating after 7 min; (d) MXene coating after 1 min; (e) a fully de-iced MXene coating after 5 min; (f) detached ice after 5 min of MXene coating.

Author Contributions: Conceptualisation, G.M. and D.Z.; methodology, G.M., M.O. and D.Z.; validation, G.M. and D.Z.; formal analysis, G.M., M.O., A.A. and D.Z.; investigation, G.M., J.T.S. and P.K.; resources, M.O. and D.Z.; data curation, G.M., J.T.S. and P.K.; writing—original draft preparation, G.M.; writing—review and editing, M.O., J.T.S., P.K., A.A. and D.Z.; visualisation, G.M.; supervision, D.Z.; project administration, M.O., A.A. and D.Z.; funding acquisition, M.O. and A.A. and D.Z. All authors have read and agreed to the published version of the manuscript.

Funding: This project received funding from the European Union's Horizon 2020 research and innovation program under the Marie Skłodowska-Curie grant agreement No. 777810.

Institutional Review Board Statement: Not applicable.

Informed Consent Statement: Not applicable.

Data Availability Statement: Not applicable.

Acknowledgments: The authors would like to acknowledge SYNPO A.S. (Czech Republic) for supplying the PEDOT-CNT paste.

Conflicts of Interest: The authors declare no conflict of interest.

References

- Lydia, M.; Kumar, S.S.; Selvakumar, A.I.; Prem, G.E. A Comprehensive Review on Wind Turbine Power Curve Modeling Techniques. *Renew. Sustain. Energy Rev.* **2014**, *30*, 452–460. [[CrossRef](#)]
- Dalili, N.; Edrissy, A.; Carriveau, R. A Review of Surface Engineering Issues Critical to Wind Turbine Performance. *Renew. Sustain. Energy Rev.* **2009**, *13*, 428–438. [[CrossRef](#)]
- Wang, L.; Kolios, A.; Liu, X.; Venetsanos, D.; Rui, C. Reliability of Offshore Wind Turbine Support Structures: A State-of-the-Art Review. *Renew. Sustain. Energy Rev.* **2022**, *161*, 112250. [[CrossRef](#)]
- Jin, J.Y.; Virk, M.S. Study of Ice Accretion and Icing Effects on Aerodynamic Characteristics of DU96 Wind Turbine Blade Profile. *Cold Reg. Sci. Technol.* **2019**, *160*, 119–127. [[CrossRef](#)]
- Stoyanov, D.B.; Nixon, J.D. Alternative Operational Strategies for Wind Turbines in Cold Climates. *Renew. Energy* **2020**, *145*, 2694–2706. [[CrossRef](#)]
- Li, F.; Cui, H.; Su, H.; Ma, Z.; Zhu, Y.; Zhang, Y. Icing Condition Prediction of Wind Turbine Blade by Using Artificial Neural Network Based on Modal Frequency. *Cold Reg. Sci. Technol.* **2022**, *194*, 103467. [[CrossRef](#)]
- Pérez, M.A.; Pernas-Sánchez, J.; Artero-Guerrero, J.A.; Serra-López, R. High-Velocity Ice Impact Damage Quantification in Composite Laminates Using a Frequency Domain-Based Correlation Approach. *Mech. Syst. Signal Process.* **2021**, *147*, 107124. [[CrossRef](#)]
- Mishnaevsky, L., Jr.; Johansen, N.F.; Fraise, A.; Fæster, S.; Jensen, T.; Bendixen, B. Technologies of Wind Turbine Blade Repair: Practical Comparison. *Energies* **2022**, *15*, 1767. [[CrossRef](#)]
- Brassard, J.-D.; Laforte, J.-L.; Blackburn, C.; Perron, J.; Sarkar, D.K. Silicone Based Superhydrophobic Coating Efficient to Reduce Ice Adhesion and Accumulation on Aluminum under Offshore Arctic Conditions. *Ocean Eng.* **2017**, *144*, 135–141. [[CrossRef](#)]
- Fakorede, O.; Feger, Z.; Ibrahim, H.; Ilinca, A.; Perron, J.; Masson, C. Ice Protection Systems for Wind Turbines in Cold Climate: Characteristics, Comparisons and Analysis. *Renew. Sustain. Energy Rev.* **2016**, *65*, 662–675. [[CrossRef](#)]
- Parent, O.; Ilinca, A. Anti-Icing and de-Icing Techniques for Wind Turbines: Critical Review. *Cold Reg. Sci. Technol.* **2011**, *65*, 88–96. [[CrossRef](#)]

12. Madi, E.; Pope, K.; Huang, W.; Iqbal, T. A Review of Integrating Ice Detection and Mitigation for Wind Turbine Blades. *Renew. Sustain. Energy Rev.* **2019**, *103*, 269–281. [[CrossRef](#)]
13. Boopathi, K.; Mishnaevsky, L., Jr.; Sumantraa, B.; Premkumar, S.A.; Thamodharan, K.; Balaraman, K. Failure Mechanisms of Wind Turbine Blades in India: Climatic, Regional, and Seasonal Variability. *Wind Energy* **2022**, *25*, 968–979. [[CrossRef](#)]
14. Xu, B.; Lu, F.; Song, G. Experimental Study on Anti-Icing and Deicing for Model Wind Turbine Blades with Continuous Carbon Fiber Sheets. *J. Cold Reg. Eng.* **2018**, *32*, 04017024. [[CrossRef](#)]
15. Georgakilas, V.; Perman, J.A.; Tucek, J.; Zboril, R. Broad Family of Carbon Nanoallotropes: Classification, Chemistry, and Applications of Fullerenes, Carbon Dots, Nanotubes, Graphene, Nanodiamonds, and Combined Superstructures. *Chem. Rev.* **2015**, *115*, 4744–4822. [[CrossRef](#)]
16. Stankevich, S.; Bulderberga, O.; Tarasovs, S.; Zeleniakiene, D.; Omastova, M.; Aniskevich, A. Electrical Conductivity of Glass Fiber-Reinforced Plastic with Nanomodified Matrix for Damage Diagnostic. *Materials* **2021**, *14*, 4485. [[CrossRef](#)]
17. Shimpi, P.; Aniskevich, A.; Zeleniakiene, D. Improved Method of Manufacturing Carbon Nanotube Infused Multifunctional 3D Woven Composites. *J. Compos. Mater.* **2022**, *56*, 479–489. [[CrossRef](#)]
18. Lee, T.; Min, S.H.; Gu, M.; Jung, Y.K.; Lee, W.; Lee, J.U.; Seong, D.G.; Kim, B. Layer-by-Layer Assembly for Graphene-Based Multilayer Nanocomposites: Synthesis and Applications. *Chem. Mater.* **2015**, *27*, 3785–3796. [[CrossRef](#)]
19. Shin, H.-J.; Jeon, S.S.; Im, S.S. CNT/PEDOT Core/Shell Nanostructures as a Counter Electrode for Dye-Sensitized Solar Cells. *Synth. Met.* **2011**, *161*, 1284–1288. [[CrossRef](#)]
20. Redondo, O.; Prolongo, S.G.; Campo, M.; Sbarufatti, C.; Giglio, M. Anti-Icing and de-Icing Coatings Based Joule's Heating of Graphene Nanoplatelets. *Compos. Sci. Technol.* **2018**, *164*, 65–73. [[CrossRef](#)]
21. Karim, N.; Zhang, M.; Afroz, S.; Koncherry, V.; Potluri, P.; Novoselov, K.S. Graphene-Based Surface Heater for de-Icing Applications. *RSC Adv.* **2018**, *8*, 16815–16823. [[CrossRef](#)] [[PubMed](#)]
22. Raji, A.-R.O.; Varadhachary, T.; Nan, K.; Wang, T.; Lin, J.; Ji, Y.; Genorio, B.; Zhu, Y.; Kittrell, C.; Tour, J.M. Composites of Graphene Nanoribbon Stacks and Epoxy for Joule Heating and Deicing of Surfaces. *ACS Appl. Mater. Interfaces* **2016**, *8*, 3551–3556. [[CrossRef](#)] [[PubMed](#)]
23. Yao, X.; Hawkins, S.C.; Falzon, B.G. An Advanced Anti-Icing/de-Icing System Utilizing Highly Aligned Carbon Nanotube Webs. *Carbon N. Y.* **2018**, *136*, 130–138. [[CrossRef](#)]
24. Venkateshalu, S.; Grace, A.N. MXenes—A New Class of 2D Layered Materials: Synthesis, Properties, Applications as Supercapacitor Electrode and Beyond. *Appl. Mater. Today* **2020**, *18*, 100509. [[CrossRef](#)]
25. Zeleniakiene, D.; Monastyreckis, G.; Aniskevich, A.; Griskevicius, P. Deformation and Failure of MXene Nanosheets. *Materials* **2020**, *13*, 1253. [[CrossRef](#)]
26. Zhang, J.; Kong, N.; Uzun, S.; Levitt, A.; Seyedin, S.; Lynch, P.A.; Qin, S.; Han, M.; Yang, W.; Liu, J.; et al. Scalable Manufacturing of Free-Standing Strong Ti₃C₂T_x MXene Films with Outstanding Conductivity. *Adv. Mater.* **2020**, *32*, 2001093. [[CrossRef](#)]
27. Alhabeb, M.; Maleski, K.; Anasori, B.; Lelyukh, P.; Clark, L.; Sin, S.; Gogotsi, Y. Guidelines for Synthesis and Processing of Two-Dimensional Titanium Carbide (Ti₃C₂T_x MXene). *Chem. Mater.* **2017**, *29*, 7633–7644. [[CrossRef](#)]
28. Kilikevicius, S.; Kvietkaite, S.; Mishnaevsky, L., Jr.; Omastová, M.; Aniskevich, A.; Zeleniakiene, D. Novel Hybrid Polymer Composites with Graphene and MXene Nano-Reinforcements: Computational Analysis. *Polymers* **2021**, *13*, 1013. [[CrossRef](#)]
29. Zukiene, K.; Monastyreckis, G.; Kilikevicius, S.; Procházka, M.; Micusik, M.; Omastová, M.; Aniskevich, A.; Zeleniakiene, D. Wettability of MXene and Its Interfacial Adhesion with Epoxy Resin. *Mater. Chem. Phys.* **2021**, *257*, 123820. [[CrossRef](#)]
30. Shimpi, P.; Omastova, M.; Aniskevich, A.; Zeleniakiene, D. In Situ Deformation Monitoring of 3D Woven Composite T-Profile Using MXene Nanoparticles. *Materials* **2022**, *15*, 2730. [[CrossRef](#)]
31. Yang, W.; Liu, J.-J.; Wang, L.-L.; Wang, W.; Yuen, A.C.Y.; Yuen, Y.; Peng, S.; Yu, B.; Lu, H.-D.; Yeoh, G.H.; et al. Multifunctional MXene/Natural Rubber Composite Films with Exceptional Flexibility and Durability. *Compos. Part B* **2020**, *188*, 107875. [[CrossRef](#)]
32. Zhao, M.-Q.; Trainor, N.; Ren, C.E.; Torelli, M.; Anasori, B.; Gogotsi, Y. Scalable Manufacturing of Large and Flexible Sheets of MXene/Graphene Heterostructures. *Adv. Mater. Technol.* **2019**, *4*, 1800639. [[CrossRef](#)]
33. Jia, X.; Shen, B.; Zhang, L.; Zheng, W. Waterproof MXene-Decorated Wood-Pulp Fabrics for High-Efficiency Electromagnetic Interference Shielding and Joule Heating. *Compos. Part B* **2020**, *198*, 108250. [[CrossRef](#)]
34. Li, L.; Cao, Y.; Liu, X.; Wang, J.; Yang, Y.; Wang, W. Multifunctional MXene-Based Fireproof Electromagnetic Shielding Films with Exceptional Anisotropic Heat Dissipation Capability and Joule Heating Performance. *ACS Appl. Mater. Interfaces* **2022**, *12*, 27350–27360. [[CrossRef](#)] [[PubMed](#)]
35. Knotek, P.; Tichý, L. Atomic Force Microscopy and Atomic Force Acoustic Microscopy Characterization of Photo-Induced Changes in Some Ge-As-S Amorphous Films. *Thin Solid Film.* **2009**, *517*, 1831–1834. [[CrossRef](#)]
36. Borysiuk, V.N.; Mochalin, V.N.; Gogotsi, Y. Bending Rigidity of Two-Dimensional Titanium Carbide (MXene) Nanoribbons: A Molecular Dynamics Study. *Comput. Mater. Sci.* **2018**, *143*, 418–424. [[CrossRef](#)]
37. Lipatov, A.; Lu, H.; Alhabeb, M.; Anasori, B.; Gruverman, A.; Gogotsi, Y.; Sinitskii, A. Elastic Properties of 2D Ti₃C₂T_x MXene Monolayers and Bilayers. *Sci. Adv.* **2018**, *4*, 1–7. [[CrossRef](#)]
38. Hassan, G.; Bae, J.; Hassan, A.; Ali, S.; Hyun, C.; Choi, Y. Ink-Jet Printed Stretchable Strain Sensor Based on Graphene/ZnO Composite on Micro-Random Ridged PDMS Substrate. *Compos. Part A* **2018**, *107*, 519–528. [[CrossRef](#)]
39. Monastyreckis, G.; Stepura, A.; Soyka, Y.; Maltanova, H.; Poznyak, S.K.; Omastová, M.; Aniskevich, A.; Zeleniakiene, D. Strain Sensing Coatings for Large Composite Structures Based on 2D MXene Nanoparticles. *Sensors* **2021**, *21*, 2378. [[CrossRef](#)]

CURRICULUM VITAE

Gediminas Monastyreckis

gediminas.monastyreckis@ktu.lt

Education:

- 2011–2016 Bachelor of Science in transport engineering, Kaunas University of Technology, study programme "Aviation Engineering".
- 2016–2018 Master of Science in transport engineering, Kaunas University of Technology, study programme "Aeronautical Engineering".
- 2018–2022 PhD studies in mechanical engineering, Kaunas University of Technology, topic: "Development of novel multifunctional polymer nanocomposites with outstanding mechanical and electrical properties".

Work experience:

- 2014–2015 Aviation mechanic UAB FL-Technics.
- 2015–2016 Helicopter mechanic UAB Helisota.
- 2021–present Assistant lecturer at Kaunas University of Technology.

ARTICLES IN PEER-REVIEWED SCIENTIFIC PUBLICATIONS

In journals indexed in the *Web of Science* with Impact Factor (JCR SCIE), when IF/AIF > 0.25

Foreign publishers

1. [S1; CH; OA] Monastyreckis, Gediminas; Tortosa Siles, Juan; Knotek, Petr; Omastova, Maria; Aniskevich, Andrey; Zeleniakiene, Daiva. Scalable MXene and PEDOT-CNT nanocoatings for fibre-reinforced composite De-Icing // Materials. Basel : MDPI. ISSN 1996-1944. 2022, vol. 15, iss. 10, art. no. 3535, p. 1-12. DOI: 10.3390/ma15103535. [Science Citation Index Expanded (Web of Science); Scopus; MEDLINE] [IF: 3,748; Q2 (2021, InCites JCR SCIE)] [Field: T 009] [Input: 0,170]
2. [S1; CH; OA] Monastyreckis, Gediminas; Stepura, Anastasiia; Soyka, Yaryna; Malanava, Hanna; Poznyak, Sergey K.; Omastová, Mária; Aniskevich, Andrey; Zeleniakiene, Daiva. Strain sensing coatings for large composite structures based on 2D MXene nanoparticles // Sensors. Basel : MDPI. ISSN 1424-8220. 2021, vol. 21, iss. 7, art. no. 2378, p. 1-14. DOI: 10.3390/s21072378. [Science Citation Index Expanded (Web of Science); Scopus; MEDLINE] [IF: 3,847; Q2 (2021, InCites JCR SCIE)] [Field: T 009] [Input: 0,125]
3. [S1; NL] Zukiene, K.; Monastyreckis, G.; Kilikevicius, S.; Procházka, M.; Micusik, M.; Omastová, M.; Aniskevich, A.; Zeleniakiene, D. Wettability of MXene and its interfacial adhesion with epoxy resin // Materials chemistry and physics. Amsterdam : Elsevier. ISSN 0254-0584. eISSN 1879-3312. 2021, vol. 257, art. no. 123820, p. 1-7. DOI: 10.1016/j.matchemphys.2020.123820.

- [Science Citation Index Expanded (Web of Science); Scopus] [IF: 4,778; Q2 (2021, InCites JCR SCIE)] [Field: T 009] [Input: 0,125]
4. [S1; CH; OA] Zeleniakiene, Daiva; Monastyreckis, Gediminas; Aniskevich, Andrey; Griskevicius, Paulius. Deformation and failure of MXene nanosheets // *Materials*. Basel : MDPI. ISSN 1996-1944. 2020, vol. 13, iss. 5, art. no. 1253, p. 1-10. DOI: 10.3390/ma13051253. [Science Citation Index Expanded (Web of Science); Scopus; MEDLINE] [IF: 3,623; Q2 (2020, InCites JCR SCIE)] [Field: T 009] [Input: 0,250]
 5. [S1; GB] Monastyreckis, G.; Mishnaevsky, L.; Hatter, C.B.; Aniskevich, A.; Gogotsi, Y.; Zeleniakiene, D. Micromechanical modeling of MXene-polymer composites // *Carbon*. Oxford : Elsevier. ISSN 0008-6223. eISSN 1873-3891. 2020, vol. 162, p. 402-409. DOI: 10.1016/j.carbon.2020.02.070. [Science Citation Index Expanded (Web of Science); Scopus] [IF: 9,594; Q1 (2020, InCites JCR SCIE)] [Field: T 009] [Input: 0,170]

In other peer-reviewed scientific publications

Foreign publishers

1. [P1d; CH; OA] Monastyreckis, Gediminas; Aniskevich, Andrey; Zeleniakiene, Daiva. Damage sensing based on electrically conductive nanoparticles in sandwich-structured composites // *Composites meet sustainability: proceedings of the 20th European conference on composite materials, ECCM20, 26–30 June 2022, Lausanne, Switzerland* / edited by: A.P. Vassilopoulos, V. Michaud. Lausanne : Ecole Polytechnique Fédérale de Lausanne, 2022. eISBN 9782970161400. p. 934-939. [Field: T 009] [Input: 0,334]
2. [P1d; CH; OA] Zeleniakiene, Daiva; Monastyreckis, Gediminas; Omastova, Maria; Aniskevich, Andrey. MXene nanoparticles to impart multifunctional properties to fibre reinforced plastic composites // *Composites meet sustainability: proceedings of the 20th European conference on composite materials, ECCM20, 26-30 June 2022, Lausanne, Switzerland* / edited by: A.P. Vassilopoulos, V. Michaud. Lausanne : Ecole Polytechnique Fédérale de Lausanne, 2022. eISBN 9782970161400. p. 1496-1500. [Field: T 009] [Input: 0,250]

Lithuanian publishers

[P1d; LT] Trifeldaitė, Gerda; Žukienė, Kristina; Monastyreckis, Gediminas; Zeleniakiene, Daiva. Wettability and surface tension of MXene films // *International young researchers conference "Industrial engineering 2020" notification material = Tarptautinės jaunujų tyrėjų konferencijos „Pramonės inžinerija 2020“ pranešimų medžiaga*. Kaunas : Technologija. ISSN 2538-6727. 2020, p. 239-245. DOI: 10.5755/e01.2538-6727.2020. [Field: T 008] [Input: 0,250]

PRESENTATION OF RESEARCH RESULTS AT CONFERENCES

Other conference presentation abstracts and non-peer reviewed conference papers

1. [T3; LT] Jovarauskaitė, Gabrielė; Monastyreckis, Gediminas; Zeleniakienė, Daiva (temos vadovas). Self-sensing sandwich-structured composites // Technorama 2022: Code: innovation: catalogue. Kaunas : KTU. 2022, p. 51-52. [Field: T 009]
2. [P1d; CH; OA] Monastyreckis, Gediminas; Aniskevich, Andrey; Zeleniakiene, Daiva. Damage sensing based on electrically conductive nanoparticles in sandwich-structured composites // Composites meet sustainability: proceedings of the 20th European conference on composite materials, ECCM20, 26-30 June 2022, Lausanne, Switzerland / edited by: A.P. Vassilopoulos, V. Michaud. Lausanne : Ecole Polytechnique Fédérale de Lausanne, 2022. eISBN 9782970161400. p. 934-939. [Field: T 009] [Input: 0,334]
3. [T3; IT] Monastyreckis, G.; Zeleniakiene, D. MXene coated multifunctional composites for aerospace application // 10th international conference "Times of polymers (TOP) and composites", September 5-9, 2021, Ischia, Italy: book of abstracts. [S.l.] : [s.n.]. 2021, p. 38. [Field: T 009]
4. [T2; LT] Monastyreckis, Gediminas; Zeleniakienė, Daiva. Novel multifunctional polymer nanocomposites with outstanding mechanical and electrical properties // Industrial engineering 2021: international young researchers conference notification material, May 13, 2021, Kaunas, Lithuania / Antanas Čiuplys (ats. redaktorius). Kaunas : Kaunas university of technology. ISSN 2538-6727. 2021, p. 11. [Field: T 009]
5. [T3; LT] Monastyreckis, Gediminas; Shimpi, Prasad P.; Subadra, Sharath P.; Špakauskas, Kęstutis; Atmakuri, Ayyappa; Vaitkūnas, Tomas; Zeleniakienė, Daiva; Griškevičius, Paulius; Palevičius, Arvydas; Janušas, Giedrius. Composite materials: from nature to cosmos // Technorama 2021: from vision to innovation. Kaunas : KTU. 2021, p. 112-113. [Field: T 009]
6. [T3; LV; OA] Monastyreckis, G.; Zeleniakiene, D. Multifunctional polymer composites coated with MXenes // Durability of advanced polymer composites: 79th conference of the University of Latvia, online, February 16, 2021: book of abstracts. [Riga] : [University of Latvia]. 2021, p. 11. [Field: T 009]
7. [T3; LT] Trifeldaitė, Gerda; Monastyreckis, Gediminas; Žukienė, Kristina; Zeleniakienė, Daiva. Multifunctional MXene-polymer composites and coatings // Technorama 2020: from vision to innovation. Kaunas : KTU. 2020, p. 107-108. [Field: T 008]
8. [T3; AU] Monastyreckis, G.; Mishnaevsky Jr., L.; Aniskevich, A.; Zeleniakiene, D. Modelling of mechanical behaviour of MXene/polymer nanocomposites // 22nd international conference on composite materials (ICCM-22), Melbourne, Australia, 11–16 August 2019. [S.l.] : [s.n.]. 2019, p. 1. [Field: T 009]

ACKNOWLEDGMENTS

The dissertation was prepared on the topics of the following projects and was carried out in cooperation with their consortia:

H2020-MSCA-RISE-2017 Project No. 777810 “Multifunctional polymer composites doped with novel 2D nanoparticles for advanced applications,” Nano2Day. This project has received funding from the European Union's Horizon 2020 research and innovation program under the Marie Skłodowska-Curie grant agreement No. 777810.

M-ERA.NET project No. project5015 “Advanced Polymer Composites Filled with Novel 2D Nanoparticles,” NANO2COM. This work was developed under the M-era.Net research project titled NANO2COM–Advanced Polymer Composites Filled with Novel 2D Nanoparticles. The research was funded by grants No. S-M-ERA.NET-18-1 from the Research Council of Lithuania, No. 1.1.1.5/ERANET/18/02 from Latvian State Education Development Agency and No. M-ERANET-18-414-Nano2Com from the Slovak Academy of Sciences.

The authors would like to acknowledge SYNPO A.S. (the Czech Republic) for supplying the PEDOT-CNT paste.

The author wants to thank Dr.-Ing. habil. Leon Mishnaevsky Jr. for his valuable ideas through the work of modelling, Prof. Dr. DSc. Yury Gogotsy for mentoring and support, Prof. Dr. Paulius Griškevičius and Assoc. Prof. Dr. Vitalis Leišis for advices, consultations and technical support, Dr. Michal Procházka and Dr. Vladimir Spacek for consultations and technical support, Dr. Alena Opalkova Siskova and Dr. Simona Tučkutė for contributing to the SEM studies.

UDK 678.01+620.1](043.3)

SL 344. 2023-05-17, 13,5 leidyb. apsk. I. Tiražas 14 egz. Užsakymas 84.
Išleido Kauno technologijos universitetas, K. Donelaičio g. 73, 44249 Kaunas
Spausdino leidyklos „Technologija“ spaustuvė, Studentų g. 54, 51424 Kaunas

